Control of Microstructure in Laser Additive Manufacturing

by

Mohammad Hossein Farshidianfar

A thesis
presented to the University of Waterloo
in fulfillment of the
thesis requirement for the degree of

Master of Applied Science
in
Mechanical Engineering

Waterloo, Ontario, Canada, 2014

AUTHOR'S DECLARATION

I hereby declare that I am the sole author of this thesis. This is a true copy of the thesis, including any required final revisions, as accepted by my examiners.

I understand that my thesis may be made electronically available to the public.

Mohammad H. Farshidianfar

Abstract

Since its arrival in the late 1980's, Laser Additive Manufacturing (LAM) has come a long way to establish itself as one of the most advanced versatile manufacturing technologies in the 21st century. LAM implies a novel layer by layer solidification of powder injected materials for the formation of arbitrary configurations. Production of complex shaped functional metallic components, including metals, alloys and metal matrix composites (MMCs), with desired mechanical and metallurgical properties is currently the main focus in the LAM industry. A potential problem in applying the LAM technique however, is the possibility of an inconsistent microstructure throughout a complex component.

The emphasis of this thesis is to develop an automated closed-loop system in order to control deposition microstructure of the LAM process in real time. An infrared imaging system is developed to monitor thermal properties of the process as feedback signals. Cooling rate and melt pool temperatures are recorded in real time to provide adequate information of the thermal process. The aim is to provide a consistent microstructure by controlling thermal characteristics involved in the LAM.

An experimental analysis is developed to identify cooling rate and melt pool temperature effects on the final microstructure using two combined parameters: the effective energy density and the effective powder deposition density. The analysis provides critical insight of how the microstructure is specifically dependent on the cooling rate and its variations. Further study is conducted to evaluate cooling rate effects on the microstructure properties such as the morphology, grain size and phase transformations. Positive correlation is observed between microstructure evolutions and the cooling rate. On the other hand, cooling rate variations are also studied with respect to the traveling speed, in order to identify a suitable controlling action for the controller.

Using the identified correlations between the cooling rate, travelling speed and the clad microstructure, a novel feedback PID controller is established to control the cooling rate. The controller is designed to operate the cooling rate around a desired point by tuning the travelling speed. The performance of the controller is examined on several single-line and multi-line closed-loop claddings in order to achieve desired microstructures with specific properties. Results show that the closed-loop controller is capable of generating a consistent controlled microstructure during the LAM process in real time.

Acknowledgements

This thesis owes its existence to the help, support and inspiration of many people. Firstly, I would like to express my sincere appreciation and gratitude to Professor Amir Khajepour and Adrian Gerlich for their overwhelming support over the past 2 years. They have been an immense source of knowledge, enthusiasm, encouragement and friendship. I offer my regards and blessings to all who have supported me in any respect during the completion of this research.

Last but not least, my deepest gratitude and love for my parents Anooshiravan and Maryam, whose dedication and the many years of support during my studies have provided the foundation for this work.

Dedication

I would like to dedicate this thesis to my parents Anooshiravan and Maryam, who have taught me how to live.

Table of Contents

List of Figures

List of Tables

Chapter 1
Introduction

Laser Additive Manufacturing (LAM) implies layer by layer shaping of materials (usually in the form of powder) to arbitrary configurations and geometries, using a comprehensive integration of materials science, mechanical and control engineering, and laser technology. The LAM technology, which uses computer controlled high power lasers as the energy source, is regarded as an important revolution in the manufacturing industry. The technology is currently being used in manufacturing and repair, cladding, design of novel alloys or functionally graded materials (FGM), and metallic rapid prototyping.

LAM offers several advantages in terms of process optimization and quality of the final product over traditional deposition techniques such as arc welding and plasma spraying. LAM provides minimal dilution and distortion, smaller heat affected zone, and better surface quality or geometry control. On the other hand, the strengths of laser additive manufactured parts lie in those areas where conventional manufactured parts reach their limitations. The technology brings in a new approach towards design and manufacturing by enabling a design-driven manufacturing process where design is no longer limited by production methods. Furthermore, highly complex structures and materials which can still be extremely light and stable are achievable by the process. Due to the high cooling rates, fine-grained microstructures are produced during solidification in the LAM process.

Although, LAM is capable of processing a broad range of metals, alloys, ceramics and MMCs, the mechanical properties (geometry, strength, hardness, residual stress) and microstructural characteristics (morphology, grain size, phase precipitation, etc.) of the depositions are difficult to be tailored to a specific application. Process disturbances may even cause variations in the clad properties between reproduced processing cycles performed using the same operating conditions. This poor reproducibility arises from the high sensitivity of LAM to small changes in the operating parameters and process disturbances. The process involves complex non-equilibrium physical and chemical metallurgical process, which exhibits multiple modes of heat and mass transfer such as Marangoni flow, buoyancy, convection, and in some instances, chemical reactions. The majority of the current literature has focused on understanding of the relationships between a material's final microstructural and physical characteristics and conditions of solidification. Reports reveal that the complex metallurgical phenomena during LAM processing are strongly material and process dependent and governed by

process parameters (e.g. laser power, laser type, traveling speed, spot size, scan line spacing and powder characteristics).

The next big step for the LAM technology is to produce complex shaped functional metallic components, including metals, alloys and metal matrix composites (MMCs) that have to meet specific mechanical and metallurgical demands from the aerospace, automotive, rapid tooling, and biomedical industrial sectors. Finding an optimal set of experimental parameters and using them in an open-loop laser cladding process may not result in a good quality clad due to random or periodic disturbances in the system. Therefore, development of an intelligent closed-loop control system is essential for overcoming the aspects of disturbances in the process.

While, previous researchers have been successful in developing closed-loop control process for geometrical properties (e.g. clad height and width) of the LAM process, there have been no successful attempts in closed-loop control of microstructural aspects of LAM products. Microstructure analysis is by far the broadest area of research in the LAM industry; however, the majority of studies report microstructural evolutions off-line and for a specific material. For sensitive processes like LAM, which are continuously disturbed by process and environmental variables, each specific material operated at a specific configuration requires a separate set of off-line analysis. What is more, offline analysis of microstructural evolutions do not guaranty consistent desired properties, due to the presence of real time process disturbances. Therefore, an intelligent closed-loop control system, which can monitor and track desired microstructural properties of the LAM process in real time is of great importance.

In this thesis, preliminary steps are taken towards understanding the microstructural evolutions in real time in order to develop an intelligent expert system for a fully automated and adaptive laser fabrication process.

1.1 Fundamentals of LAM

The first step in developing an intelligent closed-loop LAM process is to gain insight into the process and its features. In this process, a stream of metallic powder is fed on to a substrate, a high power laser beam melts the injected powder particles and parts of the substrate. As the laser heats up the substrate, the molten metal is attached to the moving substrate to produce a deposited layer as shown in Figure 1-1. By producing clads besides and on top of each other, a functional component is made in a layer-by-layer fashion.

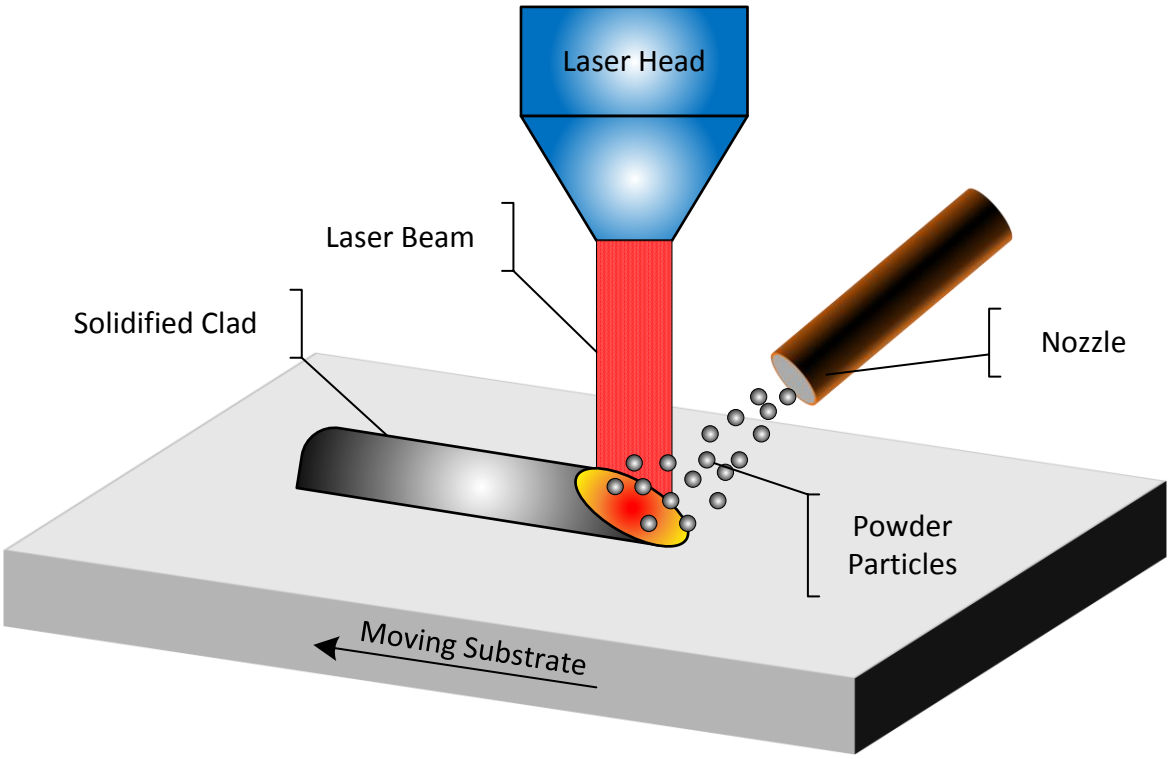

Figure 1-1 Schematic view of the Laser Additive Manufacturing (LAM) process.

LAM has specific features, which makes it unique compared to other deposition methods [1], [2]:

1. Reduced dilution, which is the mixing percentage of the substrate to the clad region (compared to laser alloying)
2. High heating/cooling rates ($10^3 - 10^8\ Ks^{-1}$) at the solid/liquid interface in a small sized molten pool ($1\ mm$), which results in refined grain microstructure
3. Improved wear resistance and hardness
4. Reduced thermal distortion
5. Reduced porosity, particularly in LAM by powder injection, which results in production of near full density components made from metals, alloys and blended/composite powders
6. Improved process control
7. Reduced post-cladding machining time and cost

As illustrated in Figure 1-1, the LAM process is a conjunction of the main four engineering fields: (1) laser technology, (2) computer-aided design (CAD) and manufacturing (CAM), (3) robotics, sensors and control, and (4) powder metallurgy. These areas have made LAM one of the most broadest fields in the industry.

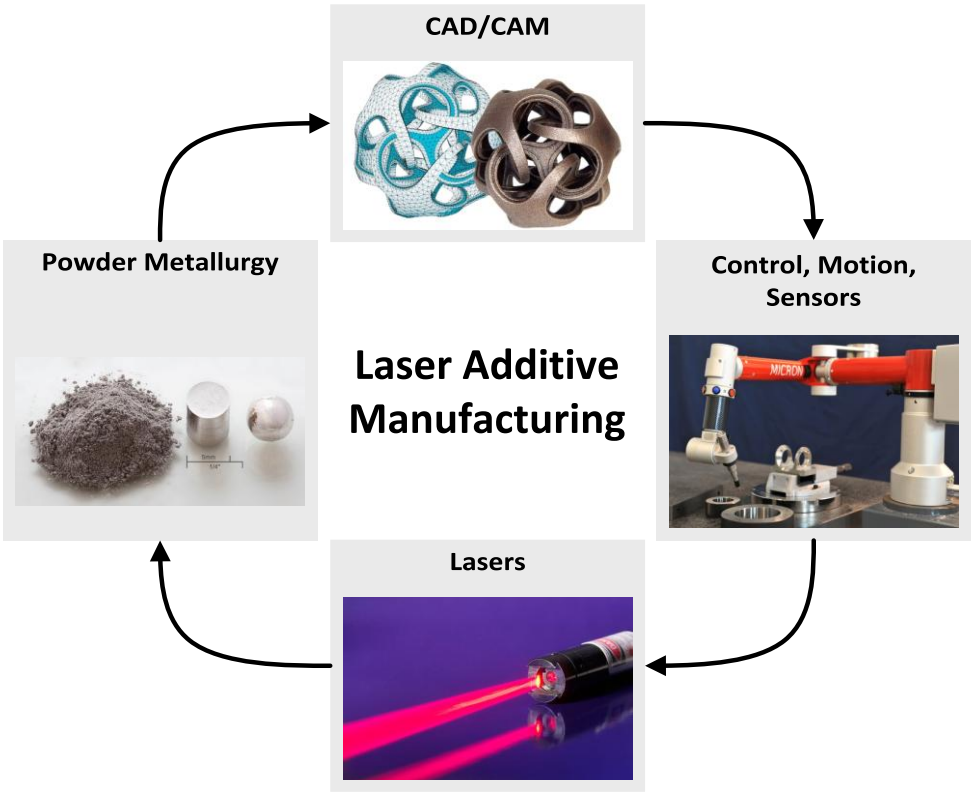

Figure 1-2 Different fields involved in LAM [3]–[6]**.**

Various configurations have been arranged for LAM based on these features:

- **Lasers:** Initially, CO_2 lasers were used in LAM as they were the first laser sources available with high power outputs (a minimum power of $500\ W$). Over the past 2 decades new laser sources such as Nd:YAG, diode, disk, and more recently fiber lasers have been developed, which can produce high power outputs with greater efficiency and shorter wavelengths. Pulsed and continuous wave lasers are both applicable in LAM, although, selecting the proper type of laser highly depends upon the type of the application.

- **Material Feeder:** LAM requires additive materials. These materials are either preplaced on the substrate before laser processing (e.g., galvanizing, thermal spraying) or fed into the interaction zone in form of powder or wire. Direct feeding techniques such as powder feeding are well established these days, since preplacing limits thickness and materials and requires an additional process which increases the costs. Nozzles in LAM with powder feeding are either lateral or coaxial.

- **Motion:** The substrate and the laser head have to move relative to each other in order to produce a deposition layer. Various configurations have been developed for generation of this relative motion. In some configurations the laser head is stationary and the substrate moves by a multi-axis CNC machine. In others, the substrate is stationary and the laser head and powder feeder system move by a robotic arm with several degrees of freedom. There are cases in which both the laser head and the substrate move.

1.2 Closed-loop Control of LAM

The second step towards developing a real time closed-loop LAM system is design and implementation of a closed-loop controller considering all system constraints. Implementation of a closed-loop controller requires a set of feedback signals, control actions, and a robust control algorithm.

Since the aim of the present thesis is to control the clad microstructure in real time, feedback signals have to provide information regarding the temperature and solidification process. Microstructural features in LAM are related to thermal gradients, cooling rates and melt pool temperature. A thermal vision feedback system has to be developed to record and process the thermal cycles in real time. There are several devices available to capture the thermal history, including thermocouples, pyrometers and infrared cameras. Each of these instruments is suitable for a specific application. The selection of an appropriate device for capturing the current feedback signal is of crucial importance.

There are many parameters involved in LAM, which make LAM a complex process. These parameters result in several physical phenomena, which govern the process. The output of LAM is composed of many factors such as microstructure, hardness, clad geometry including clad height, width, angle of wetting, and cross sectional profile, cracks, pores, residual stresses and dilution [1]. It is essential to know how these input parameters affect the output parameters. Figure 1-3 summarizes the inputs, outputs and process parameters that are present in the LAM process.

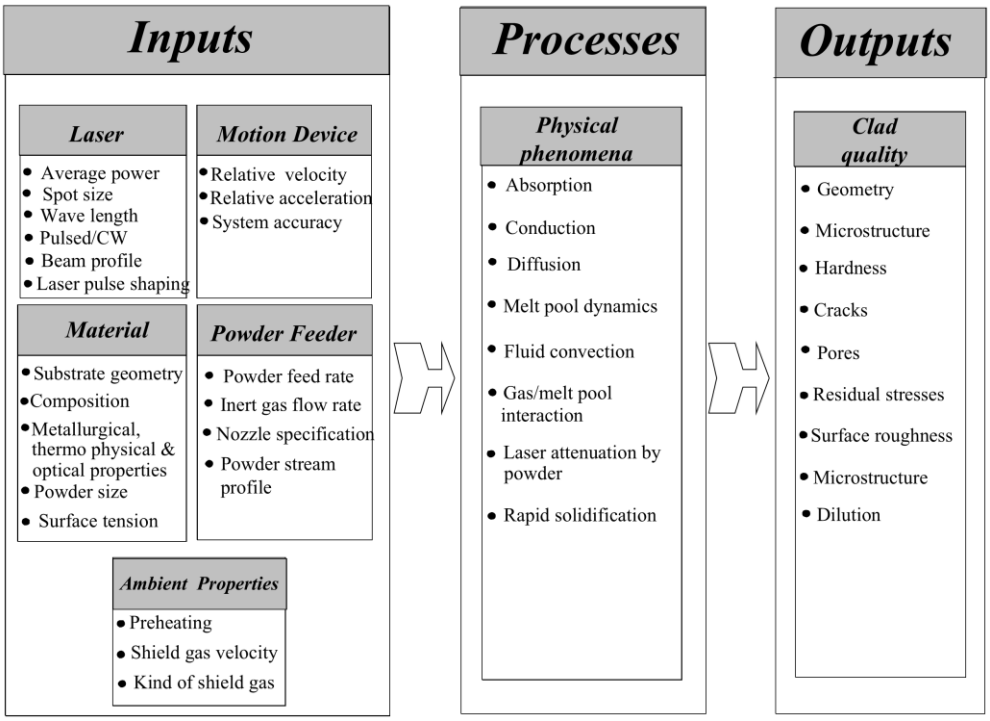

Figure 1-3 Inputs, outputs and process parameters of LAM by powder injection [1].

Therefore, identifying the proper input parameter for obtaining desired outputs is very challenging. Every closed-loop process requires a series of changing inputs so called control actions to reach the desired output parameters. Designating the suitable controlling actions is one the most challenging and significant steps in implementing a closed-loop controller. After assigning the proper feedback and control action signals, an appropriate controlling scheme is required. There are several controlling algorithms available in theory, which have to implemented and evaluated for specific LAM applications.

1.3 Statement of Objective and Scope

The main objective of the thesis is:

To establish the feasibility of real-time microstructure control for the LAM process by gaining insight into microstructural evolution during laser deposition by means of in-situ real time monitoring of the thermal process.

In order to reach the aforementioned goal it is required to have a good understanding of the LAM thermal process and how it affects the microstructural aspects of the system. An infrared-based thermographic system will be developed to monitor thermal characteristics such as the cooling rate and melt pool temperature in real time. Experimental analysis will be held to correlate thermal variations with microstructural evolutions. The system identification process is limited to general experimental investigations on a stainless steel powder. Finally, to implement a real time microstructure control scheme for the LAM process, a PID controller is designed to control the cooling rate in real time to develop consistent desired microstructures.

1.4 Thesis Overview

The thesis is divided into six chapters. Chapter 2 provides a review of the literature related to this research topic to identify the contribution of this work. The background of microstructure analysis, phase diagrams and thermal control are also discussed. Experimental setup and data acquisition system is discussed in Chapter 3. The experimental results of microstructure analysis and closed-loop control are discussed in Chapter 4 and Chapter 5, respectively. The final section, Chapter 6, presents conclusions and future perspectives of the research.

Chapter 2
Literature Review and Background

In this chapter, the existing literature and background on laser additive manufacturing technology is reviewed. It continues with description on the thermal characteristics of the process and their effects on microstructural evolutions. The employment of various thermal sensors for process monitoring is studied. Finally, phase diagrams and solidification processing applicable to laser additive manufacturing are discussed and reviewed in detail.

2.1 Laser Additive Manufacturing

Laser Additive Manufacturing (LAM) is a collection of laser technology, computer-aided design and manufacturing (CAD/CAM), actuators, sensors and control, and powder metallurgy that creates parts in a layer-wise fashion. The technology owes its existence to the discovery of lasers in 1960 [7]. The term "laser" is an abbreviation for "Light Amplification by Stimulated Emission of Radiation". The ability to emit light coherently, allows a laser to produce high power beams, which can be focused on a fine spot. This characteristic of lasers, enables applications like laser welding, laser cutting and LAM.

LAM was first introduced in 1971 by Ciraud [8], which proposed a powder process that has the features of modern powder-based direct deposition additive manufacturing techniques. However, the material used in Ciraud's experiments were partially melted and most were non-metallic particles. One of the first approaches towards laser additive manufacturing of metallic components was conducted in 1982 by Brown, Breinan and Kear [9] at United Technologies Corporation. They proposed a method for the production of bulk rapidly solidified metallic articles of near-net shape, by depositing multiple thin layers of feedstock using an energy beam to fuse each layer onto a substrate. The feedstock was in the form of metal powder or wire. Apart from rapid prototyping applications of LAM, other applications such as laser surface treatment and laser cladding received great attention from researchers. Gnanamuthu [10] and Seaman [11] introduced application of lasers in surface treatment in the mid 70's. Later in the 80's, Steen [12] used this method to develop a laser cladding process, which falls under the LAM techniques.

Since the first applications of LAM were introduced for metallic parts, there have been great improvements and modifications in the process. Many research groups around the globe have

conducted research on the topic. The following are some of the most important LAM processes developed by different research groups:

- "Automated Laser Fabrication" at University of Waterloo [1]
- "Laser Engineered Net Shaping" at Sandia National Laboratories [13]
- "Direct Metal Deposition" at University of Michigan at Ann Arbor [14]
- "Laser Based Manufacturing" at University of Cambridge [15]
- "Direct Laser Manufacturing" at Georgia University of Technology
- "Laser Beam-Based Additive Manufacturing Processes" at Carnegie Mellon [16]
- "Laser Direct Casting" at University of Liverpool [17]
- "Additive Manufacturing Alliance" at Fraunhofer Institute for Machine Tools and Forming Technology IWU
- "Direct Light Fabrication" at Los Almos National Laboratories [18]
- "Freeform Laser Consolidation" at National Research Center [19]
- "Laser Additive Manufacturing" at Pennsylvania State University
- "Laser Rapid Manufacturing" at Raja Ramanna Center for Advanced Technology
- "Laser Assisted Material Processing" at University of Illinois
- "Laser Direct Metal Deposition" at University of Manchester
- "Laser Cladding" at University of Purdue [20]

A wide variety of different aspects of the LAM process has been investigated by the above research groups. These aspects include: process modeling, control and automation, optimization, system identification, hardware and software integration, metallurgical and mechanical characterization of the process. These in-depth research areas have resulted in several system manufacturers and developers in the LAM industry. Some of the most important commercialized LAM systems are:

- **TruLaser Cell:** Manufactured by TRUMPF [21]
- **Electro Optical Systems GmbH (EOS)**

- **Concept Laser GmbH**: Manufactures the patented Laser CUSING® method [22]
- **Optomec:** Commercializes the Aerosol Jet technology and Laser Engineered Net Shaping process (TM) (LENS®) developed at Sandia National Labs [23]
- **DM3D (POM):** Commercialized the DMD technology [24].
- **BeAM:** Developed the CLAD® process [25].

The primary goal in all the above systems is to build metal parts with desired mechanical and metallurgical properties for functional prototypes and products. In 3D laser additive manufacturing, a large number of parameters govern the process; they are sensitive to environment variations and significantly influence each other as well. As shown in Figure 1-3, these parameters are categorized into three groups [1]: (1) input parameters (laser, motion device, material, feeder mechanism and ambient properties), (2) process parameters (phase transformation, thermodynamics and heat transfer), and (3) output parameters (mechanical and metallurgical clad properties). The input parameters define process parameters, and the final output parameters are also governed by the process parameters. Thus, there is great interaction and influence between each and every one of these parameters. A small disturbance in one of the parameters, from the environment or from the laser-material interaction itself may result in defects in the mechanical and metallurgical properties of the clad. The complexity and disturbance of the LAM process has been the main challenge for engineers over the past few decades. Therefore, understanding the dynamics, monitoring, and controlling the laser additive manufacturing process are necessary to achieve a good manufactured part in terms of metallurgical and mechanical properties.

In order to generate a good controlling technique, it is necessary to know the main output parameters of the process that define the final product. Clad geometry and microstructure are the two significant output parameters that define the mechanical and metallurgical properties of the deposition. In applications like rapid prototyping, the height, width, depth of penetration and dilution of the clad are of most importance. These dimensions are directly related to the clads' geometry. On the other hand, properties such as; bonding, hardness, wear, residual stress, crack formation and surface roughness, are the main subjects of attention in parts and repair, coating, mold making and manufacturing industries. These properties are a function of the output microstructure after the solidification process. Hence, understanding microstructural evolutions and geometrical variations inside the LAM process, and controlling them is an essential need.

2.2 Microstructural Evolution in Laser Additive Manufacturing

Deposition microstructure plays an important role in the LAM process control, due to mechanical and material property requirements in the finished parts. It is of great priority to obtain a consistent and desirable microstructure to the successful application of processes [26]. Thus, prediction and control of the major process outputs such as the cladding microstructure and geometry, are a necessity. Microstructure modeling and controlling techniques of the LAM process are categorized into three groups: (1) experimental analysis, (2) analytical analysis, and (3) numerical analysis.

The majority of the research available in literature for LAM microstructure modeling and control belong to experimental analysis. There are complex non-equilibrium physical and chemical metallurgical processes involved in LAM, which exhibit multiple modes of heat and mass transfer [27]–[30], and even chemical reactions [31], [32]. Thus, obtaining an exact analytical or numerical model for the microstructure is hard to achieve.

2.2.1 Microstructural Evolution in Stainless Steel Depositions

Microstructures of numerous metallic compositions have been studied in several LAM works. Stainless steel compositions are one of the most widely used materials in LAM. Austenitic stainless steels, such as AISI type 316, are particularly interesting for LAM because they are relatively expensive to be machined. Corrosion sensitive grain boundaries are also a result of welding different type of steels [33]. Near net shaped structures produced by LAM save a great amount of material loss, and decrease waste of expensive metals such as Ni, Cr and Mo. For engineering applications, AISI 316 steel presents outstanding inter-granular corrosion resistance, good grain corrosion resistance to most chemicals, salts and acids, while higher Mo content helps increase resistance in marine environments [34]. AISI type 316L, which is the low carbon version of AISI 316, is virtually immune to sensitization (grain boundary carbide precipitation) [35] and are especially suitable for in vivo applications [36]. Current applications of the type AISI 316 L processed by LAM are: dental caps; ultra-light structures and channels for aircraft, automotive, and medical industries; thin- walled assembly parts; and chirurgical devices.

Ultimate tensile strength, yield strength and total elongation of 316 stainless steel deposition were evaluated by Keicher [37] in Laser Engineered Net Shaping (LENS). Pinkerton et al. [38] studied the connections between input parameters and final material properties and surface finish in laser cladding of stainless steel 316L. David et al. [39] determined the effect of rapid solidification on the weld metal microstructure of austenitic stainless steels and studied its implication on the ferrite constitution

diagram. Zhang et al. [40] analyzed microstructure and properties of laser direct deposited 663 copper alloy and 316L stainless. Mazumder et al. [41] studied the microstructure and mechanical properties of H13 alloy deposited by Direct Metal Deposition (DMD). Surface finish in laser solid freeform fabrication of an AISI 303L stainless steel thin wall was verified by microstructural examination by Alimardani et al. [42]. Abd-Elghany and Bourell [43] studied the effect of layer thickness and speed on structure and selected properties of low cost feedstock 304L stainless steel fabricated by Selective Laser Melting (SLM). Delgado et al. [44] found out how scanning speed, layer thickness, and building direction, as process parameters, affect the part quality and mechanical properties of iron-based products manufactured by Direct Metal Laser Sintering (DMLS) and SLM technologies. Further work on selective laser melting of iron-based powders was conducted by Kruth et al. [45], in which they studied the effect of pulsed peak intensities on microstructures. Gu et al. [46], [47] studied direct metal laser sintering of AISI 316L powders for the preparation of porous components. The processing conditions, microstructural features, and mechanical properties of DMLS-processed porous metals were assessed and the formation mechanisms of pores were elucidated. Li et al. [48] later fabricated 316L stainless steel sample with a graded porous microstructure along the speed gradient direction. Yasa and Kruth [49] investigated the influence of laser re-melting on microstructure and density of SLM 316L stainless steel parts. There have also been investigations into producing novel stainless steel alloys in SLM by consolidating 316L and 17-4PH SS powder mixtures and evaluating their microstructure variations.

2.2.2 Microstructural Evolution in Titanium Alloy Depositions

Apart from stainless steel materials, titanium and its alloys have also been an attractive field of study in the LAM industry because of their lightweight, high strength properties and excellent behavior at high temperatures. Kobryn and Semiatin [50], investigated the relationships between LAM processing parameters and Ti–6Al–4V microstructure, obtaining processing maps for the process. Brandl [51] investigated and discussed the morphology, microstructure, chemical composition, and hardness of additive manufactured Ti-6Al-4V blocks. Emamian et al. [52]–[55] studied the effects of processing parameters and combined laser process parameters on microstructural evolutions of Fe-TiC composition. They also analyzed tribology characteristics of the Fe-TiC deposition as a function of microstructure and morphology. Klingbeil et al. [56] showed that process variables (beam power and velocity) can vary the microstructure significantly throughout the depth of the deposit, and that under high power conditions a transition from columnar to mixed columnar and equiaxed structures is

possible. The effect of free-edges on melt pool geometry and solidification microstructure has also been considered [57].

There are also several numerical modeling approaches towards laser additive manufacturing of metallic alloys to correlate microstructural evolutions with process variables. “Process mapping” is one of the most widely used terms that denotes mapping of process outcomes in terms of process variables by means of numerical results for single processes, usually in terms of non-dimensional quantities. Early work in process mapping addressed the modeling and measurement of residual stress in metal and polymer deposition SFF processes [58]–[61]. In the work on transient melt pool response, numerically determined melt pool response times are used to establish a lower bound on the response times of thermal feedback control systems for LENS [16].

The first attempt to predict and control microstructure in laser deposition processes based on thermal conditions at the onset of solidification was carried out by Bontha and Klingbeil [62] in 2003. Early studies in the literature [62]–[66] employed the Rosenthal solution [67] for a moving point heat source on an infinite substrate to identify the dimensionless process variables governing thermal conditions in laser deposition processes [62]. Bontha and Klingbeil [62] extracted cooling rates and thermal gradients at the onset of solidification numerically from the Rosenthal solution throughout the depth of the melt pool, and developed dimensionless process maps for both thin-wall and bulky deposits. They obtained solidification maps for Ti-6Al-4V, which provided insight into the effects of process variables on grain morphology. Cao [68] developed a process model of microstructure evolution by utilizing a phase-field method. Different solidification morphologies of different locations in the melt pool were also investigated. It was found that it is not the mass transfer but the heat transfer in the melt pool that dominates the solidification process [68].

2.3 Thermal Control in LAM

The mechanical properties of the deposited material are dependent on the solidification microstructure (grain size and morphology), which is controlled by the thermal conditions at the onset of solidification [50]. The grain morphology, grain size, and texture that result from solidification are controlled primarily by the thermal conditions that exist locally at the start of solidification, while the fine-scale microstructure is controlled primarily by the post-solidification cooling rate [50]. The thermal process in laser cladding is an indicator of microstructure and mechanical properties, clad quality and dilution. Thus, measuring the real time thermal conditions of the LAM process is of significant importance in

predicting and controlling the deposition microstructure. However, real time measurements of the thermal process is a great burden in LAM, due to the very fast solidification rates present in the process.

Temperature is a measure of the average kinetic energy of the particles in a sample of matter expressed in units of degrees on a standard scale. Temperature can be measured in many different ways that vary in application, equipment cost and accuracy. The most common types of sensors used for temperature measurement in LAM are categorized as:

- **Thermocouples:** Thermocouples are the most commonly used temperature sensors because of their relatively low prices yet accurate output that can operate over a wide range of temperatures. A thermocouple is created when two dissimilar metals touch and the contact point produces a small open-circuit voltage as a function of temperature. The changing temperature at the junction induces a change in electromotive force (emf) between the other ends. To obtain temperature the thermoelectric voltage is calculated and used. There are different types of thermocouples according to American National Standards Institute (ANSI) conventions. The most common types of thermocouples include B, E, K, N, R, S, and T.
- **Pyrometers (thermometers):** A pyrometer or thermometer as shown in Figure 2-1, in very simple terms, consists of an optical system and detector. The energy emitted by an object is focused onto the detector by means of an optical system, which is sensitive to radiation. The output of the detector is proportional to the amount of energy radiated by the target object and the response of the detector to the specific calibrated radiation wavelengths. The emissivity, of the object is an important variable in converting the detector output into an accurate temperature signal by using Planck's law of thermal radiation.

Figure 2-1 Pyrometer [69]**.**

Infrared pyrometers, by specifically measuring the energy being radiated from an object in the 0.7 to 20 micron wavelength range, are a subset of radiation thermometers. As opposed to thermocouples, there is no need for direct contact between the radiation thermometer and the object. Radiation thermometers are suited especially to the measurement of moving objects or any surfaces that cannot be reached or can not be touched such as the substrates in the LAM process.

The benefits of radiation thermometry also come with some major draw backs. Even the simplest thermometers are more expensive than a standard thermocouple. In addition, the user requires to know the emissivity of the object being measured, whereas, emissivity of several materials at several temperatures is unknown. On the other hand, measurement regions of pyrometers are limited to point measurements only. Thus, the user can only measure one measurement point at each sample time.

- **Infrared Cameras (IR-camera):** An IR-camera is a device that forms an image using infrared radiation as illustrated in Figure 2-2, similar to a common camera that forms an image using visible light. Instead of the $450-750\ nm$ range of the visible light camera, infrared cameras operate in wavelengths as long as $14000\ nm$ ($14\ \mu m$).

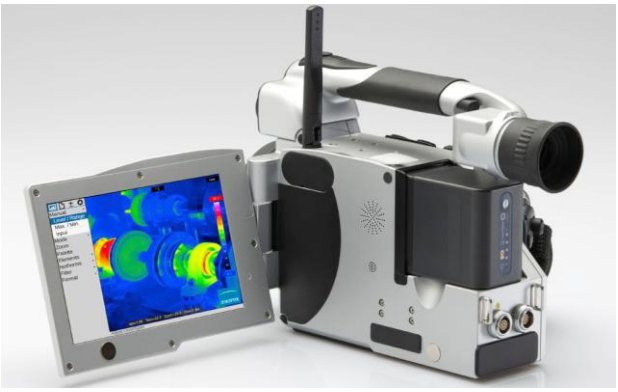

Figure 2-2 Infrared camera [70]**.**

There are two types of cooled and uncooled infrared detectors. Uncooled thermal cameras are operated by a sensor ran at ambient temperatures or controlled close to ambient temperatures. Modern uncooled detectors all use sensors that work by the change of resistance, voltage or current when heated by infrared radiation. These changes are then measured and compared to the values at the operating temperature of the sensor.

IR-cameras have all the advantages of a pyrometer including some major features, which makes them a suitable choice for industrial applications such as LAM. Unlike pyrometers, which can only take point (single pixel) measurements, IR-cameras can measure an area of interest (image pixels). This feature enables IR-cameras to provide greater information on a region of interest rather than a point of interest. With this additional advantage, the temperature history of a fixed point in space can be measured in consecutive images of an IR image, which cannot be achieved by a pyrometer. Hence, real time measurements of melt pool temperature and solidification cooling rates in LAM is easily applicable by IR-cameras, whereas, pyrometers are only able to provide information on one single point, usually the melt pool temperature. On the other hand, the problem of emissivity and cost still exist for IR-cameras as well.

The temperature of the melt pool in LAM is high enough to generate thermal infrared and visible radiation. Consequently, radiation pyrometry using the Plank's radiation law is the most convenient method for measuring the LAM thermal process [71]. According to previous studies by Li [72] and Meriaudeau [73], since most materials used in LAM have melting points greater than $800\,℃$, the wavelength region of interest for the LAM thermal process lies between 0.7 and $15\ \mu m$, the part of the electromagnetic spectrum in which most radiometric surface temperature measurements are made. The

sensor output is based on the melt pool radiation, and consequently dependent upon the melt pool temperature, shape, size, and the distance to the sensor, as well as the sensor viewing angle [74].

Thermal gradients in LAM are governed by solidification characteristics of the process. LAM is a solidification process, which is very similar to processes like casting; however, at a more microscopic level. Most fundamental solidification studies report that the microstructure evolution is a function of the temperature gradient (G) and growth rate (V) ahead of the microscopic solidification front. According to experimental [75], [76] and theoretical [77] analysis of solidification, the primary dendrite arm spacing of a solidified product is formulated as below:

$$\lambda_1 = A_1 G^{-n} V^{-m} \quad \textbf{(2.1)}$$

where λ_1 is the primary arm spacing, G is the average temperature gradient in front of tip of dendrite in liquid side, V is average solidification velocity, and A_1, m and n are constants. Regarding the second dendrite arm spacing, the most widely accepted expression for the relationship between λ_2 and cooling rate (GV) was proposed by Cahn and Haasen [78]:

$$\lambda_2 = B_1 (GV)^{-n} \quad \textbf{(2.2)}$$

where $B_1$and n are constants. Little is known about what controls the constant B_1, but it appears that it becomes smaller as the temperature interval between liquidus and solidus increases.

Thus, understanding of the relationships between a material's final microstructural and physical characteristics and conditions of solidification in LAM requires knowledge and control of the melt pool temperature and more importantly the cooling rate.

2.3.1 Melt Pool Temperature Analysis and Control in LAM

Early reports on monitoring systems using pyrometers [79]–[84] indicate their feasibility in observing changes in LAM and their application to real-time process control; they also highlight the complexity of the process. Since most measurements in LAM were recorded with pyrometers, which can only measure a point during the process, the majority of the research available in literature belongs to melt pool temperature measurements.

Griffith et al. [85] where one of the first to apply thermal contact and imaging techniques to monitor the thermal signature during LENS processing in 1999. A fine diameter (10 μm) C-type thermocouple was used initially to measure melt pool temperature at different passes of a hollow block [85]. They

also correlated residual stress and hardness of H13 steel with the thermal behavior of the LAM process. In-situ temperature measurements were later performed during LENS processing using a digital infrared camera and high speed visible data imaging. However, no correlation was obtained for microstructural evolutions with the thermal behavior.

Bi et al. [86] investigated the whole LAM thermal cycle for AISI 316L during the deposition of thin walls with a germanium-based thermometer. They measured the melt pool temperature in real time and observed that variation of the melt pool temperature and cooling rate results in dimension error, inhomogeneous microstructure and hardness. A set of original pyrometers and special diagnostic CCD-camera were applied by Doubenskaia et al. [87] for monitoring of Nd:YAG laser cladding with coaxial powder injection and on-line measurement of cladded layer melt pool temperature. They observed instabilities in the cladding zone with a bi-dimensional pyrometer because of varying operating parameters (powder feeding rate of WC-Co/Stellite). In a later study Doubenskaia [88] ran a comprehensive optical diagnostics on CO2 laser using a pyrometer and an infrared camera. They studied variations of brightness temperature measured by the pyrometer in the zone of laser impact versus laser cladding parameters.

Two types of high-temperature thermocouples (C-type and R-type) were successfully utilized to measure the thermal cycle and the temperature distributions for laser cladding process by Hu et al. [89]. The clad-zone temperatures under various processing conditions were between 1650 ℃ and 1800 ℃. Hua et al. [90], developed a temperature measurement system by using a two-color infrared thermometer. The influences of laser processing parameters such as powder feed rate, scanning velocity of laser beam, laser power, spot diameter, shielding gas flow rate and powder feeding position were investigated on the temperature of molten pool. A relationship between the molten pool temperature and the cladding thickness was also constructed by Hua et al. [90]. Lhospitalier et al. [91] calibrated thermal imaging of a charge coupled device camera equipped with infrared filters by a set of tungsten (W5-type) thermocouples. They measured the temperature distribution in the weld pool and near the melted zone.

Peyre et al. [92] developed a three-step analytical and numerical approach to predict the shapes of manufactured structures and thermal loadings induced by the DMD process. Their results were confirmed by comparisons with experimental thermocouple data and fast camera melt-pool recording. A two-dimensional thermal model was presented by Wang et al. [93] to predict the temperature distribution in the deposited metal for SS 316 during the LENS process as a function of time and process

parameters. The relative sensitivities of the thermal profiles and the molten pool size to the boundary conditions and laser powers were illustrated [93].

Zahng et al. [94] investigated the influence of thermal history on the microstructures and properties of a multilayer stainless steel 410 (SS 410) thin wall built by laser direct metal deposition (LDMD) process investigated experimentally and numerically. The results indicated that thermal history had an important effect on the microstructure, and consequently on the final properties [94]. Vasudevan et al. [95] carried out real-time monitoring of the weld pool using infrared thermography during gas tungsten arc welding (GTAW). Temperature profiles were measured on the plates using thermocouples in combination with IR thermography to determine the emissivity of the plate surface. For 316LN stainless steel weld joints, IR thermal signatures were acquired for various weld defects, such as lack of fusion, lack of penetration and tungsten inclusions, for use as reference signatures for on-line monitoring during GTA welding [95].

Few research groups have implemented closed-loop controllers to control the melt pool temperature in their cladding process. Song and Mazumder [96] presented a model predictive control system that controls the melt pool temperature. A dual-color pyrometer was used to monitor the melt pool temperature. The compensation for the lack of deposition with the closed-loop controller was demonstrated by cladding on a stepped surface. The controller successfully compensated for the lack of deposition by adjusting the laser power during laser cladding process.

Salehi and Brandt [74] developed a PID-based controller to monitor and control melt pool temperature during laser cladding. The quality of clad layer in terms of its dilution and the extent of HAZ was investigated, and it was shown that control of temperature alone will not produce desired cladding results. They indicated that controlling the melt pool size with another operating parameter – such as translation speed is also required to effectively control the process and quality of clad layer under a wide range of operating conditions [74].

2.3.2 Cooling Rate Analysis and Control in LAM

Although, there are numerous reports available in literature on melt pool temperature measurements, there are very few researchers who have reported in-situ cooling rate measurements in LAM. Griffith and Hofmeister [97] used thermal imaging and metallographic analysis to study Laser Engineered Net Shaping processing of 316 stainless steel and H13 tool steel. A 12-bit digital charge-couple device (CCD) camera was used to measure the radiant intensity from the sample at $650\ nm$ through the laser-

focusing objective. Thermal imaging was used to measure the temperatures, gradients and cooling rates around the melt pool with an offline algorithm. However, they [97] found it impractical to measure cooling rates with the thermal imaging system in real time due to complexities of the process. The length scale of the molten zone controls cooling rates during solidification in direct metal deposition. Griffith et al. [97] reported cooling rate values ranging from $200-6000\,Ks^{-1}$ at the solid-liquid interface, for molten zone ranges from $0.5\,mm$ in length to $1.5\,mm$.

Wang et al. [98] characterized the thermal behavior of the LENS process for SS 410 single wall build by using a two-wavelength imaging pyrometer. It was found that the maximum temperature in the molten pool is approximately 1600°C. They calculated a maximum offline cooling rate in the liquid-solid interface in the order of $10^3\ ℃s^{-1}$. It was observed that the molten pool size and cooling rate significantly depend on the travel velocity and the laser power.

Yamashita et al. [99] developed a novel temperature measurement method during laser welding by using two high-speed cameras and a two-color thermometry method. Both temperature distribution and history were measured precisely although, the cooling rate was quite high during laser welding.

Yu et al. [100] used two kinds of methods on temperature measurement for AISI 304: (1) real-time tracking for online measurement of the melt pool, in which the sensor moved together with the laser head and aimed at the molten pool, and (2) fixed-point monitoring for offline measurement of the cooling rate, in which the sensor aimed at the midpoint of the track without moving. They analyzed multi-layer depositions on a wall. The cooling time decreased with decreasing the powder feeding rate and increasing the laser power and scanning velocity in single layer deposition process. In multi-layer deposition process, the cooling rate increased with increasing the number of the deposition layers.

To the author's knowledge there are no reports available in literature on closed-loop control of the cooling rate. There have been a couple of attempts to monitor the cooling rate in real time; however, none were successful. In fact, there are various reports in literature that have indicated the great difficulty of real time cooling rate calculations in LAM due to the high melt pool temperature and the rapid solidification process.

2.4 Solidification in LAM

Since LAM is one of the many solidification processes available in the industry, understanding the theory of solidification plays a crucial role in predicting and controlling the process. Solidification

conditions determine the clad microstructure and should be a determining factor in predicting morphology patterns.

The LAM process delivers a localized heat source and short interaction time. Thus, there are rapid solidification rates, which are mainly caused by heat conduction of the clad and substrate. The solidification rate can be formulated as below [1]:

$$V_S = Vcos(\theta) \tag{2.3}$$

where V_S is the solidification rate, V is the scan speed and θ is the angle between the substrate motion and the normal vector of the liquid/solid surface at a particular point along the solid/liquid interface as illustrated in Figure 2-3. The solidification rate is zero when θ is 90° (at the substrate interface) and equal to the substrate motion speed (maximum) at the top of the clad. Therefore, low cooling rates are expected at the clad substrate interface, and a high cooling rates on top of the clad.

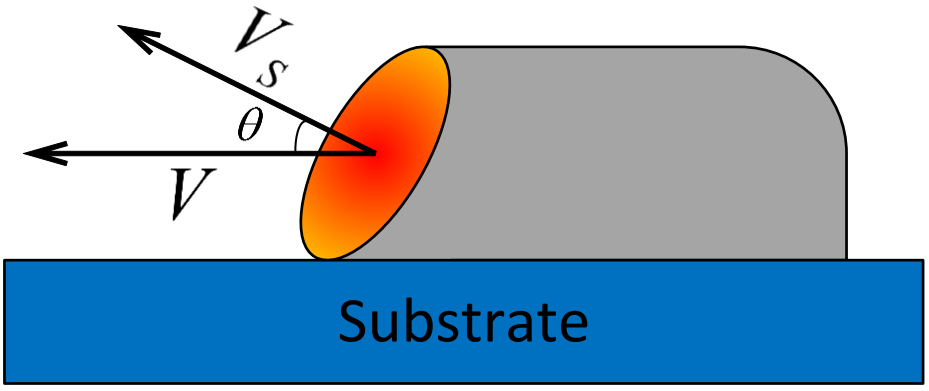

Figure 2-3 Scan speed and solidification rate vectors.

Since the laser provides highly focused heat, it causes high local temperatures in the melt pool region, and thus a large positive temperature gradient can be expected in the clad. This temperature gradient is maximal on the clad/substrate surface and minimal at the top of the clad [1].

To obtain quantitative expressions for the solute distributions, a quantity known as the partition coefficient, k, is used:

$$k = \frac{C_S}{C_L} \tag{2.4}$$

in which C_S and C_L are the concentrations at the solidus and liquidus phases at a given temperature. This ration determines the extent to which solute is ejected into the liquid during solidification.

During the solidification of an alloy with partition coefficient less than 1($k < 1$), solute atoms are rejected in front of the solid/liquid interface. The concentration of the solute increases until the solution reaches a steady state condition. In this steady state, the freezing temperature ahead of the liquid/solid interface is determined by the composition of the liquid (the liquidus line). If the temperature near the liquid/solid interface is equal or greater than the liquidus temperature of Figure 2-4, no constitutionally super-cooled region exists, preventing dendrite formation and creating planar growth. The minimum temperature gradient which causes planar growth is the critical temperature gradient G_c. If the real temperature gradient is greater than G_c, planar growth is stable. If the actual temperature gradient is lower than G_c, the growth of protrusions may occur in the molten pool in a cellular or dendrite form. Since the temperature gradient in the molten pool of the clad decreases from the bottom to the top of the clad, various degrees of constitutional supercooling are possible throughout the thickness of the clad melt pool. Since both the temperature gradients and the solidification rate vary with distance in the melt pool, solidification conditions can vary significantly from the bottom to the top of the clad.

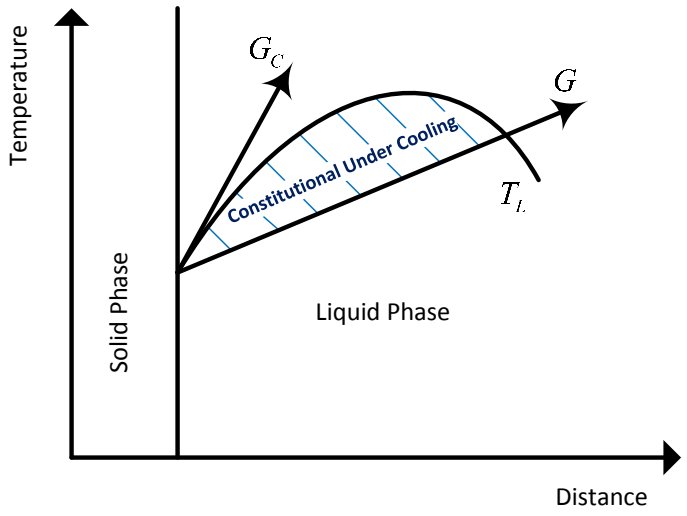

Figure 2-4 Constitutional under cooling at the solid\liquid interface.

2.5 Phase Diagrams

Stainless Steel (SS) type 316L and 303, which are well known austenitic stainless steels are the primary materials in this research due to their broad applications and known microstructure. The binary and

ternary diagrams of austenitic steel will be presented in this section. These diagrams identify the phases expected to appear for different material compositions and temperatures. Although, LAM is a non-equilibrium process, phase diagrams are useful guides to interpret and estimate the final outcome of the process.

2.5.1 Iron-Chromium-Nickel Ternary Phase Diagram

The Fe-Cr-Ni ternary system provides the basis for predicting microstructure and primary modes of solidification. Since most commercial stainless steel are composed of 16-25 wt% Cr and 8-20 wt% Ni, their compositions are limited to the Fe-rich section of the ternary diagram. The liquidus and solidus surface of the system can be represented by a series of isotherms as shown in Figure 2-5. Note that the liquidus surface exhibits a single, dark line that runs from near the Fe-rich apex of the triangle to the Cr-Ni side. This line separates compositions that solid as primary ferrite (above and to the left) from compositions that solidify as primary austenite. At approximately 48Cr-44Ni-8Fe, a ternary eutectic point exists. Alloy compositions lying on the Cr-rich side of this line will solidify predominantly as BCC δ-ferrite while those on the Ni-rich side of this line will solidify predominantly as FCC γ-austenite.

The solidus surface exhibits two dark lines that run from near the Fe-rich apex to the Cr-Ni-rich side of the diagram. Between these two lines the austenite and ferrite phases coexist with liquid just above the solidus, but only with one another just below the solidus. This region separates the ferrite and austenite single-phase fields below the solidus. Note that these lines terminate at the ternary eutectic point. Arrows on these lines represent the direction of decreasing temperature.

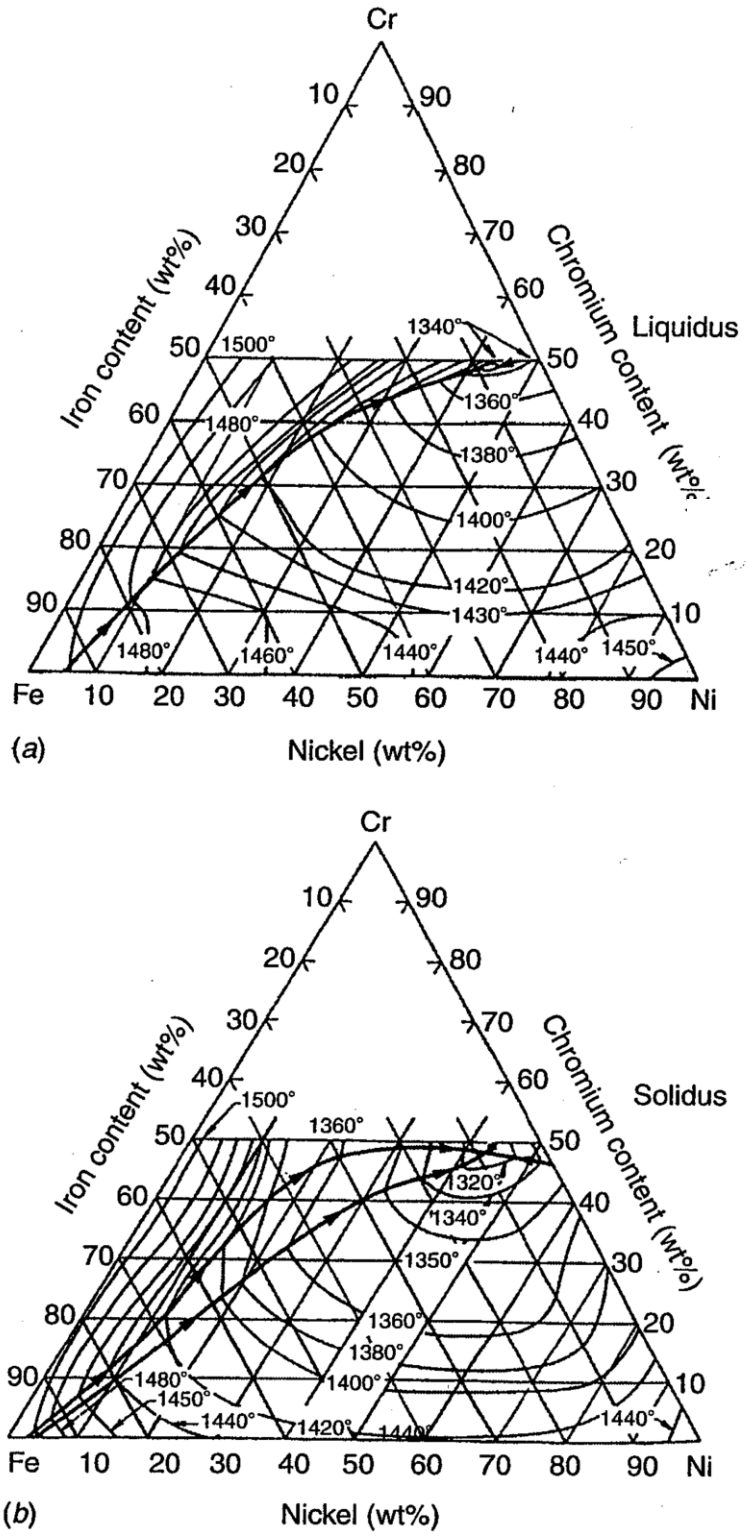

Figure 2-5 Liquidus and solidus projections of the Fe-Cr-Ni ternary system [101].

2.5.2 Chromium-Nickel Binary Phase Diagram

If a constant Fe section of the ternary phase diagram is extracted from the liquidus to room temperature, a pseudobinary Fe-Cr-Ni phase diagram can be generated. As shown in Figure 2-6, the ternary phase diagram Fe-Cr-Ni has been cut at 70 wt% Fe and at 60 wt% Fe cross sections. Since this is a ternary system, the phase fields exist in three dimensions, resulting in three-phase fields that cannot occur on a standard binary phase diagram.

A small triangular region exists between the solidus and liquidus lines in the Cr-Ni binary phase diagrams. This is the three-phase austenite (γ) + ferrite(δ) + liquid region that separates alloys that solidify as austenite (to the left) from those that solidify as ferrite (to the right). In the solid state, the ferrite is stable at elevated temperature at chromium contents greater than 20 wt%.

As the temperature decreases, this ferrite will transform partially to austenite in the range 20 to 25 wt%. Alloys that solidify as austenite (to the left of the three-phase triangle) remain as austenite upon cooling to room temperature. Alloys that solidify as ferrite at compositions just to the right of the three-phase triangle, must cool through the two-phase austenite + ferrite region. This results in the transformation of some of the ferrite to austenite. At compositions farther to the right of the triangle (higher Cr/Ni ratios) ferrite will become increasingly stable, until ultimately a fully ferritic structure will exist toward the far right side of each diagram. These diagrams are used in Chapter 4 to explain the phase transformations and microstructure evolution in deposition of the austenitic 316L stainless steel.

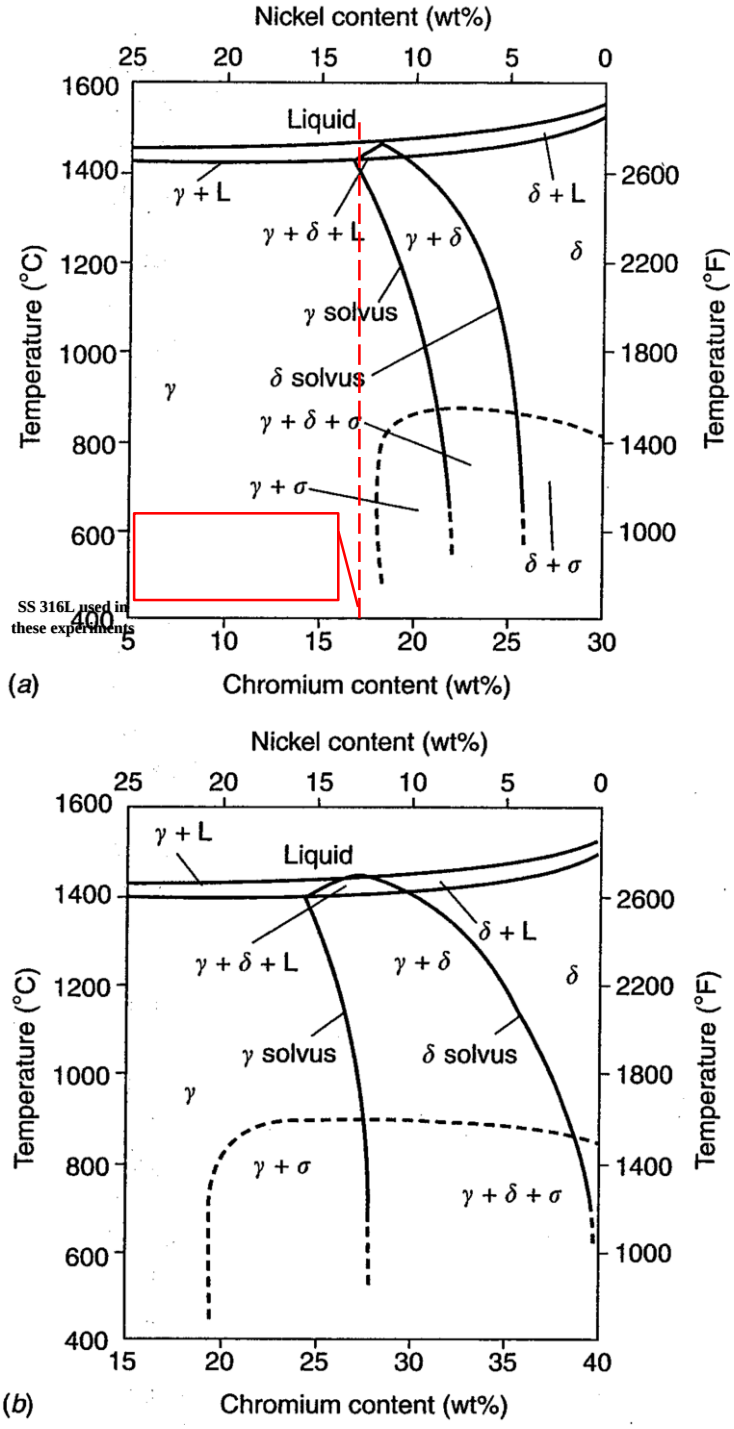

Figure 2-6 Pseudobinary sections of the Fe-Cr-Ni ternary system at (a) 70% Fe and (b) 60% Fe [102].

Chapter 3
Experimental Setup

3.1 Introduction

An automated Laser Additive Manufacturing (LAM) system is composed of several high-tech instruments. The main components are a high power laser, powder feeder, multi-axes CNC machine or a robotic arm, nozzle and an intelligent controller consisted of data acquisition systems and sensors. In this chapter, the LAM setup configured in the Automated Laser Fabrication (ALFa) lab at University of Waterloo will be described. The chapter begins with information provided on infrared imaging techniques and devices. Different programing techniques and acquisition devices are addressed in full detail. Finally, a closed-loop thermal feedback control system is developed and discussed based on thermal information acquired by thermography techniques.

3.2 Experimental Setup

A schematic view of the state of the art LAM apparatus used in this research is illustrated in Figure 3-1.

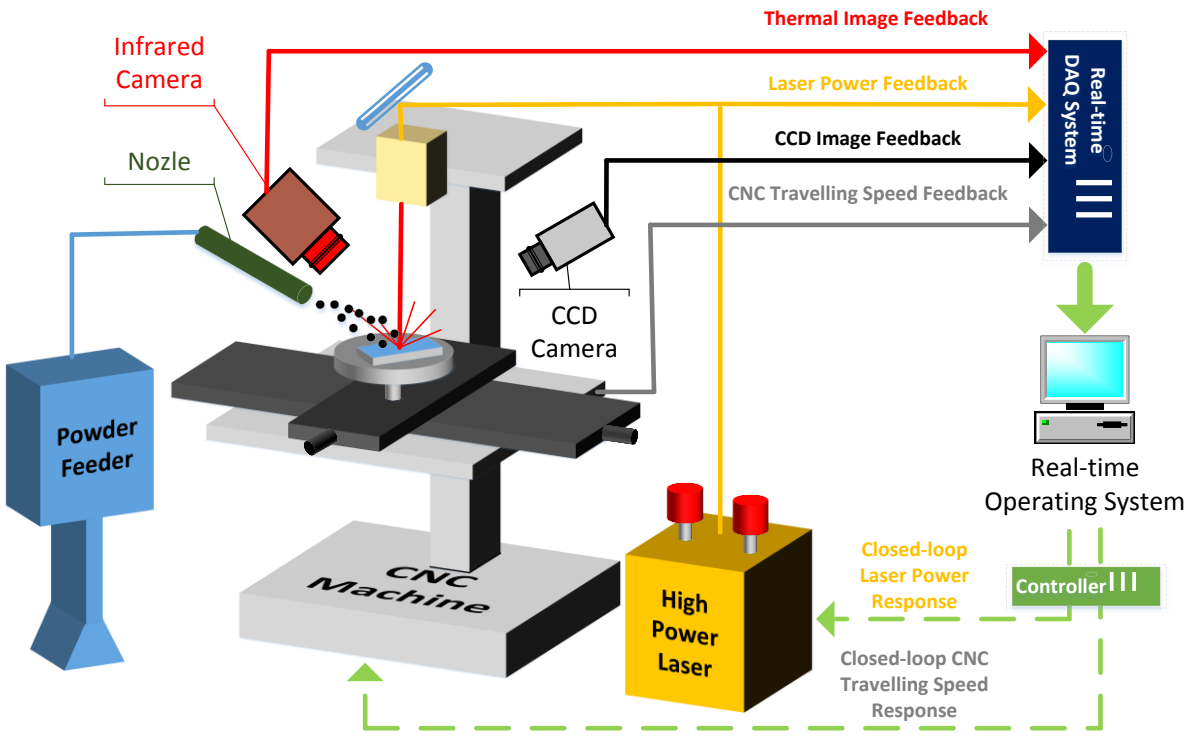

Figure 3-1 Experimental setup in Automated Laser Fabrication (ALFa) lab.

Each piece of equipment is described briefly as follows.

A. High power laser: An IPG fiber laser YLR-1000-IC operated in continuous mode with a maximum power of 1.1 kW is utilized as the energy source. The fiber laser operates under a wavelength of 1070 nm.

B. Powder feeder: A Sulzer Metco TWIN 10-C powder feeder with two 1.5 L hoppers are used to control the powder mass feed rate and the flow of argon shielding gas. The feed rate and flow rate are controlled manually using the onboard controllers installed on the system. A wide range of particle sizes can be sprayed at feed rates varying from 2 g/min to 150 g/min.

C. CNC machine: A 5-axes CNC machine is used as the positioning device. Two additional rotational axes were installed on a 3-axes Fadal VMC 3016 to produce the required motions. The CNC machine and its axes are illustrated in Figure 3-2. An additional moving axis was also installed on the laser head, vertically aligning the head in order to control the laser spot size on the substrate.

D. Nozzle: The powder is fed through a lateral nozzle onto the substrate with input diameter 1.6 mm and output diameter 3.1 mm. The nozzle is installed on a mechanism with four degrees of freedom, providing good positioning for focusing the powder onto the laser beam spot.

E. Real-time operating system: Online data is acquired and processed using a National Instruments (NI) real time platform and Labview. An NI-IMAQ module is utilized to grab images from the Infrared (IR) and Charged Couple Device (CCD) cameras as input signals. The CCD images are acquired by an NI PCI-1409 (NI-IMAQ) and the IR images are acquired separately through an imaging card developed by Jenoptik. An NI Motion module is installed to apply controller signals to the system. CNC travelling speed, laser power and laser spot size are controlled using an NI PCI-7340.

Figure 3-2 5-axes CNC machine used as the motion device in the setup.

Referring to Figure 3-1, the process starts when the laser produces a laser beam with the desired power. This beam is transferred to the laser head installed on the CNC machine through the fiber optics. The laser beam is then shot on to the substrate producing a melt pool with a desired spot diameter. As the beam heats up the melt pool the powder feeder sprays the required amount of powder onto the melt pool, also feeding argon shielding gas to prevent oxidation. When the powder stream is fed into the melt pool the powder particles and a thin layer of substrate are melted. The CNC machine moves the substrate, producing a desired trajectory of the deposition on the substrate. Due to rapid cooling rates and localized heat zones, a strong bonding is formed between the deposited layer and the substrate.

During the process, the IR and CCD cameras capture images of the process at high frequency rates and send them to the NI IMAQ module for image processing and analysis. The images are analyzed and processed in real time by Labview. A controller monitors the signals and generates a desired control action for the CNC table feed rate, laser power or laser spot size. The NI Motion Controller module is used to send the controlling action commands to the system in order to produce the required motions for the desired output.

3.3 Infrared Image Acquisition System

Many material and mechanical properties of the deposited layer are related to solidification and thermal properties of the LAM process. To control these properties during solidification, a great amount of thermal information is required from the melt pool and its surroundings. As discussed earlier in

Section 2.3 there are a variety of devices available to capture the thermal history of a process. However, only a certain number of these devices are applicable to the LAM process and its applications.

Contact temperature-measuring devices such as thermocouples are not able to capture real time LAM melt pool temperatures since they can only withstand temperatures of up to 1600 ℃ (R- and S- type). In LAM, temperatures inside the melt pool reach 2500 ℃ or even higher. Furthermore, since these devices have to be always connected to the measuring body, there are only a few joining methods that could withstand such high temperatures without breaking down. In addition, connecting thermocouples to the substrate may damage the work piece. On the other hand, thermal gradient information of the LAM process requires multiple point measurements in real time, whereas, thermocouples are only suitable for single point measurements. Thus, thermocouples are only suitable for measurements outside the melt pool that are not of high importance.

Pyrometers (thermometers), which are the most common non-contact temperature-measuring devices are also not suitable for the LAM process. The more important metallurgical properties such as microstructure and morphology are greatly related to the solidification cooling rate rather than the melt pool temperature. To capture the cooling rate of the melt pool in real time, constant temperature measurements of two or more points in a single frame are required, whereas, it is only possible to measure one point at a frame with a pyrometer. Thus, pyrometers are not the best options for the purpose of controlling mechanical and metallurgical properties in LAM.

As discussed in Section 2.3 thermal infrared (IR) cameras are another type of non-contact temperature measuring devices. Unlike thermocouples, they do not need to be connected to the work piece for measurement. Thus, IR cameras are suitable for measuring high temperatures inside the melt pool with great accuracy. Moreover, due to the non-destructive and non-contact nature of the IR technique, there are no limitations in measurement of different geometries and no destruction on the work piece. On the other hand, compared to a pyrometer, IR cameras can provide a thermal image over a large area in each frame rather than one point measurements, which could only capture the melt pool temperature. Hence, crucial thermal information of the LAM process such as cooling rates of different points can be achieved through IR cameras.

IR cameras have several advantages compared to other contact and non-contact techniques that are specifically suitable for the LAM application. These advantages of IR imaging are summarized as follows:

- Provides a thermal image, thus temperatures over a large area can be compared
- Ability to capture cooling rate and melt pool temperature in real time
- Capable of capturing moving heat sources in real-time with high response time
- Provides thermal information of inside cavities and hard-to-access locations
- Wide range of temperature measurements ($0 - 3000$ ℃)
- Non-contact technique
- Non-destructive method

Considering these many advantages, a high temperature IR camera was used in the current setup to provide thermal imaging of the process. A Jenoptik IR-TCM 384 camera module is used to monitor the LAM process. The IR camera and its specifications are shown in Figure 3-3 and Table 3-1.

Figure 3-3 Jenoptik IR-TCM 384 infrared camera.

Table 3-1 Technical data of the Jenoptik IR-TCM 384 IR camera.

Image Resolution:	Standard: 384 x 288 RE Mode: 768 x 576 (optional)
Interfaces:	IEEE-1394 (FireWire), S-/C-Video, VGA, RS-232 Gigabit-Ethernet (option) WLAN (option)
Measuring accuracy:	± 1.5 K (0 °C ... +100 °C), otherwise ± 2 K / ± 2 %
Spectral range:	7.5 µm ... 14 µm
Temperature measurement range:	Standard: -40 °C ... +300 °C Optional: up to +2000 °C
Temperature resolution:	NETD <70mK with filtering: NETD <30 mK

The IR camera is connected to the LAM setup through an IEEE-1394 interface. Images were then captured and processed by two different software:

1. **Vario Capture/Vario Analyzer:** The Vario Cpature software saves thermal images in conventional .jpg format or .irb format, which can later be analyzed using the Vario Analyzer. However, these software are only applicable for post processing of thermal data and are not sufficient for real time processing that is required for control purposes.
2. **Labview:** Using a toolbox developed by Jenoptik, raw thermal images were transferred to Labview where they could be processed online during the process for control applications. Hence, using the Labview interface, thermal images were received, analyzed and processed in real time to process input and output signals for the proposed controllers.

Although, IR cameras have all the required characteristics for acquisition and processing of thermal information during the LAM process, they have one minor drawback for the current application, which is discussed in the following section.

3.3.1 Emissivity

Emissivity is defined as the relative ability of a material's surface to emit thermal energy. Every object having an absolute temperature above $0\ K$ emits thermal radiation. A black body is the most ideal in terms of emitting thermal radiation, since it absorbs every incident radiation regardless of its direction and wavelength. For a given temperature and wavelength, no other body can emit more energy than a black body. Therefore, a black body possesses the maximum emissivity value of one ($\varepsilon_b = 1$). Black bodies are idealizations and no real object can emit this amount of maximum energy. Hence, all real bodies have an emissivity value of $0 < \varepsilon < 1$. The real emission of any object can, however, be calculated by multiplying the black body radiation with a relative quantity that describes the object's effectiveness in emitting thermal radiation, the emissivity ε. In other words, the emissivity of an object is the ratio of the amount of radiation actually emitted from the surface to that emitted from a blackbody (with the same material) at the same temperature [103].

Although, emissivity $\varepsilon(\lambda, T)$ is a constant value for most practical applications, in special material and applications it is a function of the wavelength being measured λ, and the body temperature T. Since, the IR camera only measures the temperature in one constant wavelength in the current LAM setup, the emissivity will not change with respect to the wavelength. However, the emissivity of metallic powders deposited during LAM (such as stainless steel and titanium) are highly dependent on temperature, especially at the elevated temperatures of the LAM process ($800 - 2000$ ℃). The change of emissivity with temperature in steel is attributed to the formation of an oxide layer on the surface of the steel as its temperature increases [104]. This change of emissivity may lead to errors in capturing the real body temperature as high as 100 ℉ [105]. To address the difficulty of unknown and changing emissivity, instrument manufacturers have devised the two-wavelength and multi-wavelength (Spectro Pyrometers) pyrometers [105]. These devices capture the emissivity at two or more wavelengths, eliminating the requirement of emissivity for calculation of real body temperatures.

While emissivity variation is an undesirable phenomena in IR measurements of the LAM process, it is not disruptive by any means to the current applications of this research. The main aim of the current research is to monitor the thermal history variations of LAM, in order to control the metallurgical output of the process. As stated earlier in Section 2.2, material characteristics such as microstructure and morphology are greatly related to cooling rate, which is only obtained through measurement of thermal variations and not real body temperatures. Moreover, for applying certain type of controllers, only monitoring variations in temperature will be sufficient. Thus, there is no need for information on exact

real body temperatures for the specific controlling applications of this research. Emissivity changes are therefore, not important in acquiring and analyzing thermal data for the current application. Hence, an average emissivity is calculated for the material being deposited and this emissivity is kept constant throughout the whole process and real-time temperature calculations.

3.4 Thermography Analysis and Processing Techniques

The IR camera module IR-TCM 384 captures infrared images of 384×288 pixel resolution that are collected and processed online using Labview. A raw image captured during deposition of a single clad line is shown in Figure 3-4. These images only provide temperatures of each pixel and thus, require processing and analysis to be functional for control applications.

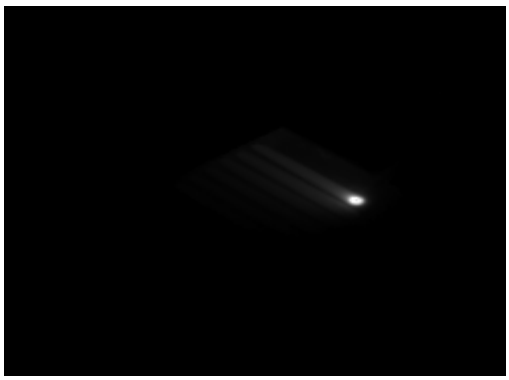

Figure 3-4 Sample of thermal images captured by the IR camera.

Since the proposed controller is supposed to control material properties, it requires information from output parameters that influence these properties. Cooling rate and melt pool temperature were recognized as the two most important factors, which influence the clad microstructure. Thus, an algorithm is required to extract melt pool temperature and cooling rate in real time using the thermal images (Figure 3-4). Apart from the melt pool and cooling rate, a thermal map of the neighboring points on the clad line and outside will provide additional information of the microstructure evolution.

An algorithm was developed in Labview to obtain the melt pool temperature, cooling rate and a complete thermal map during deposition of single-line claddings from the raw IR images shown in Figure 3-4. The data were acquired in a step by step process as follows:

3.4.1 Finding Melt Pool Temperature

The IR images were grabbed in an 8 bit grey scale format with a resolution of 384 × 288 pixel. As illustrated in Figure 3-4, the images include two main regions, the dark area, which represents the background or the surrounding of the clad line and the bright area, which represents the clad line and its melt pool. Since the images are stored in an 8 bit format, each pixel has an RGB value 0f $0 - 255$. The intensity of each pixel is directly related to its temperature, the greater the RGB value (the brighter the pixel) the higher the temperature. To obtain the melt pool temperature and its location, the image is converted into a two-dimensional array as shown in Figure 3-5. The array has a size of $X \times Y$ in which X is the total number of pixel rows and Y is the total number of pixel columns of the image. In case of a 384×288 pixel image, $X = 384$ and $Y = 288$. Each element of the array has an assigned row r, and column c, with a position vector (c, r), which is shown in Figure 3-5. The size of each element $I_{c,r}$ is equal to the RGB value of the equivalent pixel. By converting the image to an array, one can apply all the analysis, display and array operators available in Labview to the image data.

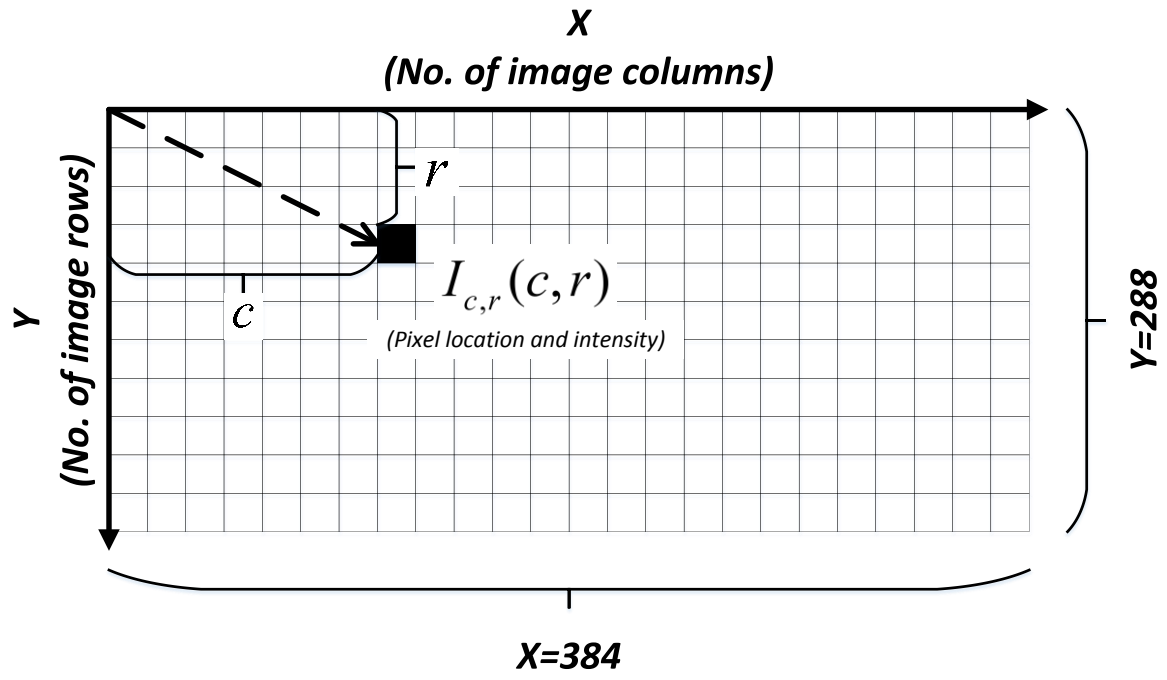

Figure 3-5 Two-dimensional array of the IR image.

The main approach to find the melt pool temperature and its location is to consider the setup of the IR camera and laser beam with respect to each other. In the setup, the laser head is placed on a fixed

position and the work piece is moved by the CNC table. The IR camera is also installed on a fixed position on the CNC machine, experiencing no motion during deposition. The laser beam and the IR camera are therefore, static with no motion with respect to each other. Hence, the instantaneous melt pool vector (c_m, r_m) always remain the same in the captured images since, not the laser beam nor the IR camera move with respect to each other. The pixel with the maximum RGB value I_{max}, represents the melt pool.

The instantaneous melt pool vector (c_m, r_m) can be obtained in advance before the deposition, by rapidly applying an on/off to the laser and finding the position of the maximum element (c_{max_0}, r_{max_0}) in the image array. Since this location of the melt pool pixel is fixed with respect to the IR camera, it should also be fixed inside the image. Hence, the maximum element vector measured initially (c_{max_0}, r_{max_0}), is assumed to be equal to the instantaneous melt pool vector (c_m, r_m) in later images. As a result, as each image is grabbed and converted to an array, the RGB value I_0, of the element located at (c_{max_0}, r_{max_0}) is obtained and fed through a convertor block to obtain the pixel's temperature. This temperature will be the representative of the melt pool's temperature T_m.

While this method is straight forward, experiments showed that the maximum element vector in the array is not always fixed. Since the whole melt pool area occupies a couple of pixels in the image, the pixel with the maximum RGB value lies inside one of these pixels. Experiments showed that the instantaneous maximum element vector (c_{max}, r_{max}) varies with a tolerance of ± 1 pixels with respect to the initial location (c_{max_0}, r_{max_0}). Therefore, the instantaneous maximum temperature might not always be located at (c_{max_0}, r_{max_0}), whereas, the melt pool temperature should always be the maximum element of each image. To fix this error and also to reduce noise in measurements, after the initial maximum vector (c_{max_0}, r_{max_0}) is located in each image, a 9×1 array of the temperature values of the initial pixel T_0 and its eight surrounding pixels is formed (Figure 3-5). The maximum three temperatures of the initial pixel and its neighboring pixels are extracted and averaged to represent the melt pool temperature at each image. Thus, reducing noise and canceling out any miss-selection of the melt pool pixel.

3.4.2 Calculation of Cooling Rate

After the melt pool temperature is obtained, the program has to provide information on the cooling rate. Figure 3-6 illustrates two thermal images at times $t_1 = t_0$ and $t_2 = t_0 + n\tau$, in which τ is the sampling time and n is the total number of sampling times elapsed after initial time t_0. Point P_m is the

instantaneous melt pool position that has a fixed position vector (c_m, r_m) in all the captured images. Point P_1 is a fixed point on the clad line. At time t_0 (Figure 3-6a), P_1 is located inside the melt pool having a position vector (c_m, r_m) with temperature $T_0 = T_m$. After $n\tau$ seconds (Figure 3-6b), point P_1 moves out of the melt pool having a new position vector (c_P, r_P) inside the acquired image with a temperature T_n. As stated earlier in Section 3.4.1 and shown in Figure 3-6, the melt pool vector (c_m, r_m) is fixed inside the image array, whereas, the location of a fixed point P_1, (c_P, r_P), on the clad line is moving. The two factors influencing the microstructure at point P_1 are: (1) melt pool temperature that is measured as T_0 and (2) cooling rate C_P. For point P_1 the cooling rate is defined as:

$$C_P = \frac{\Delta T}{\Delta t} = \frac{T_n - T_0}{n\tau} \tag{3.1}$$

In Eq.(3.1), the only unknown is T_n. In order to calculate T_n, the final position vector of P_1, (c_P, r_P), should be known.

According to Figure 3-6, the total number of pixels point P_1 has traveled from time t_0 to $t_0 + n\tau_n$ is determined as follows:

$$\begin{aligned} N_r^n &= \frac{[(v_1\tau_1 + v_2\tau_2 + \cdots + v_n\tau_n)\cos\alpha]}{d} \\ N_c^n &= \frac{[(v_1\tau_1 + v_2\tau_2 + \cdots + v_n\tau_n)\sin\alpha]}{d} \end{aligned} \tag{3.2}$$

in which, $(v_1, v_2, \dots, v_n)$ are the CNC machine speeds at each sample time $(\tau_1, \tau_2, \dots, \tau_n)$, n is the total number of sample times, d is the dimension each pixel occupies on the clad line in mm, α is the angle of the clad line, N_r^n is the total number of row pixels traveled and N_c^n is the total number of column pixels traveled. As shown in Figure 3-6b, N_c^n and N_r^n form a transfer vector (N_c^n, N_r^n) for point P_1, which gives the final location of P_1, (c_P, r_P), with respect to the instantaneous melt pool position at time $t_0 + n\tau_n$. Since the experiments are held at equal sampling times; $\tau = \tau_1 = \tau_2 = \tau_n$, Eq.(3.2) is summarized as follows:

$$\begin{aligned} N_r^n &= \frac{[(v_1 + v_2 + \cdots + v_n)\tau\cos\alpha]}{d} \\ N_c^n &= \frac{[(v_1 + v_2 + \cdots + v_n)\tau\sin\alpha]}{d} \end{aligned} \tag{3.3}$$

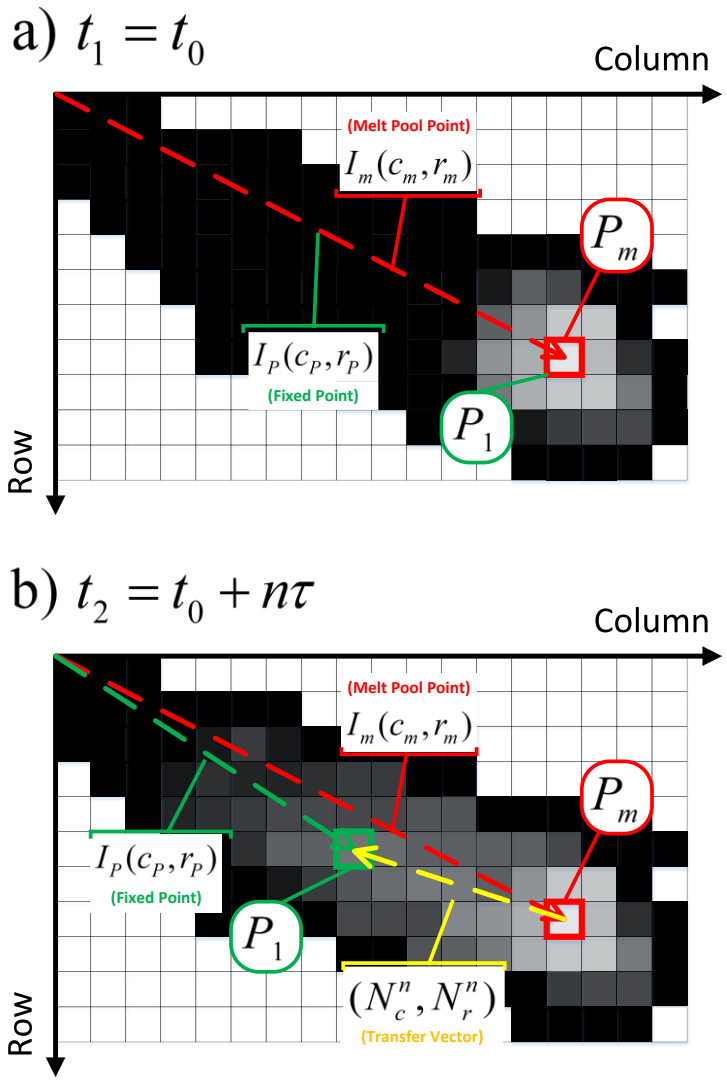

Figure 3-6 Movement of a constant point on the clad line in consecutive images.

Since the melt pool pixel has a fixed position at every image it is depicted as the reference point in the image array for obtaining the final fixed point location (c_P, r_P). When the transfer vector is obtained by Eq.(3.3), it is added to the melt pool vector (c_m, r_m) to obtain the current location of point P_1:

$$\begin{bmatrix} c_P^n \\ r_P^n \end{bmatrix} = \begin{bmatrix} c_m \\ r_m \end{bmatrix} + \begin{bmatrix} N_c^n \\ N_r^n \end{bmatrix} \tag{3.4}$$

where (c_P^n, r_P^n) is the position vector for P_1 at time $t_0 + n\tau$. Hence, the new location (c_P^n, r_P^n) is updated after n sample times using Eq.(3.3) and Eq.(3.4). As (c_P^n, r_P^n) is obtained at each step, it is fed through the convertor block to obtain the temperature T_n of point P_1 at time $t_0 + n\tau$. Consequently, the

thermal history ($T_0,\ T_1, \dots ,\ T_n$) of any fixed point P_1 on the clade line or outside can be derived using Eq.(3.3) and Eq.(3.4).

The thermal history of a random point P_1 on the middle of a clad line was measured experimentally to verify the algorithm described above. Results shown in Figure 3-7 are for a stainless steel deposition that will be used throughout this research. As it can observed in Figure 3-7, the cooling of point P_1 has a pseudo-linear and nonlinear region. Although, the pseudo-linear region is originally a stepped profile, it is interpolated as a linear line below and above the melt pool temperature for easier interpretation and analysis. The linear section of the solidification process is crucial in determining the microstructure of a solidified region. Thus, in order to obtain the cooling rate of the linear region, only the duration of the linear section t_L, is required and the temperatures forming the nonlinear section are of no interest.

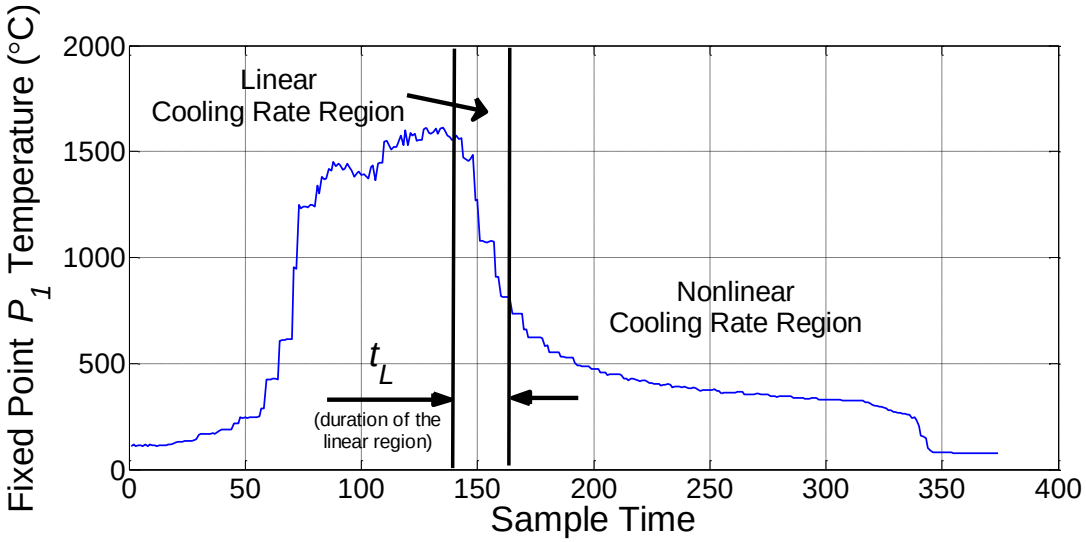

Figure 3-7 Thermal history of a fixed point P_1 during deposition.

The current program has a sampling time $\tau = 0.0625\ s$. Several thermal history measurements similar to Figure 3-7 were performed to determine the duration of the linear cooling region t_L. Experiments indicated that the linear cooling region of several lines had an average duration of $t_L = 0.975\ s$. Thus, for Eq.(3.1) to be representing the cooling rate of the linear region the following has to be satisfied:

$$\Delta t = t_L \qquad \textbf{(3.5)}$$

As a result, $\Delta t = 0.975\ s$, and if Δt is greater than $0.975\ s$, the cooling rate C_P falls into the nonlinear region, which is of no interest to the current application of microstructure control. Since $\Delta t = n\tau$ and

$\tau = 0.0625\ s$, consequently $n\tau = 0.975$ and $n = 15$. With $n = 15$ meaning that the linear cooling rate of any fixed point P_1 will lie between 1 to 15 consecutive sampling times. Therefore, for Eq.(3.1) to be applicable for calculating the linear cooling rate of any fixed point P_1, the equation should be revised as follows:

$$C_{PL} = \frac{T_{15} - T_0}{15\tau} \tag{3.6}$$

The above equation indicates that after $n = 15$ iterations (or sample times) the temperature of point P_1 should be calculated as T_{15}, and inserted into Eq.(3.6) to obtain the linear cooling of any fixed point P_1. Eq.(3.6) only provides linear cooling rate of one fixed point on the clade line, whereas, for the current application an updating cooling rate in real time is required. Therefore, Eq.(3.6) has to be converted to an updating cooling rate in real time.

If in Eq.(3.3), the complete speed vector $(v_1, v_2, \dots, v_n)$, is replaced by the speeds of the last 15 sample times; $(v_{n-15}, v_{n-14}, \dots, v_{n-1})$, the following transfer vector is yield:

$$\begin{aligned} N_r^{15} &= \frac{[(v_{n-15} + v_{n-14} + \cdots + v_{n-1})\tau \cos\alpha]}{d} \\ N_c^{15} &= \frac{[(v_{n-15} + v_{n-14} + \cdots + v_{n-1})\tau \sin\alpha]}{d} \end{aligned} \tag{3.7}$$

In the above equation, (N_c^{15}, N_r^{15}) is a transfer vector that will provide the current location of a previous melt pool at time $t_0 + t_L$. This new location is exactly the place where the decreasing temperature of point P_1 lies inside the linear cooling rate region. In order to obtain the new location of the previous melt pool at time $t_0 + t_L$, Eq.(3.4) is rewritten as follows:

$$\begin{bmatrix} c_p^{15} \\ r_p^{15} \end{bmatrix} = \begin{bmatrix} c_m \\ r_m \end{bmatrix} + \begin{bmatrix} N_c^{15} \\ N_r^{15} \end{bmatrix} \tag{3.8}$$

where (c_P^{15}, r_P^{15}) is the new location of the previous melt pool point P_m after 15τ seconds (or t_L seconds) of cooling. Thus, (c_P^{15}, r_P^{15}) is fed into the convertor block to obtain temperature T_{15} of a tracking point P_t after 15τ seconds. Finally, T_{15} is inserted into Eq.(3.6) to obtain the linear cooling rate of a tracking point P_t in real time.

To obtain the linear cooling rate (Eq.(3.6)) in real time, the travel speed vector $(v_{n-15}, v_{n-14}, \dots, v_{n-1})$ is always updated with the last 15 travel speeds of the CNC machine. As a result, Eq.(3.8) provides the location of a moving tracking point P_t, which is always tracking the current

melt pool location and providing the location and temperature of a previous melt pool after 15τ seconds (or t_L seconds) of cooling and solidification. As a result, after each sample time, Eq.(3.6) will provide an updated real time cooling rate. However, output cooling rate has a delay of $15\tau = 0.9375\ s$, since this time has to elapse initially for Eq.(4.3) and Eq.(3.8) to obtain the new location of the first melt pool.

3.4.3 Obtaining a Thermal Map

Although, melt pool temperature and cooling rate would provide adequate information for microstructural analysis, additional thermal information of other points will also be helpful in the analysis. A thermal map consisting of all the points on the clad line and inside the heat affected zone will be essential for validating online measurements and supporting experimental results. Thus, part of the developed program created and stored a thermal map of the process at each sample time. In order to obtain a thermal map, position vectors of all fixed points on the work piece such as P_1 in Figure 3-6 are required. Since, calculation of all the fixed point position vectors is computationally expensive for the system, only one position vector for one fixed point was extracted and all other fixed points were obtained with respect to that point. This initial fixed point will serve as a reference point in the image coordinate system for all other thermal points required in the thermal map.

Using Eq.(3.3) and Eq.(3.4), the location of a constant point P_1 is obtained at each sample time. Point P_1 will serve as the reference in the coordinate system for all other fixed points on the clad line and heat affected zone. Thus, 1D, 2D and 3D thermal maps of the clad line and the neighboring heat affected zones are extracted as shown schematically in Figure 3-8, Figure 3-9 and Figure 3-10.

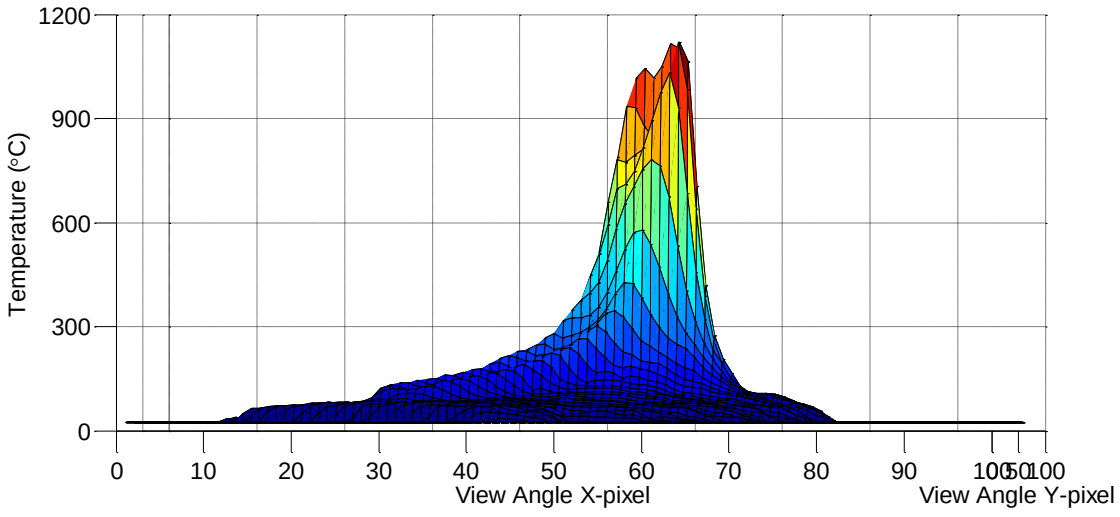

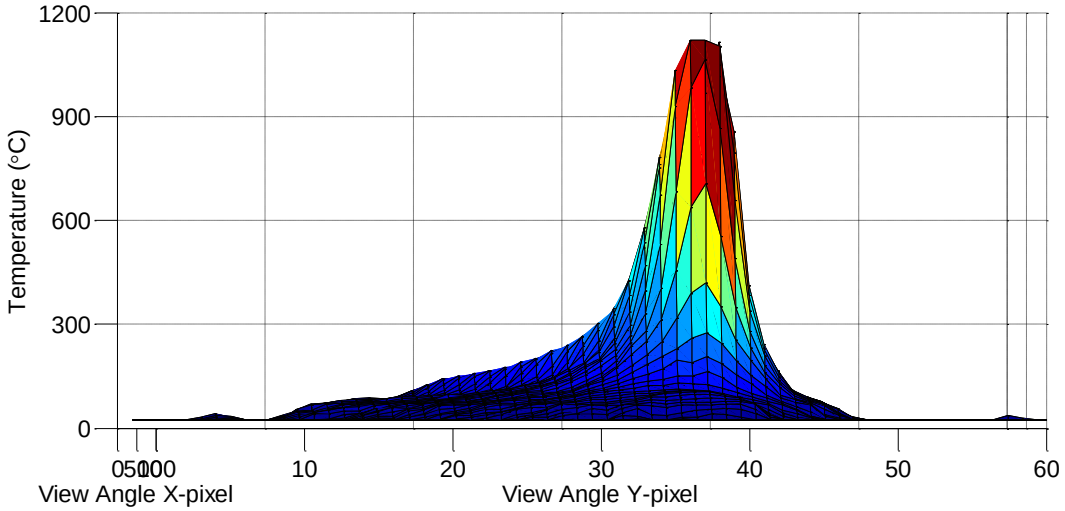

Figure 3-8 1D thermal map of a clad line in X and Y coordinate systems..

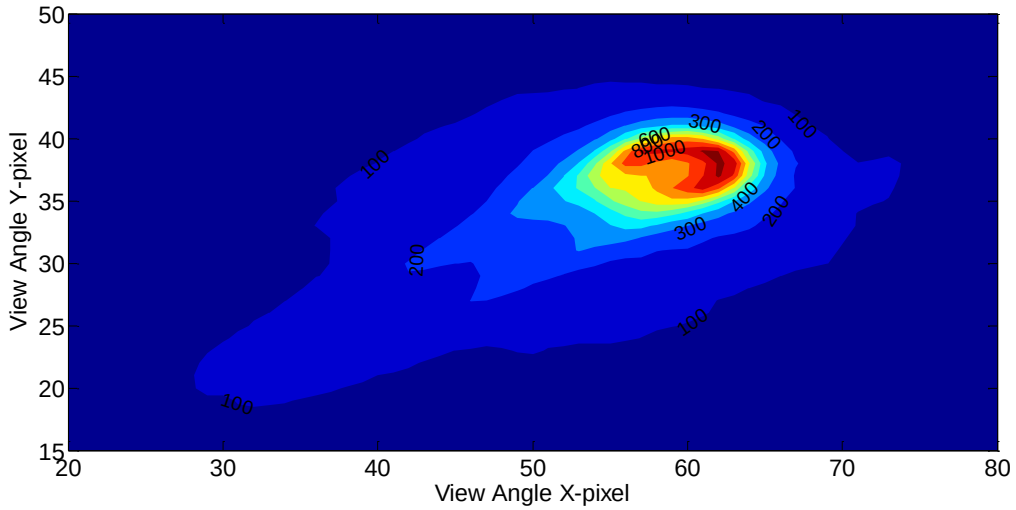

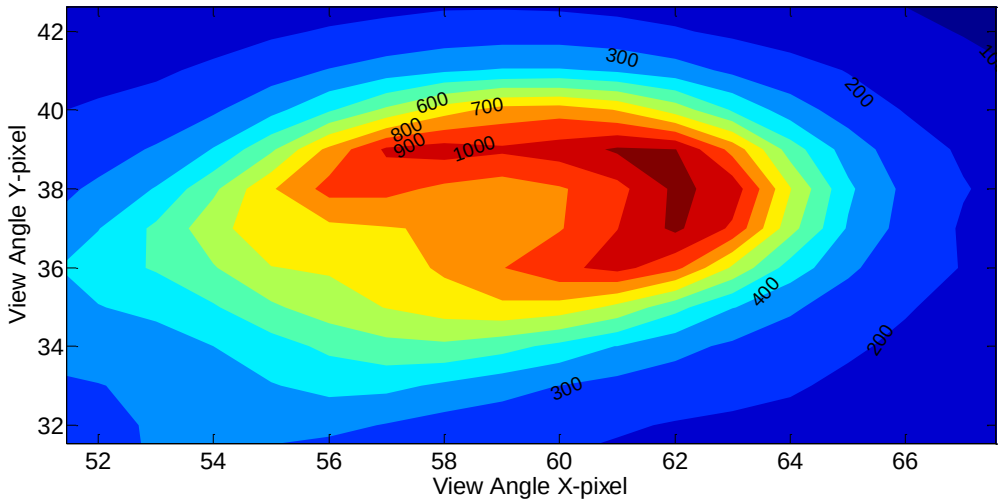

Figure 3-9 2D thermal of a clad line in X-Y coordinate system.

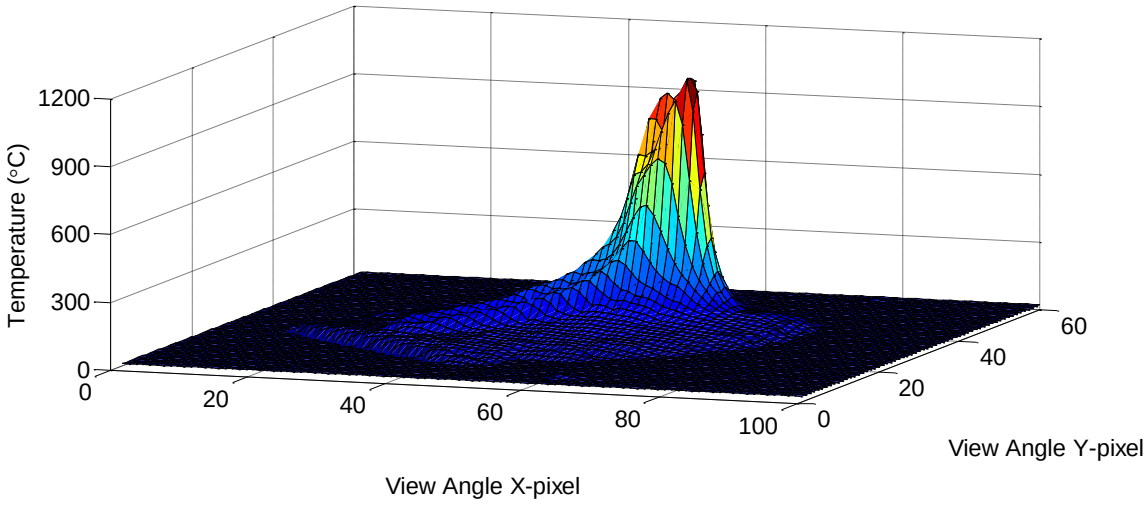

Figure 3-10 3D thermal map of a clad line.

3.5 Application of Thermal Feedback Control to LAM

Melt pool temperature, cooling rate and the thermal map are output process parameters which have to monitored and processed to obtain a desired microstructure during the LAM process. A controller is responsible for acquiring these data and interpreting the required control actions to create desired material properties such as microstructure. Since the output process parameters are measured and fed back to the controller in real time, a closed-loop feedback controller is required for the current system.

3.5.1 Closed-loop PID Control

Proportional-Integral-Derivative (PID) controllers are the most common control algorithms used in industry and have been widely accepted in manufacturing automation. Robustness and simplicity in functionality are the main reasons to the popularity of PID control. A PID controller calculates error values of the difference between a measured process output and a desired set point. The controller attempts to minimize the error by adjusting the process through use of a manipulated variable. The PID algorithm consists of three basic coefficients; proportional (P), integral (I) and derivative (D) which are varied to get optimal response.

A block diagram of a PID controller in a feedback loop is shown in Figure 3-11. The present error is represented by K_c (proportional gain), the accumulation of past errors is represented by T_i (integral gain), and prediction of future errors is represented by T_d (differential gain), as the error and its rate of change are computed at each step. The three actions are summed to adjust the microstructure using a process variable $u(t)$ such as the travel speed, laser power or beam diameter.

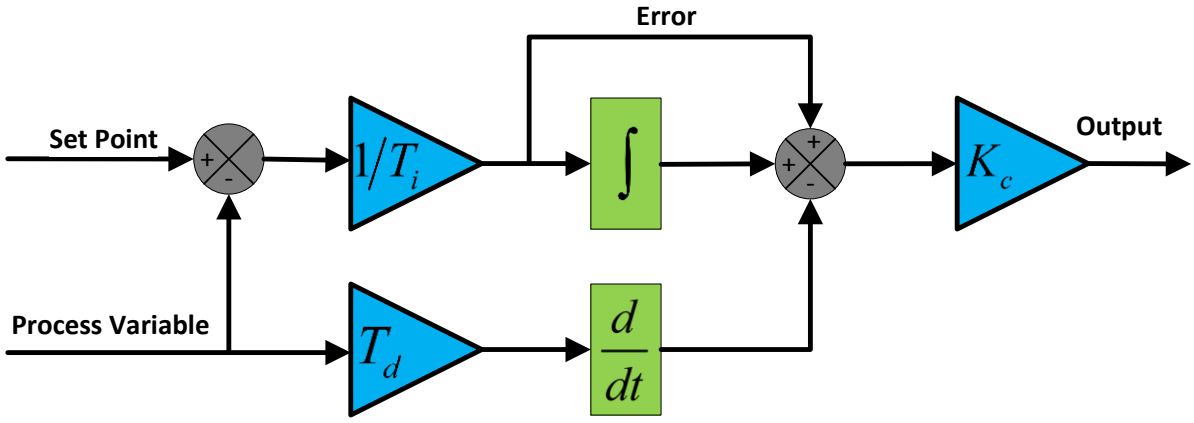

Figure 3-11 Block diagram of a basic PID control algorithm.[106].

In some cases, the response of the system to a given control output may change over time or in relation to some variable [106]. A nonlinear system is a system in which the control parameters that produce a desired response at one operating point might not produce a satisfactory response at another operating point [106]. The LAM process is also a very complex nonlinear system, which cannot be predicted or modeled with simple relations.

Thus, preliminary experiments are required to understand which of the process variables should be used as the control action. These experiments are carried out in the later sections (Section 4.4) to provide a good choice for the control action.

A schematic graph of the closed-loop thermal control of the LAM process developed and discussed in this chapter is illustrated in Figure 3-12. Figure 3-12 is a general summary of all the algorithms and processes developed in the experimental setup (Section 3.2), thermography setup (Section 3.4) and closed-loop PID control (Section 3.5) sections.

Figure 3-12 Schematic of the developed closed-loop thermal LAM process.

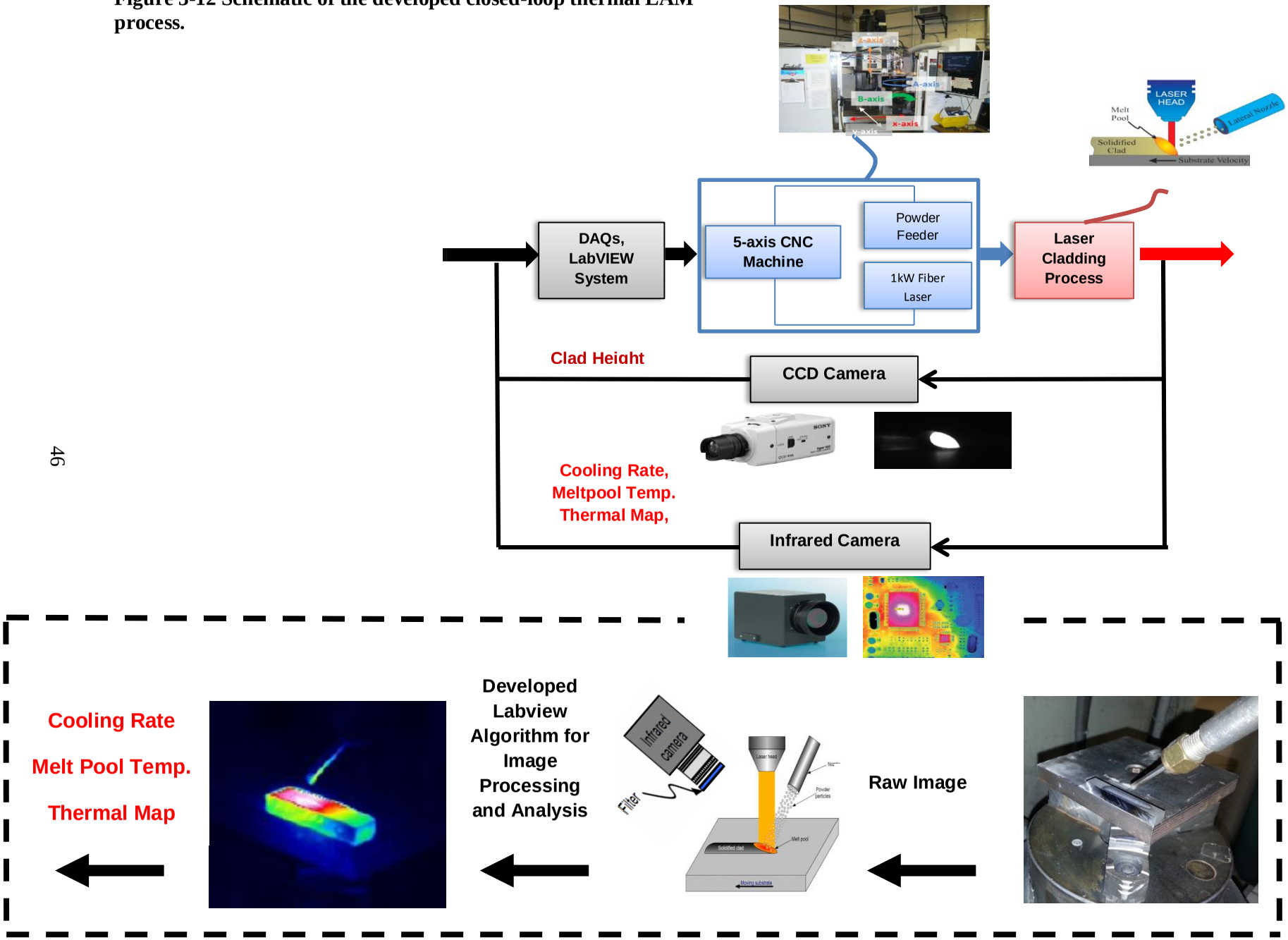

Chapter 4
Influence of Cooling Rate on Microstructural Evolution

This chapter addresses the effects of melt pool temperature and cooling rate on the formation of the clad microstructure during the Laser Additive Manufacturing (LAM) process. The chapter begins with studying the combined effects of melt pool temperature and cooling rate variations on the clad microstructure. Melt pool temperature and cooling rate effects are compared to evaluate the more influential parameter on clad morphology and microstructure. The chapter continues with further detailed analysis of cooling rate effects on the microstructure. Finally, the influence of travel speed on cooling rate and microstructure evolutions during the LAM process is discussed.

4.1 Experimental Methods

Stainless Steel (SS) 316L powder, -325 mesh, from Praxair Surface Technologies were used for deposition. The SS 316L powder had a composition of 0.003 wt % C, 17 wt % Cr, 65.5 wt % Fe, 1 wt % MN, 3 wt % Mo, 13 wt % Ni, less than 0.005 wt %, 0.01 wt % S and 0.45 wt % Si.

All experiments in this chapter conducted used AISI 1030 medium carbon steel substrates with a composition of: 0.28-0.34 wt % C, 0.6-0.9 wt % Mn, less than 0.04 wt % P, and less than 0.05 wt % S. The dimensions of the substrates were $100 \times 30 \times 6.35\ mm$. Before the LAM process the substrates were rinsed with ethanol and washed with acetone to remove any contamination. Each set of single-line claddings in Sections 4.2 and 4.3 were performed on separate substrates. Thus, the two group of experiments were performed on two substrates with each two clad lines having a distance of $10\ mm$ with each other. Initial temperature and amount of preheat in all single-line claddings have great influence in microstructure formation. To insure the initial temperature and preheat of each clad line was same, after the deposition of each line on the substrate, the substrate was water cooled for $10\ s$ and air dried to reach the initial room temperature.

The specimens were sectioned in the longitudinal direction for microstructural examination. Samples were prepared using SiC grit paper with grit mesh sizes from 240 to 1200, polished with $1\ \mu$ alumina powder and auto polished with $1\ \mu$ to $0.5\ \mu$ diamond paste. After each polishing step, the samples were placed in an ultrasonic machine to remove contamination and later air dried. Stainless steel samples were etched in Marble's reagent ($10\ g$ $CuSO_4$ in $50\ mL$ HCl and $50\ mL$ H_2O), to expose grain structure

and morphology. The microstructures were analyzed using optical microscopy with images obtained from an Olympus AH microscope with objective magnifications of up to $50\times$.

4.2 Combined Effect of Melt Pool Temperature and Cooling Rate on Clad Microstructure

The influence of melt pool temperature and cooling rate on microstructure and solidification behavior of metals has been an area of active research over the past few decades. Although there are several reports available in literature that consider the effects of these two parameters on the microstructure, no investigation has compared the effects of these two parameters on solidification behavior. Comparing the effects of melt pool temperature and cooling rate on the microstructure provides a good understanding of each parameter's characteristic and type of influence. More importantly, to develop a good controller for microstructure it is essential to determine the most important governing parameter on the microstructure between the melt pool temperature and cooling rate.

The amount of heat input during the LAM process defines the values of the melt pool temperature and cooling rate. A large variety of operating parameters and physical phenomena determine the amount of heat input. The main input parameters of the current LAM system can be categorized as the travel speed, laser power, laser beam diameter and powder feed rate. Since these parameters affect the heat input all at the same time, it is essential to use a combined parameter to address their combined influence. The effective energy per unit area E, and the powder deposition density PDD [1] are two widely used parameters in literature that can express combined influence of all the main input parameters.

The effective energy measures the amount of energy delivered to the process by the laser. This energy is principally responsible for melting the substrate surface and powder, and is defined by [1]:

$$E = \frac{P}{VD} \tag{4.1}$$

in which P is the laser power, V is the traveling speed of the substrate, and D is the laser beam diameter. The effective energy E is measured in units of $\frac{J}{mm^2}$.

The powder deposition density is also a good indicator of the amount of powder fed to a unit area of the substrate during deposition. The powder deposition density is defined by [1]:

$$PDD = \frac{R}{VD} \tag{4.2}$$

where R is the powder feed rate. The powder deposition density PDD is measured in units of $\frac{g}{mm^2}$.

The effective energy and powder deposition density are two parameters that describe the combined effects of the laser power, travel speed, laser beam diameter and powder feed rate on the amount of heat input during the LAM process. The amount of heat input defines values for the melt pool temperature and cooling rate. Thus, E and PDD are directly related to the melt pool temperature and its cooling rate, and indirectly related to the microstructure formation and its properties. However, there still exists the question of whether it is the melt pool temperature or the cooling rate which has a more vital role in the formation of clad microstructure?

In order to evaluate the effects of melt pool temperature and cooling rate on the microstructure, a set of experiments were held considering the effective energy E, and powder deposition density PDD. Emamian et al. [52] studied the effects of laser parameters on the formation of TiC morphology using the effective energy and powder deposition density. They observed great changes in the microstructure by variations in both combined parameters. These changes were interpreted and verified analytically considering the individual effect of each combined parameter. However, identical values of E and PDD can be reached with different laser parameters. Emamian et al. [52] realized that by keeping both combined parameters E and PDD constant and changing the laser processing parameters, different microstructures were resulted. Analyzing these evolutions is difficult, since the system's processing parameters are changing, whereas, the combined parameters are constant and indicate no change. Hence, by keeping the effective energy and powder deposition density constant at different laser parameter setups, the heat input to the system is changing. Clearly defining the role of heat input is rather difficult since the LAM process is complex and there are several physical processes involved. No firm conclusion can be made on the trend of microstructural evolution of these type of experiments unless the thermal behavior during each E and PDD combination is studied.

To explore any possible influence of the melt pool temperature or cooling rate on microstructure and morphology differences, a set of samples with identical effective energy and powder deposition density, but dissimilar process parameters were prepared. Laser processing parameters for samples $A1 - A5$ are listed in Table 4-1. In all the samples A1 through A5, the effective energy and powder deposition density are $E = 110\frac{J}{mm^2}$, $PDD = 0.008\frac{g}{min}$ respectively, and the beam diameter is $2.5\ mm$.

Table 4-1 Laser processing parameters of A samples with similar $E = 110\,\frac{J}{mm^2}$ and $PDD = 0.008\,\frac{g}{min}$ parameters.

Sample No.	Laser power (W)	Travel Speed (mm/min)	Powder Feed Rate (g/min)
$A1$	1031.25	225	4.5
$A2$	916.67	200	4.0
$A3$	802.08	175	3.5
$A4$	687.50	150	3.0
$A5$	572.92	125	2.5

To examine the microstructure and morphology of each sample in Table 4-1, optical micrographs were captured. Different magnifications ($10\times$ to $50\times$) were used to analyze the microstructure locally and generally on the clad cross section. It is essential to understand microstructural changes and their correlation with cooling rate and melt pool temperature variations.

The macroscopic structure of a deposition is of great importance since many mechanical and material properties depend on grain size and grain shape. Figure 4-1 illustrates a low magnification micrograph of the samples. The solidification microstructures of the SS 316L are complex and different as expected in a rapid solidification process. The macrostructures of each sample differentiate in different regions of each cross section. Thus, there is no constant morphology for any of the samples; however, there are similar microstructural trends in all the samples. Generally, columnar zones predominate the bottom of the claddings at the clad substrate interface. All other regions of the clad have a cellular structure. The size of the cellular grain boundaries decreases gradually from bottom to the top of the clad interface. This general macrostructure in the claddings is very similar to the macrostructures developed in castings. Therefore, microstructural trends in the LAM process can be explained based on similarities to casting structures and their properties.

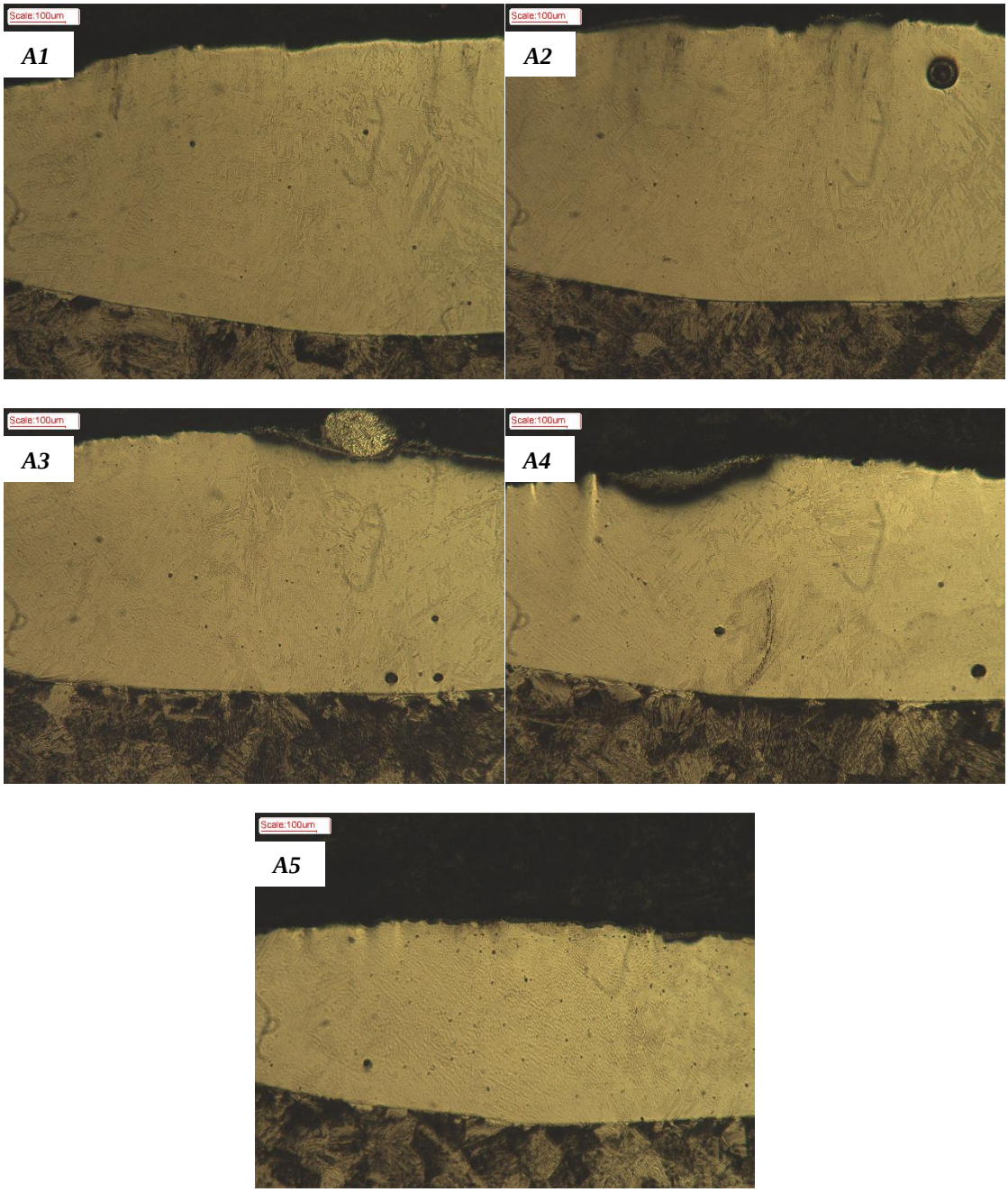

Figure 4-1 Low magnification $10\times$ micrographs of A samples with similar $E = 110\frac{J}{mm^2}$ and $PDD = 0.008\frac{g}{min}$ parameters.

The clad substrate interface is analogous to the mold walls in a cast structure. This interface provides nucleation sites for the columnar growth. The columnar shapes at the bottom of the cladding are due to

slow cooling rates that provide time for nucleation and growth of the nucleation sites. The axes of the columnar crystals are normally in the direction of heat flow [107]. The cellular zones in Figure 4-1 are also analogous to the equiaxed grains formed during castings. Two phenomena are responsible for production of these equiaxed grains [108]:

1) ***Grain multiplication:*** Grain multiplication is primarily caused by remelting of dendrites inside the columnar zone. Dendritic arms get coarsened and thus separated and carried into the supercooled liquid metal. Hence, a new crystal is formed without an added nucleation site.

2) ***Convection:*** The separated arms are carried away by convection. Moreover, convection dissipates superheat in the liquid metal, thus providing suitable growth locations for the dendritic arms. This dissipated heat is transferred to the interface between the columnar and cellular grains, accelerating the melting of dendrites. It has been shown that convection has a great influence on the grain size. Larger grain size and columnar zones are produced when convection is reduced.

Smaller grain size on top of the clad cross section can also be attributed to the increased convection on top of the melt pool due to the additional air flow. Consequently, convection has a vital role in forming the columnar and cellular zones. On the other hand, increasing convection results in increased cooling rates that is measureable by the IR camera. Thus, the cooling rate is proven to be effective on the microstructure in theory.

The melt pool temperature also has a great effect on the formation of the equiaxed grains. When the melt pool temperature is high, the separated dendrite arms melt and disappear. Hence, as the melt pool temperature increases, the tendency to form equiaxed grains should decrease. Generally, the equiaxed grains that form in high melt pool temperatures have an increased grain size [109]. Therefore, the melt pool temperature is also theoretically effective on the developed microstructure.

Although, microstructures of the different samples in Figure 4-1 have a similar trend in terms of transformation from columnar to cellular zones, they are greatly different in terms of grain size and volume percentage of each cellular and columnar zone. For example, the cellular grain size in $A5$ is much greater than $A4$. Furthermore, a greater volume percentage of samples $A1 - A3$ have a columnar zone compared to $A5$. Since the effective energy and powder deposition density of all samples are similar, none of the microstructural changes can be interpreted theoretically considering the combined values or laser processing parameters individually. As discussed above, cooling rate and melt pool

temperature are in great connection with microstructural evolutions inside the melt pool during the LAM process. Thus, in order to study the effects of cooling rate and melt pool temperature on microstructural variations in samples $A1 - A5$, the measured values of these output parameters need to be compared.

In Figure 4-2 and Figure 4-3, the measured cooling rates and melt pool temperatures of each sample are illustrated in real time. These output signals were captured using the developed algorithm in Section 3.4.

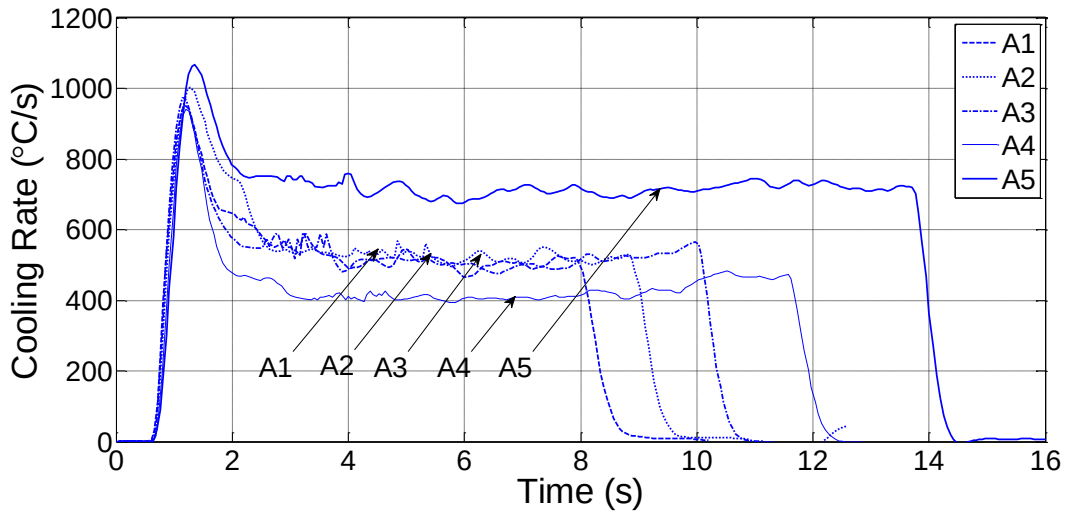

Figure 4-2 Real time cooling rate of A samples with similar $E = 110\frac{J}{mm^2}$ and $PDD = 0.008\frac{g}{min}$ parameters.

Since the cooling rate and melt pool temperature values are hard to compare graphically in Figure 4-2 and Figure 4-3, their values were averaged quantitatively over their steady state regions. The averaged values of the cooling rate and melt pool temperature for samples $A1 - A5$ are listed in Table 4-2.

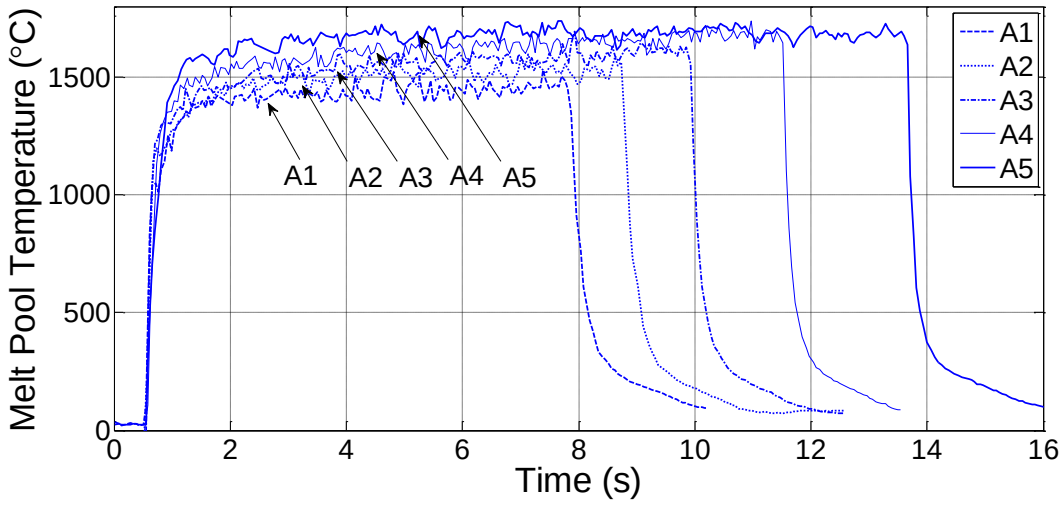

Figure 4-3 Real time melt pool temperature of A samples with similar $E = 110\,\frac{J}{mm^2}$ and $PDD = 0.008\,\frac{g}{min}$ parameters.

The effect of power and velocity on the amount of heat input can be interpreted by comparing the process parameters of the samples in Table 4-1 with the cooling rate and melt pool temperatures in Table 4-2. According to Table 4-1, the power, travelling speed and powder feed rate decrease gradually from $A1$ to $A5$. The decreasing power results in less heat input, whereas the decreasing traveling speed results in more concentrated energy and heat. Thus, the power and travelling speed act in opposite ways in changing the amount of heat during the LAM process.

Table 4-2 Average cooling rate and melt pool temperatures A samples with similar $E = 110\,\frac{J}{mm^2}$ and $PDD = 0.008\,\frac{g}{min}$ parameters.

Sample No.	Average Cooling Rate ($\frac{℃}{s}$)	Average Melt pool Temperature (℃)
$A1$	505	1440
$A2$	518	1510
$A3$	511	1576
$A4$	426	1621
$A5$	712	1683

In Table 4-1, the melt pool temperature increases from sample $A1$ to $A5$ that indicates an increase in the heat input as well. The increasing melt pool temperature can be attributed to the decreasing travelling speed, which increases the heat input. Hence, the traveling speed is found to be more influential on the heat input than the laser power. On the other hand, the cooling rate behaves in a nonlinear manner. Samples $A1 - A3$ have an equal value of cooling rate, whereas, samples $A4$ and $A5$ have different values. $A4$ has the lowest cooling rate and $A5$ has an unusual high cooling rate with $C_{A5} = 1683\ \frac{℃}{s}$. This irregular behavior of the cooling rate makes it difficult to correlate it with the combined influence of travel speed or laser power. It is noteworthy to point out that due the unusual behavior of the cooling rate and melt pool temperatures in Table 4-2, and also to study the repeatability of the measurements, each sample was deposited two times and similar results were observed.

It is necessary to correlate cooling rate and melt pool temperature variations with microstructural evolutions in the samples indicated in Table 4-1, to understand microstructural characteristics in the LAM process. In order to do so, higher magnification micrographs are required to compare grain size and grain shapes in more detail. High magnification micrographs ($50\times$) of each sample are shown in Figure 4-4. These micrographs have all been taken at a similar location at the center of the cladding for all the samples. Thus, microstructural variations in Figure 4-1 and Figure 4-4 should be compared to the data in Table 4-1 and Table 4-2 to find the relations between the processing parameters and the material properties.

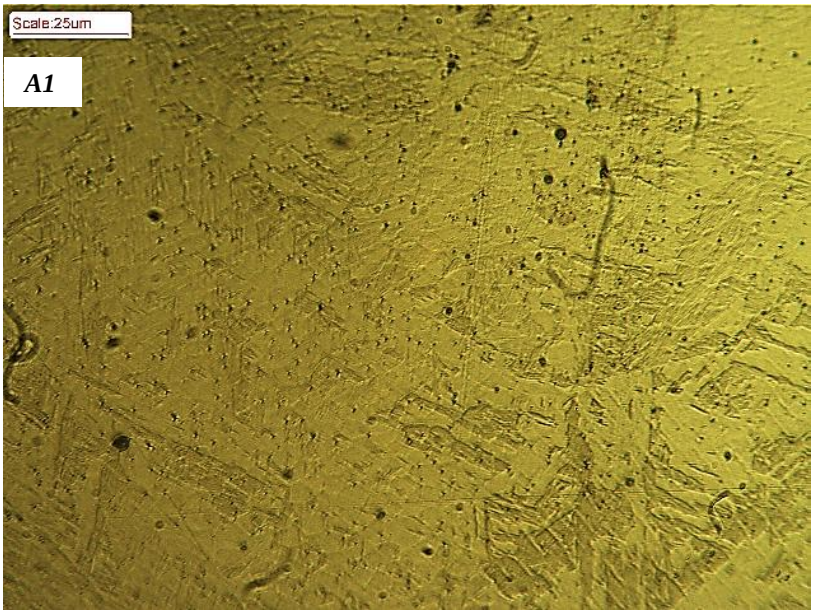
Scale:25um
A1

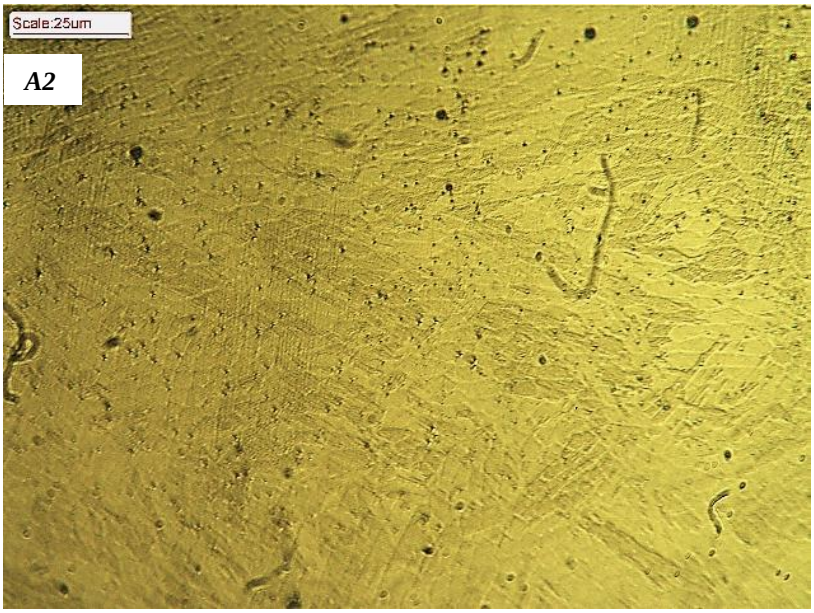
Scale:25um
A2

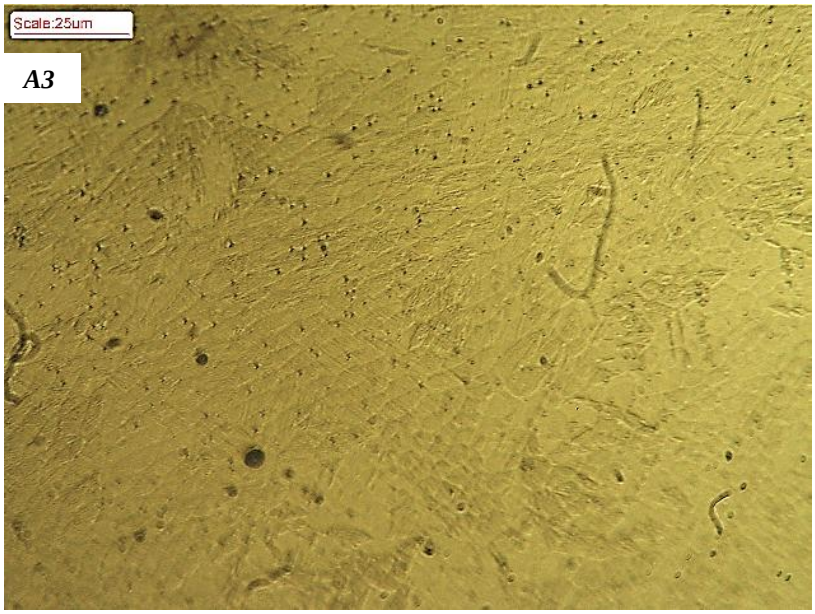
Scale:25um
A3

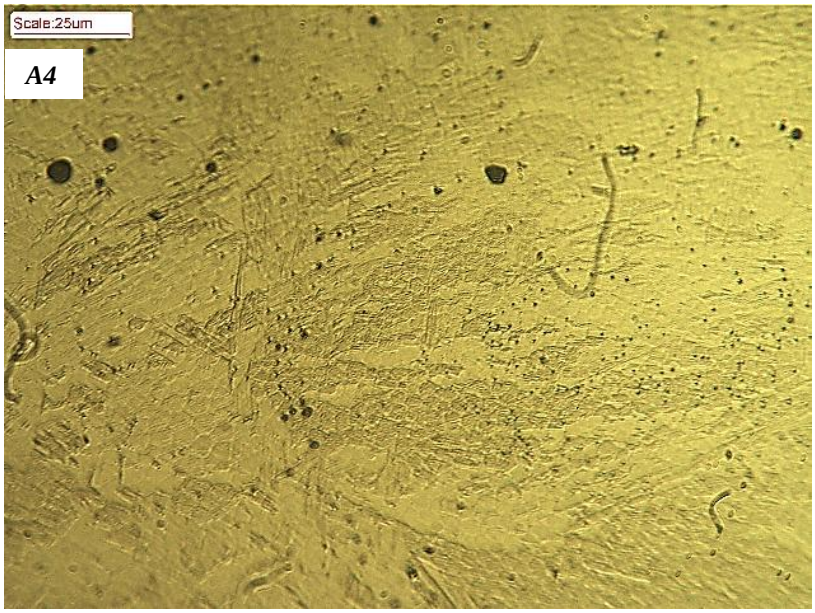
Scale:25um
A4

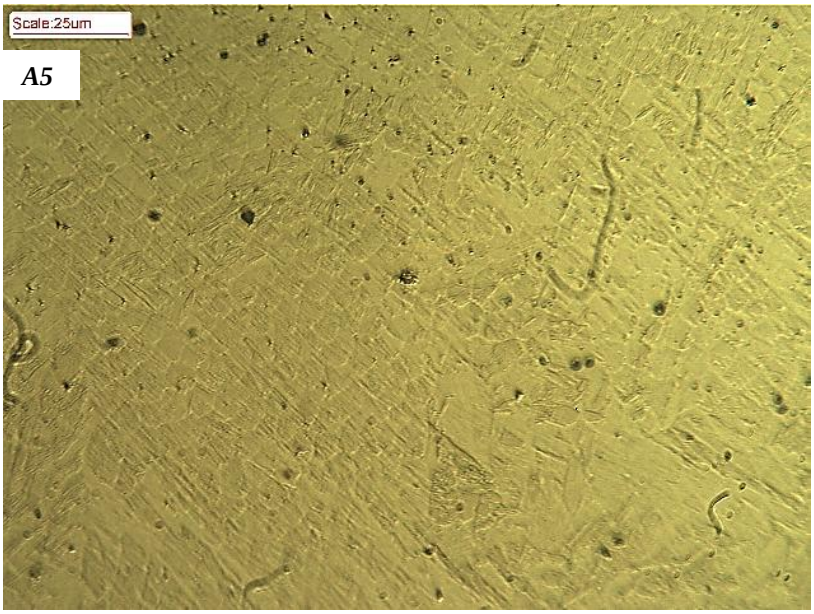

Figure 4-4 High magnification $50\times$ micrographs of samples A1 through A5 with similar values of $E = 110\frac{J}{mm^2}$ and $PDD = 0.008\frac{g}{min}$ parameters.

Samples $A1 - A3$ have very similar macrostructural (Figure 4-1) and microstructural (Figure 4-4) properties. Their macrostructures consist of an initial columnar zone at the clad substrate interface with a region of cellular zone in the center. Moreover, according to Figure 4-4, generally the size of these grains for samples $A1 - A3$ are also identical. As observed in Table 4-2 , these samples were solidified with equal cooling rates but different melt pool temperatures. The macrostructural consistency with the cooling rate indicates a strong relation between these two parameters. Compared to $A1 - A3$, sample $A4$ has a greater columnar region and less fraction of cellular grains. This change is due to the decreasing value of the cooling rate for $A4$ compared to $A1 - A3$. The lower cooling rate in $A4$ provides more time for the columnar grains to grow, making it difficult for the cellular grains to further nucleate and precipitate. In addition, the higher melt pool temperature in $A4$ further reduces the chances of the cellular crystals to survive in the melt pool. Thus, the lower cooling rate and higher melt pool temperature act in similar ways to reduce cellular growth and promote the columnar region appearing in sample $A4$. On the other hand, $A5$ has the largest cellular region amongst all the samples. This greater cellular region is caused by the high cooling rate value measured in $A5$. The increased cooling rate is a burden for dendrites to grow, thus, resulting in early coarsening and separation of their tips that form the equiaxed grains. In spite of the increased cellular region due to lower cooling rate, the equiaxed grains in $A5$ are much bigger in size compared to the ones in $A4$. Examining Table 4-2, it can be noted

that sample $A5$ has a higher melt pool temperature than $A4$. As stated earlier, it is harder for the cellular grains to grow in high melt pool temperatures since the smaller grains re-melt due to the high temperature of the melt pool. Thus, only the bigger cellular grains survived and grown in $A5$ due to a higher melt pool temperature. Moreover, since there are fewer columnar grains to limit the growth of the cellular region, the cellular grains grow rapidly and yield a larger size in $A5$.

4.2.1 Effect of Cooling Rate and Melt Pool Temperature on Dilution and Clad Height

Clad height and dilution of the A samples were measured to analyze the effect of cooling rate and melt pool temperature on these parameters. In this , h is the clad height, w is the clad width, θ is the angle of wetting, and b is the clad depth representing the thickness of substrate melted during the cladding and added to the clad region. The geometrical definition of dilution is defined as follows:

$$dilution = \frac{h}{h + b} \tag{4.3}$$

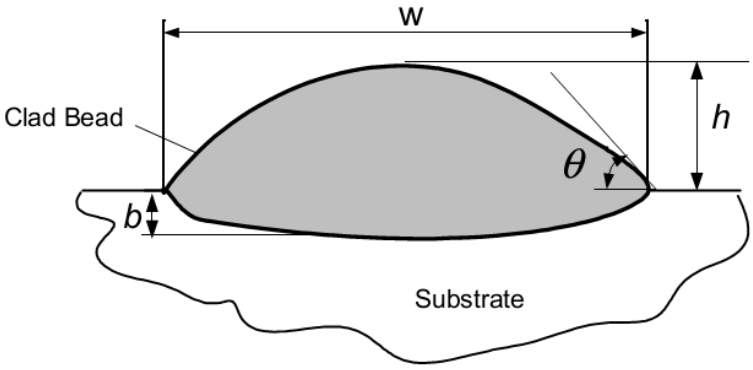

Figure 4-5 Clad cross section in LAM [1]**.**

In Table 4-3, clad height and dilution are calculated for the samples listed in Table 4-1. The clad height decreases from $A1$ to $A5$. This increase is in great correlation with the increasing melt pool temperature for these samples as listed in Table 4-2, whereas, it does not have any relation with the cooling rates of these samples. Thus, as the melt pool temperature increases, the clad height of the samples decrease.

On the contrary, the dilution does not have any specific trend from $A1$ to $A5$. However, by comparing the cooling rates (Table 4-2) with the dilution of each sample, it is observed that there is a positive correlation between the cooling rate and dilution. Sample $A5$, which has the highest dilution also has

the highest cooling rate. In addition, $A4$ has the lowest dilution because of its' low cooling rate. On the other hand, samples $A1, A2$ and $A3$, which have identical cooling rates, all have similar dilutions.

Table 4-3 Dilution and clad height of the A samples with similar $E = 110\frac{J}{mm^2}$ and $PDD = 0.008\frac{g}{min}$ parameters.

Sample	$A1$	$A2$	$A3$	$A4$	$A5$
Clad Height	81.02 μm	75.70 μm	65.74 μm	69.73 μm	36.64 μm
Dilution	48%	51%	52%	43%	63%

In order to better illustrate the correlation between the cooling rate and dilution of the A samples, dilution is plotted as a function of cooling rate in Figure 4-6. A pseudo-linear relation exists between the cooling rate and dilution.

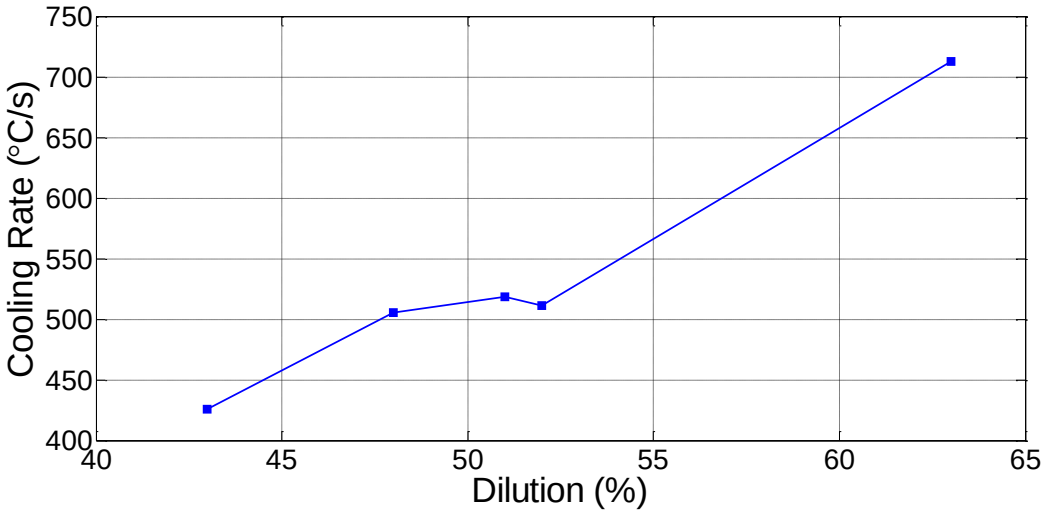

Figure 4-6 Clad dilution as a function of cooling rate.

In conclusion, the cooling rate and melt pool temperature variations are both effective in microstructural formations and evolutions in LAM; however, the cooling rate is proven to be more effective in the final microstructure. Changes in melt pool temperature do not necessarily change the microstructure unless the temperature reaches a sufficient critical value above the melting point. Furthermore, the melt pool temperature is mainly responsible for changing the status of the cellular

region in terms of growth and size. Further analysis showed a strong correlation between the microstructure and cooling rate. As the cooling rate increased, more equiaxed grains were formed, whereas, with the decreasing cooling rate a greater number of dendritic and columnar growth was promoted. It was proven that even small changes in the cooling rate as big as $90\frac{℃}{s}$ (for sample $A4$ compared to $A1-A3$) result in considerable changes in the microstructure, whereas there has to be larger variations in the melt pool temperature to observe changes in the microstructure. The cooling rate also influences the grain size boundary, both in the columnar and cellular regions.

4.3 Effect of Cooling Rate on Microstructure

According to results in the previous section, the cooling rate is more influential on the LAM microstructure compared to the melt pool temperature. Having defined the cooling rate as the most influential output parameter correlated with microstructural evolutions, it is necessary to study the sole effect of cooling rate on the clad microstructure. On the other hand, it was also observed that the travel speed had a greater influence on the cooling rate compared to the other two parameters (i.e. laser power and powder feed rate). Thus, a new set of experiments were conducted; changing the travel speed, while keeping the laser power and powder feed rate constant during single line claddings. The parameters of the B samples are shown in Table 4-4. As noted, the travelling speed of the laser increases gradually from sample $B1$ to $B4$, whereas the laser power and powder feed rate have constant values of $700\ W$ and 4.0 g/min, repectively.

Table 4-4 Laser processing parameters of B samples for studying the effects of cooling rate on microstructure, and effects of travelling speed on cooling rate.

Sample No.	Laser power (W)	Travel Speed (mm/min)	Powder Feed Rate (g/min)
$B1$	700	25	4.0
$B2$		50	
$B3$		100	
$B4$		200	

Cooling rate and melt pool temperatures of the *B* samples are presented in Figure 4-7 and Figure 4-8, respectively. It is apparent from these figures that as the speed increases the cooling rate increases dramatically, whereas the melt pool temperature decreases. Although, the cooling rate and melt pool temperature are both affected by the speed change, the changes in the cooling rate are more significant. A more detailed analysis of the speed effect on cooling rate variations will be presented in the next section.

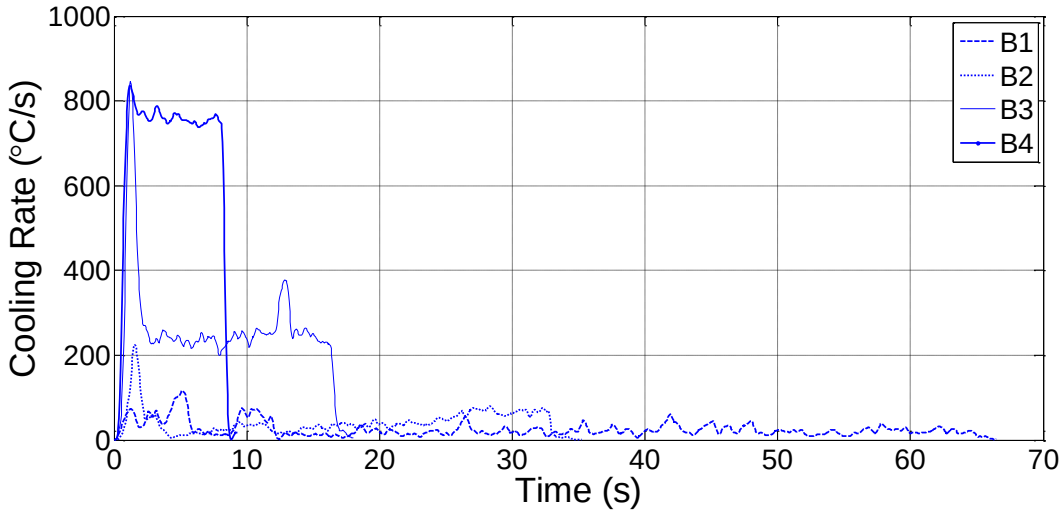

Figure 4-7 Cooling rate of *B* samples: $B1\ \left(v = 25\frac{mm}{min}\right)$, $B2\ \left(v = 50\frac{mm}{min}\right)$, $B3\ \left(v = 100\frac{mm}{min}\right)$ and $B4\ \left(v = 200\frac{mm}{min}\right)$.

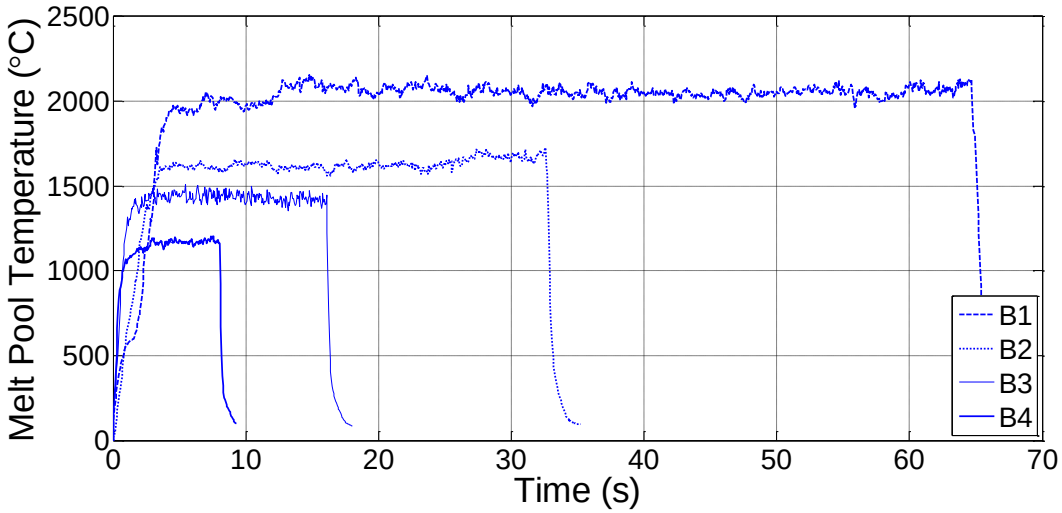

Figure 4-8 Melt pool temperature of B samples: $B1$ $\left(v = 25\frac{mm}{min}\right)$, $B2$ $\left(v = 50\frac{mm}{min}\right)$, $B3$ $\left(v = 100\frac{mm}{min}\right)$ and $B4$ $\left(v = 200\frac{mm}{min}\right)$.

In order to compare cooling rate and melt pool temperature variations in more detail, the average cooling rate and melt pool temperature values of the stable regions in each of the B samples are listed in Table 4-5. Figure 4-9 compares low magnification micrographs of the B samples. Sample $B1$ has a greater height compared to the other samples, hence, only top of the $B1$ clad is shown in Figure 4-9.

Table 4-5 Average cooling rate and melt pool temperatures B samples for studying cooling rate effects on microstructural evolutions.

Sample No.	Average Cooling Rate ($\frac{℃}{s}$)	Average Melt pool Temperature (℃)
$B1$	22	2053
$B2$	39	1630
$B3$	248	1434
$B4$	764	1153

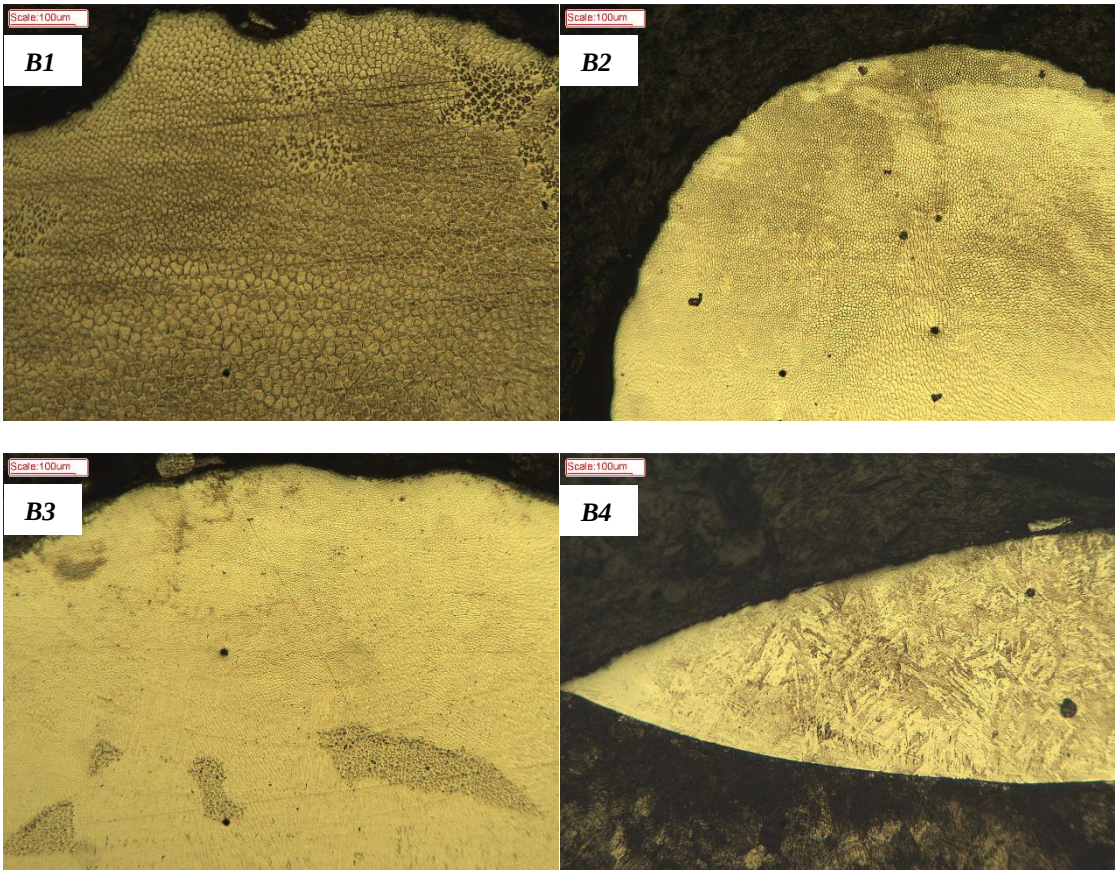

Figure 4-9 Low magnification micrographs of B samples.

As shown in Figure 2-6, SS 316L alloy line lies on the three-phase equilibrium triangle. As explained previously in Section 2.5.2, the solidification of the SS 316L undergoes the following transitions: $(L) \rightarrow (\gamma + L) \rightarrow (\gamma + \delta + L) \rightarrow (\gamma + \delta) \rightarrow (\gamma)$. Thus, the primary solidification occurs as austenite and since the line is located on the left side of the three-phase equilibrium triangle it shall remain austenitic upon cooling to room temperature. Microstructures of the SS 316L depositions in Figure 4-9 consist of two regions: (1) light regions, which represent the γ-austenite phase, and (2) dark regions, which represent the δ-ferrite phase. According to Table 4-5 and the micrographs shown in Figure 4-9, as the cooling rate decreases from $B1$ to $B3$ the ferrite content of the deposition decreases likewise. The increased cooling rate in $B3$ and to some extent in $B2$, reduces the chances of δ-ferrite formation. Since the $(\gamma + \delta + L)$ and $(\gamma + \delta)$ inter-phases are formed at very narrow temperature ranges, high cooling rates will reduce the total time of transitions in which δ-ferrite is formed. Thus, at high cooling rates less time is allocated for the formation of the δ-ferrite phase, resulting in a primary uniform austenite phase with cellular and dendritic austenitic substructures. Surprisingly, $B4$ has a higher content of

ferrite compared to $B2$ and $B3$, although having a much greater cooling rate. Moreover, compared to the cellular microstructure of samples $B1 - B3$, sample $B4$ has a needle-like microstructure. This type of microstructure and the very high cooling rate ($C = 764\ \frac{℃}{s}$) are signs of martensite production during solidification. To better understand whether sample $B4$ is martensite or not, micro hardness tests were taken from these samples. **Error! Reference source not found.** shows the micro hardness of the B samples, which were measured at similar locations on top of the clad cross sections. It is clear that $B4$ has a much greater hardness compared to the other three samples that is a proof of martensite presence in this sample. Since martensite has a higher hardness compared to austenite, the higher hardness in sample $B4$ indicates that the primary phase in this sample is martensite opposed to austenite in samples $B1 - B3$. Comparing cooling rates in these samples, apparently the rapid cooling rate in $B4$ is the cause of martensite production. Martensite is formed in stainless steels by the rapid cooling (quenching) of austenite at such high cooling rates ($C = 764\ \frac{℃}{s}$). Thus, the significance of cooling rate on the primary phase of solidification is once again proven.

Table 4-6 Micro hardness results of B samples.

Sample No.	Hardness (HV1000)	Average Cooling Rate ($\frac{℃}{s}$)
$B1$	150.5	22
$B2$	150.5	39
$B3$	153.3	248
$B4$	368.0	764

Very high cooling rate and dilution are the most likely cause of ferrite increase in $B4$. It was observed that samples $B1 - B3$ had nearly no dilution, whereas $B4$ had a certain amount of dilution. The differences in dilution can be interpreted by comparing the surface of clads $B3$ and $B4$ in Figure 4-9. It is apparent that $B3$ has a flat surface, which indicates no dilution, in contrast, $B4$ has a concave surface denoting a certain amount of laser beam penetration inside the substrate. The substrate is mild steel and consists mostly of ferrite. Therefore, dilution with carbon steel, partial melting and a very high cooling rate results in additional formation of ferrite content in $B4$. Furthermore, as it can be seen in Table 4-5, sample $B4$ has a melt pool temperature of $1153\ ℃$ that is much lower than the liquidus

temperature of SS 316L. Although, all phase transformations occur inside the γ-austenite region, the low melt pool temperature and high cooling rate prevents further nucleation and growth of the γ-austenite phase. Hence, dilution, low melt pool temperature and high cooling rate in sample $B4$ result in greater amount of the ferrite content as opposed to the general trend in $B1$-$B4$.

4.3.1 Grain Size Variation with Cooling Rate

Grain size variations are also observed in Figure 4-9, apart from changes in the ferrite content of the B samples. Grain boundary sizes decrease sharply from $B1$ to $B4$. To better illustrate these variations in the microstructure, a higher magnification micrograph of the B samples are presented in Figure 4-10. There is significant correlation between the grain size and process cooling rate. According to Figure 4-9 and Figure 4-10, with successive increase of the cooling rate, grain boundaries shrink dramatically. Consequently, $B1$, which has the lowest cooling rate, yields the largest grain size, and $B4$, which has the highest cooling rate, has very small grain substructures.

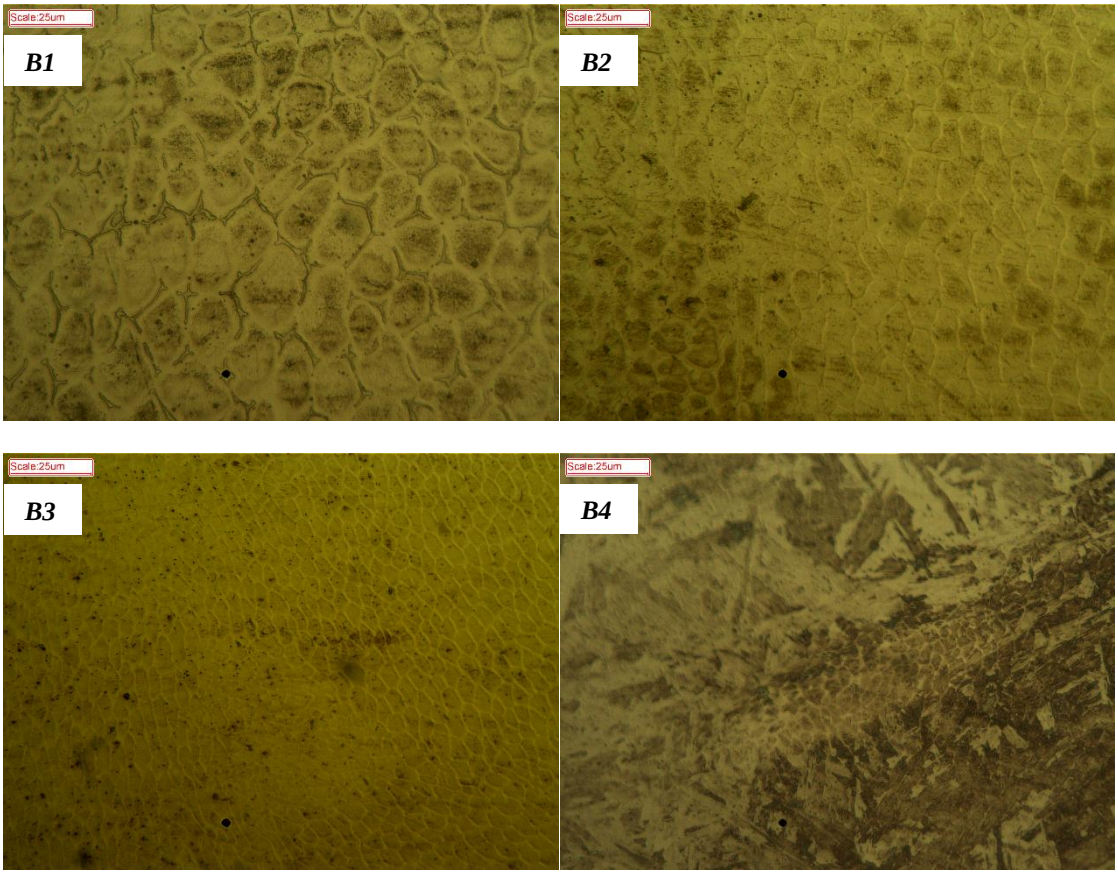

Figure 4-10 High magnification micrographs of *B* samples.

The Heyn [110] lineal intercept procedure was used to obtain the ASTM grain size of samples $B1 - B3$. In this procedure three concentric circles were sketched on a random location of each sample and the number of grain boundary intersections with the circles, P, were counted. By dividing P with the actual length of the circles, L, the number of grain boundary intersections per unit length of the test line, P_L, is obtained. The mean lineal intercept length, l, is obtained as follows:

$$l = \frac{1}{P_L} \tag{4.4}$$

which has a unit of mm. Finally, the ASTM grain size number, G, is derived by the following:

$$G = (-6.643856 \log l) - 3.288. \tag{4.5}$$

The ASTM grain size number of each B sample is listed in **Error! Reference source not found.**. The subsequent grains per unit area (N_A) and average grain diameter ($\bar{d}$) of each grain size number were also obtained using the tables provided in ASTM standard E 112.

Table 4-7 Grain size number of the B samples with changing speed.

Sample No.	G-ASTM Grain Size ($No.$)	N_A-Grains/Unit Area ($\frac{No.}{mm^2}$ at $1\times$)	$\bar{d}$-Average Grain Diameter (μm)
$B1$	9	3968.0	15.9
$B2$	10	7936.0	11.2
$B3$	12	31744.1	5.6

The grains per unit area and average grain diameter are sketched as a function of the sample's cooling rate in Figure 4-11 and Figure 4-12, respectively. The results show that the number of grains per unit increases with the cooling rate having a pseudo-linear relationship. On the other hand, the grain diameter decrease with the increasing cooling rate in a nonlinear manner. However, more measurements at different cooling rates are required to establish the generality of these relations between the cooling rate and the grain size.

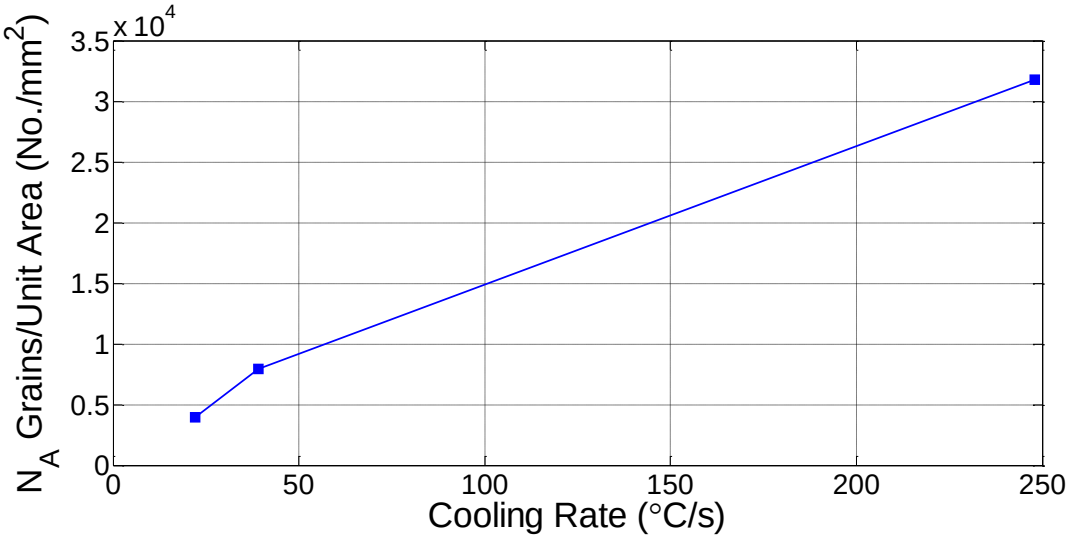

Figure 4-11 Variation of grains per unit area with respect to cooling rate for samples $B1 - B3$.

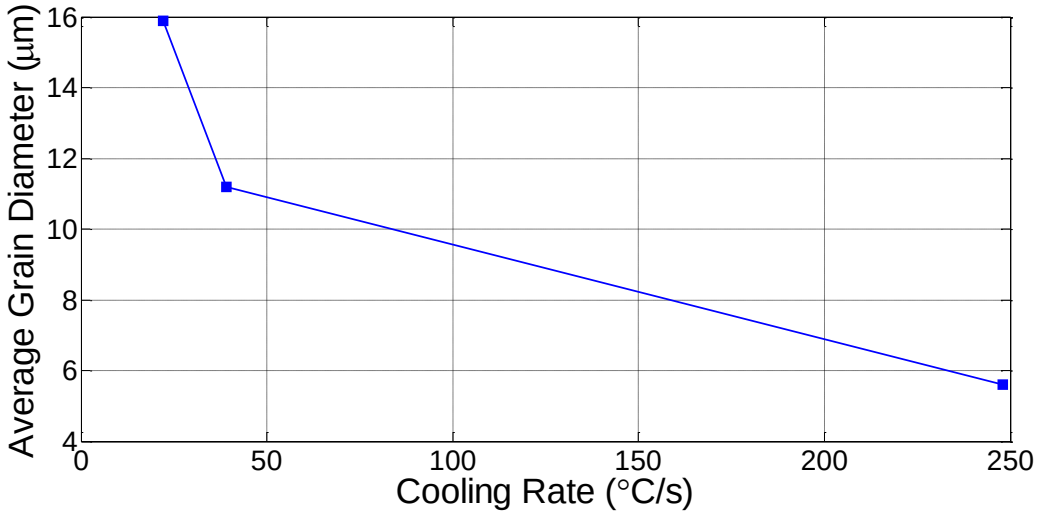

Figure 4-12 Variation of average grain diameter with respect to cooling rate for samples $B1 - B3$.

Surprisingly, an intercellular ferrite content is observed for sample $B1$ in Figure 4-10, which is not seen in other samples. This form of intercellular ferrite is the result of the very slow cooling rates in $B1$ that enables enough time for the ferrite to nucleate and grow at the cell grain boundaries. Further analysis of $B1$ even shows dendritic ferrite content at some locations of the clad, which is illustrated in

Figure 4-13. The dendritic growth of the ferrite content is another consequence of the low cooling rate in this sample.

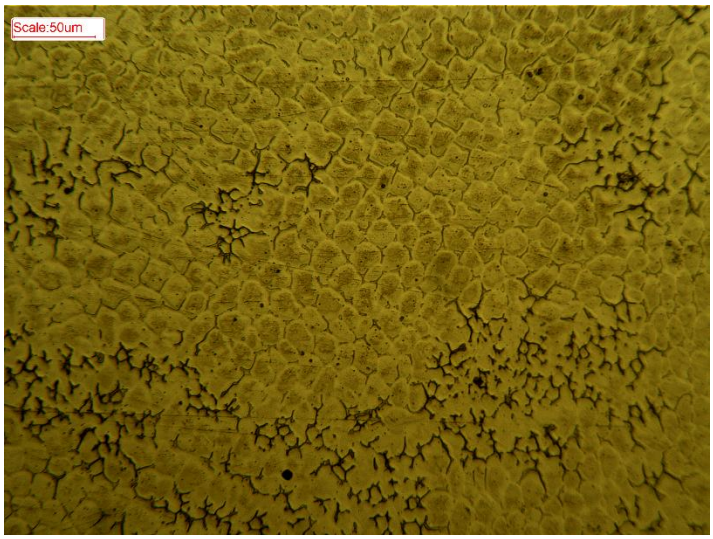

Figure 4-13 Dendritic ferrite content is sample $B1$ as a result of low cooling rate.

Overall, the results indicate a great correlation between the real time cooling rate and microstructural evolutions during the LAM process. The cooling rate has direct effect on: (1) the volumetric percentage of each phase inside the microstructure, (2) formation and growth of different phases, and (3) grain boundaries and grain size. Lower δ-ferrite content was yield at higher cooling rates. At very low cooling rates, new regions of intercellular and dendritic ferrite content were produced. Moreover, at low cooling rates, since more time existed for the nucleation and growth of the γ-austenite content, larger grains were obtained. It is noteworthy to point out the influence of the melt pool temperature and dilution on the microstructure as well. These two parameters mainly affected the volumetric content of the δ-ferrite phase and did not have great contribution in other microstructural evolutions.

4.4 Cooling Rate and Microstructure Variations with Travelling Speed

It was realized that cooling rate variations resulted in microstructural evolutions, however, the source of these variations and the effects of speed on the cooling rate were not discussed. Since the final aim of this research is to develop a microstructural controller, a physical controlling action (process variable) is required to address the microstructural evolutions as stated in Section 3.5. Although, the cooling rate, melt pool temperature and dilution were identified as the sources of microstructural

evolutions, these are only monitored output parameters that cannot be controlled directly. Thus, a control action, which is physically adjustable and has direct effect on the cooling rate is required.

It is quite revealing to combine the input and output data of the LAM process in Table 4-4 and Table 4-5. The speed is the only changing input process parameter in $B1 - B4$, having a constant laser power and powder feed rate. The cooling rate and melt pool temperature are graphically sketched as a function of the traveling speed in Figure 4-14 and Figure 4-15, respectively.

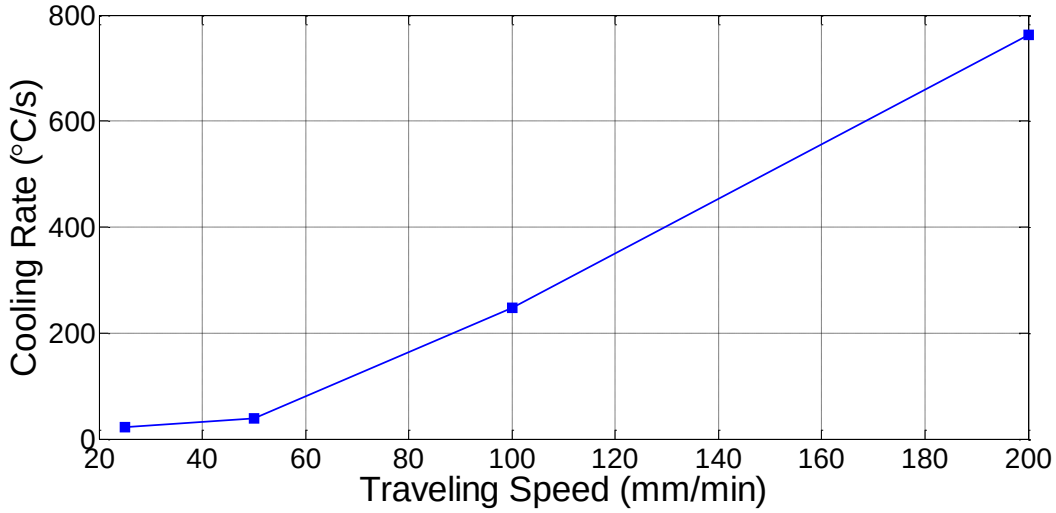

Figure 4-14 Effect of traveling speed on cooling rate.

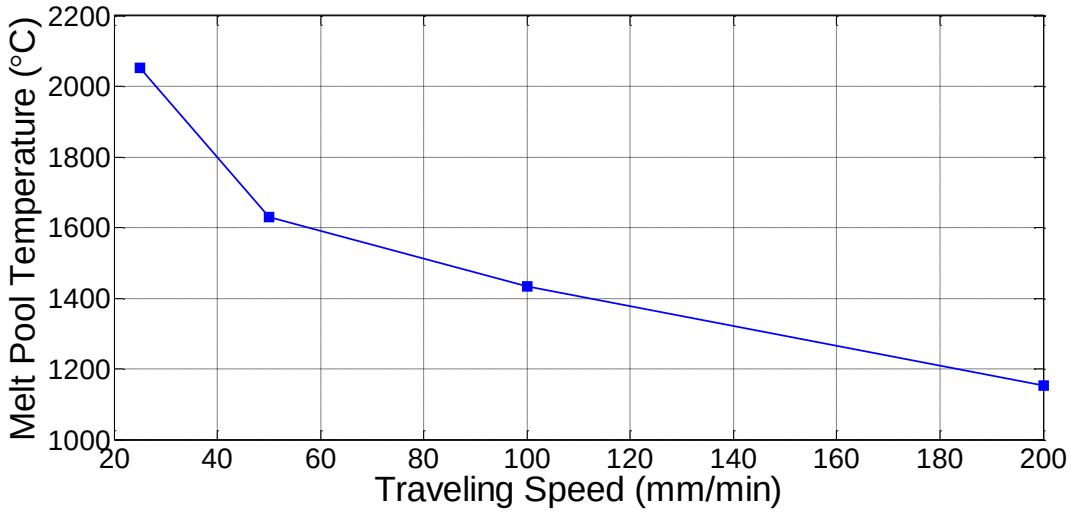

Figure 4-15 Effect of traveling speed on melt pool temperature.

The increasing speed has created an increasing trend for cooling rate and a decreasing trend for the melt pool temperature. Apparently, the traveling speed has a linear relation with the cooling rate and melt pool temperature, if the data from the $B1$ sample were to be neglected. In Figure 4-14, the cooling rate is nearly doubled by doubling the traveling speed. The traveling speed directly affects the cooling rate and hence indirectly affects the clad microstructure. Taken together, these results suggest that there is a positive association between real time cooling rate and microstructural changes, and the traveling speed. Thus, the traveling speed is a suitable physical parameter to be chosen as the controlling action for a microstructure controller in the LAM process.

The study in this chapter has shown that both cooling rate and melt pool temperature have direct effect on the clad microstructure during the LAM process. However, further analysis revealed that the cooling rate was more influential on the final macrostructure and microstructure. Effects of the cooling rate were also studied on the clad microstructure by changing the travelling speed. Microstructural analysis proved that the volumetric percentage of each phase inside the microstructure, formation and growth of different phases, grain boundaries and grain size were directly related to the real time cooling rate measured by the developed thermographic algorithm. Quantitative analysis of the grain size also revealed that the number of grains per unit area increased pseudo-linearly with increasing cooling rate, whereas, the average grain diameter decreased with the increasing cooling rate.

While, the cooling rate was identified as the most important process parameter effective on microstructure, a physical process variable was required to control the cooling rate in real time. Thus, experiments were held to understand the effect of different processing parameters (travelling speed, laser power and powder feed rate) on the cooling rate. Great correlation was observed between the traveling speed and real time cooling rate. Hence, the traveling speed of the cladding was identified as a suitable choice for the control action during microstructural control of the LAM process.

Chapter 5
Real Time Microstructure Control and Results

This chapter addresses the design and implementation of a closed-loop PID controller for controlling the microstructure in LAM. The traveling speed is used as the control action to control the cooling rate and thus, the deposition microstructure. The chapter begins with explaining the experimental procedures. It continues with tuning and implementing a controller for single line claddings with a constant desired cooling rate. The designed controller is then implemented in controlling multiple clad lines deposited consecutively on a substrate with each line having a staircase desired cooling rate and microstructure. Finally, applications of the microstructure controller in the industry are presented and evaluated.

5.1 Experimental Setup

Stainless Steel (SS) 303L powder, -325 mesh, from Alfa Aeser Co. was deposited during the LAM process carried out in this chapter. The SS 303L powder had a composition of 17 wt % Cr, 70 wt % Fe and13 wt % Ni. The current SS 303L powder differs from the SS 316L powder used in Chapter 4; which is to show the generality of the proposed controller and study. The SS 303L and SS 316L have a the same crystalline (austenitic FCC) structure and similar compositions, thus, the microstructural study carried out in Chapter 4 can be used in this chapter as well.

All other experimental and sample preparation conditions in this chapter are similar to the ones described in Section 4.1.

5.2 Microstructure Control in Single-line Cladding

The results, as shown in Section 4.3, indicate that the cooling rate has a significant effect on the microstructure during the LAM process. Thus, in order to develop a fully automated LAM process capable to produce desired mechanical and material properties, it is required to have a closed-loop controlled cooling rate during the process. Difficulties arise, however, when a controller is to be implemented experimentally to control the cooling rate, since there are several process parameters that effect the cooling process. Results in Section 4.4 showed, however, the travelling speed has a more critical role in defining the cooling rate value. Hence, to simplify the problem, the travelling speed was used as the sole controlling action to stabilize the cooling rate to a desired value. A PID controller was

designed and developed according to the algorithm discussed in Section 3.5.1. The controller was initially tested on single-line claddings deposited separately with a constant desired cooling rate.

5.2.1 Cooling Rate Control using a Closed-loop PID Controller

The developed closed-loop control system measures the cooling rate in real time and feeds it to the controller. The PID controller receives the real time and setpoint cooling rates as inputs to the system. The output of the controller is the required traveling speed to reach the desired cooling rate based on the current measurement and the PID gains. A PID controller has three adjustable integral (K_I), proportional (K_P) and derivative (K_D) gains, which have to be tuned manually or automatically.

Two cooling rate values $C_1 = 750\ \frac{℃}{s}$ and $C_2 = 210\ \frac{℃}{s}$ were chosen as the two initial setpoints for the controller to work on. The two values are chosen so that the controller is evaluated both at high ($750\ \frac{℃}{s}$) and low ($210\frac{℃}{s}$) cooling rate regions. The first step in implementing a PID controller is to tune the K_I, K_P and K_D gains on each of the desired setpoints.

Several closed-loop single-line claddings were deposited, having setpoint cooling rate values of $750\ \frac{℃}{s}$ and $210\ \frac{℃}{s}$. During these experiments, the laser power and powder feed rate were fixed to $P = 700\ W$ and $F = 4\ g/min$, respectively. During the depositions, several automatic tuning methods were tested; however, none produced the desired response. Thus, the gains were tuned manually for each setpoint. Further experiments showed that at each desired cooling rate, a different set of PID gains were required. Table 5-1 provides the optimal PID gains for the two setpoints; $C_1 = 750\ \frac{℃}{s}$ and $C_2 = 210\ \frac{℃}{s}$. It is apparent from Table 5-1 that no K_D gain is required for the controller, indicating the requirement of a PI controller for the process.

Table 5-1 Tuned PID gains for single-line cladding.

Setpoint Cooling Rate	$\boldsymbol{K_c}$	$\boldsymbol{T_I}$	$\boldsymbol{T_D}$
$\boldsymbol{C_1}$ $(\boldsymbol{750\ \frac{℃}{s}})$	2.5	0.001	0
$\boldsymbol{C_2}$ $(\boldsymbol{210\ \frac{℃}{s}})$	4	0.002	0

The developed controller was able to produce desired values of the cooling rates with great accuracy. More than ten sample clad lines were deposited by the automated system for each desired cooling rate; $C_1 = 750\ \frac{℃}{s}$ and $C_2 = 210\ \frac{℃}{s}$. In Figure 5-1 and Figure 5-2, real time values of two closed-loop single-line claddings are shown. Sample $C1$ in Figure 5-1 has a setpoint of $C_1 = 750\ \frac{℃}{s}$ and sample $C2$ in Figure 5-2 has a set point of $C_2 = 210\ \frac{℃}{s}$. As it can be seen, the controller rapidly stabilizes both setpoint values with a low error of 0.93 % for $C_1 = 750\ \frac{℃}{s}$ and 9.52 % for $C_2 = 210\ \frac{℃}{s}$. The settling time for sample $C1$ is close to $4\ s$, and for $C2$ it is $6\ s$. There are overshoots at the beginning of the cooling rate signals, which is attributed to the nature of the real time cooling rate measurement system. As stated earlier in Section 3.4.2, since the calculation of the cooling rate requires some time to be given for a decrease in temperature of a point after 15 sample times ($0.9375\ s$), the system requires $0.9375\ s$ to measure the first cooling point. Thus, as it is observed in both Figure 5-1 and Figure 5-2, after nearly $0.9375\ s$ the overshoot is damped since the system measurements of the cooling are correct, whereas, before this time the system measurements are unreliable and incorrect. Moreover, the initial oscillations and slow convergence of the system is attributed to the absence of a T_D gain. Unfortunately, after a T_D gain was inserted into the system, although, convergence was faster, the system became unstable. Thus, there below results are the best results obtained by a PID controller. However, there can be improvements in the results if advanced controlling techniques are introduced.

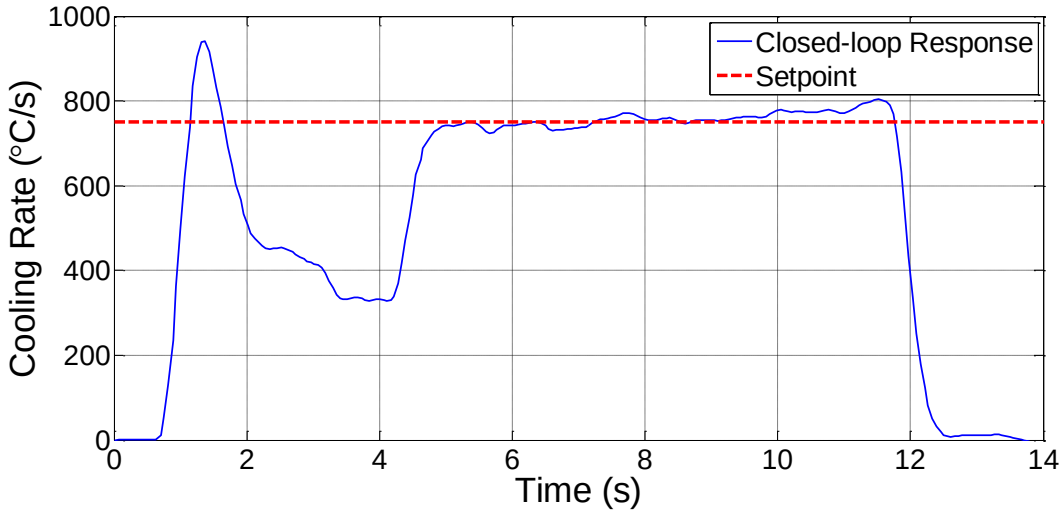

Figure 5-1 Closed-loop response of the cooling rate for sample $C1$ (single-line cladding with $750\ \frac{℃}{s}$ setpoint).

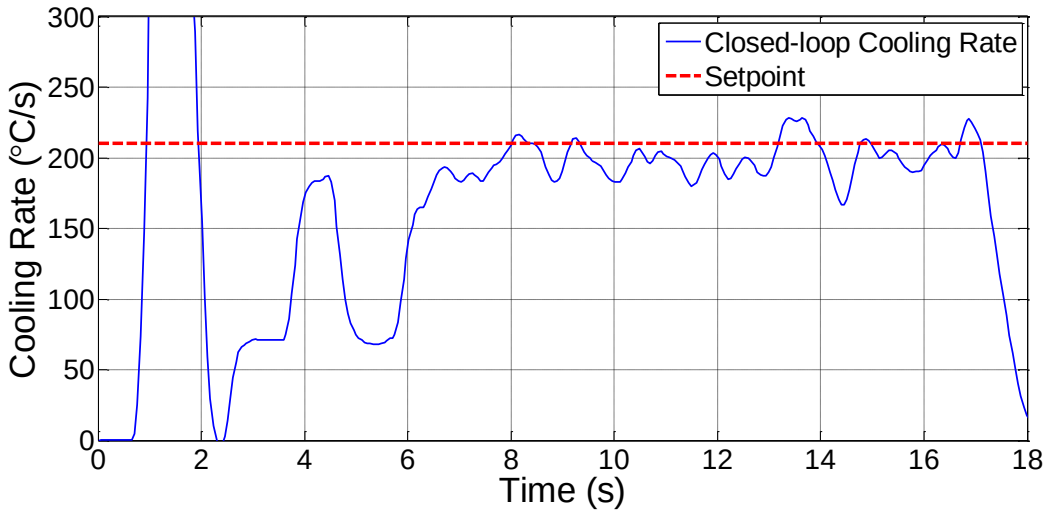

Figure 5-2 Closed-loop response of the cooling rate for sample $C1$ (single-line cladding with $210\ \frac{℃}{s}$ setpoint).

The real time closed-loop traveling speeds of the two samples $C1$ and $C2$ are shown in Figure 5-3. It can be seen that compared to $C1$, sample $C2$ has a lower speed, which is due to the lower cooling rate setpoint in $C2$. Therefore, the controller's response is logically correct considering the analysis provided in Section 4.4. Interestingly, the speed in sample $C2$ gradually increases in the stable region. This gradual increase is caused by the storage of heat in the substrate. As the clad is being deposited, residual energy not attracted by the melting material is stored in the substrate. This residual energy produces some preheat in the substrate and this amount of preheat is increased as time passes by and more material is deposited. Thus, less energy is required for reaching the desired cooling rate, which means a faster speed. Hence, the controller is adaptable to variations in the initial conditions as well. However, the increasing speed effect in the stable region is not observed for sample $C1$. Since the stable speed is higher for $C1$, the total time of laser shooting on the substrate is less for this sample. Consequently, less energy and preheat is transferred to $C1$. Therefore, the amount of preheat in $C1$ is not significant enough to have an effect on the cooling rate and the closed-loop traveling speed.

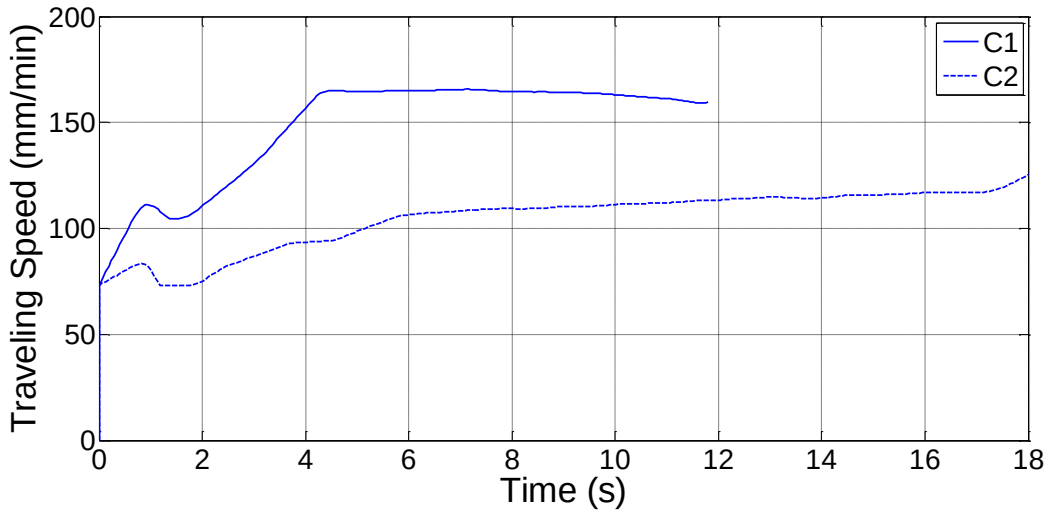

Figure 5-3 Closed-loop traveling speeds of samples $C1$ ($750\ \frac{℃}{s}$) and $C2$ ($210\ \frac{℃}{s}$).

The melt pool temperature of samples $C1$ and $C2$ are illustrated in Figure 5-4. The most striking result to emerge from the data is that the melt pool temperatures of the two samples are equal, which confirms the greater influence of the traveling speed on cooling rate compared to the melt pool temperature.

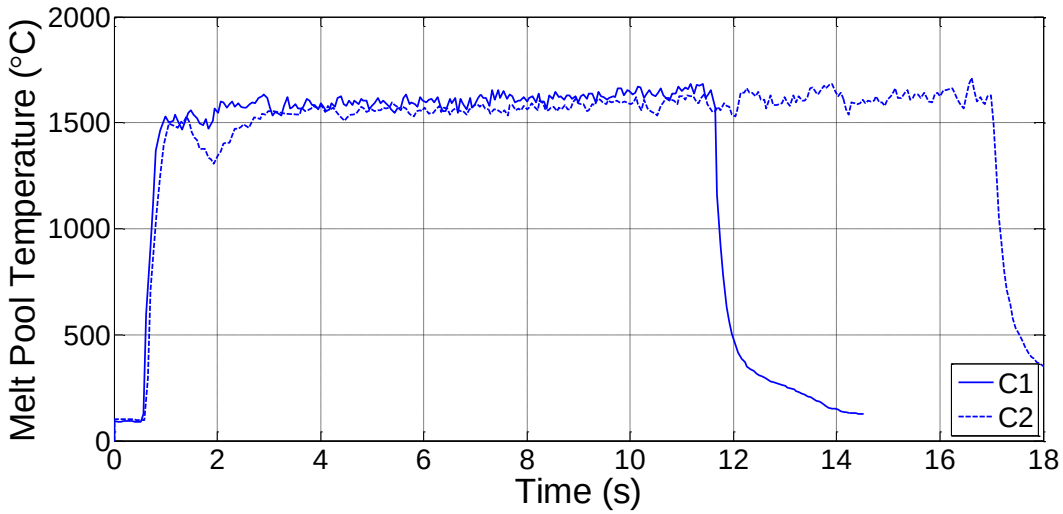

Figure 5-4 Closed-loop response of the melt pool temperature for samples $C1$ ($750\ \frac{℃}{s}$) and $C2$ ($210\ \frac{℃}{s}$).

Comparing Figure 5-1 with Figure 5-2, it is evident that the response of the PID is more stable in $C1$, which has a higher cooling rate. The oscillations observed in Figure 5-2 for $C2$ can be attributed to the low resolution of the IR-camera at low speeds. As the cooling rate decreases, the traveling speed of the substrate decreases likewise. This decrease in speed means that the tracking point P_t (refer to Section 3.4.2), will have a smaller distance with the melt pool pixel P_m (see Figure 3-6). Since there are very few pixels between P_t and P_m, the chance of error and noise increase in calculation of the real time cooling rate. However, $C2$ is shown to have a very stable closed-loop speed in Figure 5-3, which is an indication of a stable cooling rate and melt pool temperature, as shown in Figure 5-4. Thus, the oscillations observed at low cooling rates in Figure 5-2 are mainly measurement noise due to low resolution of the IR camera, and it can be confirmed that the cooling rate is stable since these noises are only around the setpoint. Moreover, in samples $C1$ and $C2$, although, the cooling rate was controlled throughout deposition, some inconsistency was observed in the clad geometry (clad height). This inconsistency in the geometry arises while the laser power during deposition is constant.

In conclusion, preliminary results reveal that the cooling rate can be controlled during the LAM process by a closed-loop PID controller. While, the cooling rate of the two samples $C1$ and $C2$ differed greatly in the closed-loop process, their melt pool temperatures were found to be similar. However, there is still no evidence of whether the microstructure has been controlled or not. To evaluate microstructure consistency obtained by the controller, micrographs from different points on the clad line have to be compared.

5.2.2 Microstructure Control and Results

The main aim of this research is to produce a desired controlled microstructure during the LAM process. The proposed closed-loop control process in Section 5.2.1 was successful in controlling the cooling rate for single-line claddings. Results in Section 4.3 suggest that a controlled cooling rate during the process should yield a controlled microstructure as well. Although, the melt pool temperature also influences the final microstructure, it is the real time cooling rate of the process that governs the general microstructure of the deposition. Hence, to investigate the performance of the closed-loop controller on microstructural evolutions, samples $C1$ and $C2$ were each sectioned at two different locations along the cladding line.

Figure 5-5 presents micrographs of the two cross sections in sample $C1$, which has a high cooling rate of $C_1 = 750\ \frac{℃}{s}$. It is apparent from these micrographs that both cross sections have a similar

microstructure in terms of grain size and cellular growth. Both microstructures consist of cellular and columnar grains. Surprisingly, the volumetric percentage of the columnar and cellular regions and their grain sizes are also exactly the same for both cross sections in Figure 5-5. The volumetric percentage of the γ-austenite and δ-ferrite are also observed to be qualitatively equal, comparing the light and dark regions of the two micrographs.

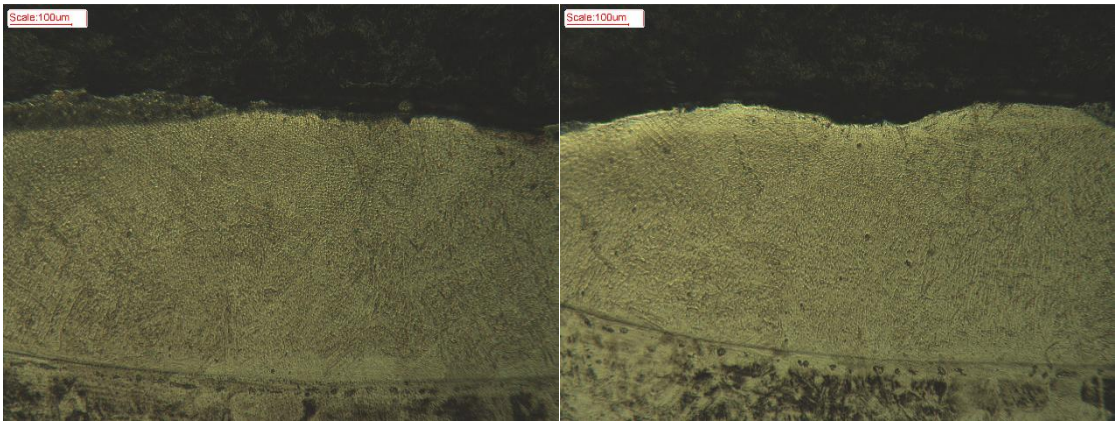

Figure 5-5 Micrographs from two different locations in sample $C1$ (closed-loop control at $750\ \frac{℃}{s}$).

Microscopic images of two cross sections in sample $C2$ are also shown in Figure 5-6. It is observed that the micrographs in this figure are also identical in terms of the general microstructure, grain size boundaries and volumetric fraction of each phase. Comparing Figure 5-5 with Figure 5-6, it is apparent that $C1$ has a smaller grain size compared to $C2$, which is due to the lower cooling rate of sample $C1$ as explained in Section 4.3. It is interesting that according to Figure 5-4, these samples have identical melt pool temperatures, thus, the only difference of these two samples are their cooling rates. Once again, the sole effect of the cooling rate on microstructure is observed by comparing microstructures of samples $C1$ and $C2$.

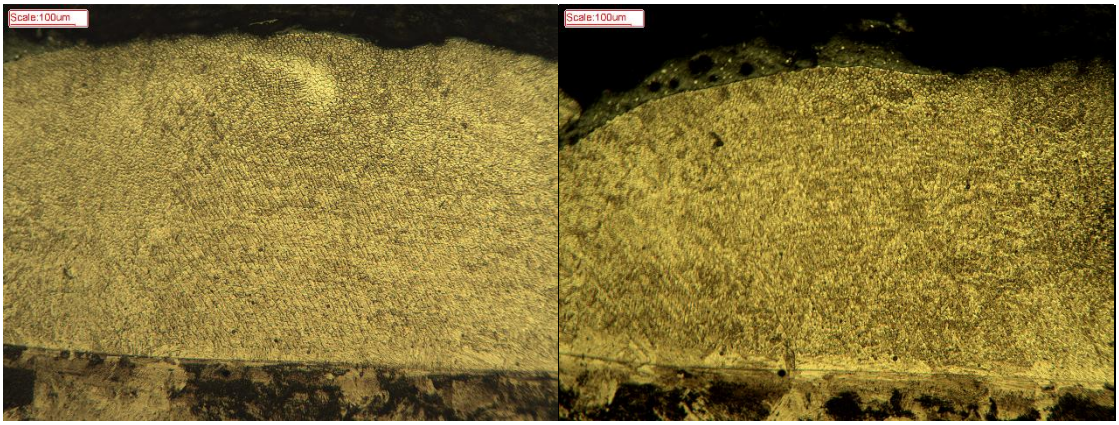

Figure 5-6 Micrographs from two different locations in sample $C2$ (closed-loop control at $210\ \frac{℃}{s}$).

In summary, these results show that the microstructure of a deposition can be controlled during the LAM process by controlling the cooling rate. There is a positive significant correlation between the closed-loop cooling rate response and microstructural evolutions in the claddings. The developed controller was able to control the cooling rate and thus provide a consistent microstructure during the LAM process, which is of crucial importance in all applications of the LAM in industry.

5.3 Microstructure Control in Multi-pass Cladding under Thermal Disturbances

While the closed-loop control process of the cooling rate was successful in achieving a consistent desired microstructure, the single-line cladding conditions are the most simple case of the LAM process. The performance of the proposed controller has to be evaluated under harsher conditions and process disturbances, which are present in industrial applications. When LAM is used in the rapid prototyping or coating technology, several lines of claddings are deposited beside each other to produce a deposition layer. Since these lines are deposited consecutively with narrow spacing or overlaps, the deposition of each line has an effect on the next or previous one. As each line is cladded, it gathers a certain amount of energy inside the substrate, hence, increasing the substrate's initial temperature and disturbing the thermal profile. As a result, each deposited line will undergo a different thermal process, which results in a different microstructure. On the other hand, open-loop deposition of different shapes on various geometries results in over heat input and disturbance that may cause excessive build-up of material, or lack of deposition. Overall, industrial applications of LAM require multi-pass claddings, which in turn introduce various disturbances to the thermal process of the system and its output metallurgical characteristics. On the other hand, there are case studies in which certain desired material

properties are required in certain sections of the cladding. Therefore, instead of a constant setpoint for the cooling rate, a changing setpoint is required to produce different material properties at different localized sections.

5.3.1 Cooling Rate Control using a PID Control

A more general experimental condition is required in order to analyze the performance of the developed closed-loop controller under process disturbances. As shown in Figure 5-7, three clad lines were deposited consecutively without any cooling in between. The length of each line is 90 mm, and the lines have a 5 mm distance between them. Thus, as each line is deposited, a certain amount of preheat is produced in the substrate, disturbing the initial thermal conditions of the system for the next deposition. Moreover, instead of having a constant setpoint, a stair case setpoint was assigned for the controller. The initial set point for the first half of each line is $430\,\frac{℃}{s}$, and then the closed-loop controller has to reach a setpoint of $850\,\frac{℃}{s}$. Therefore, the controller's performance is evaluated by introducing two disturbances: 1) preheat and 2) changing set point.

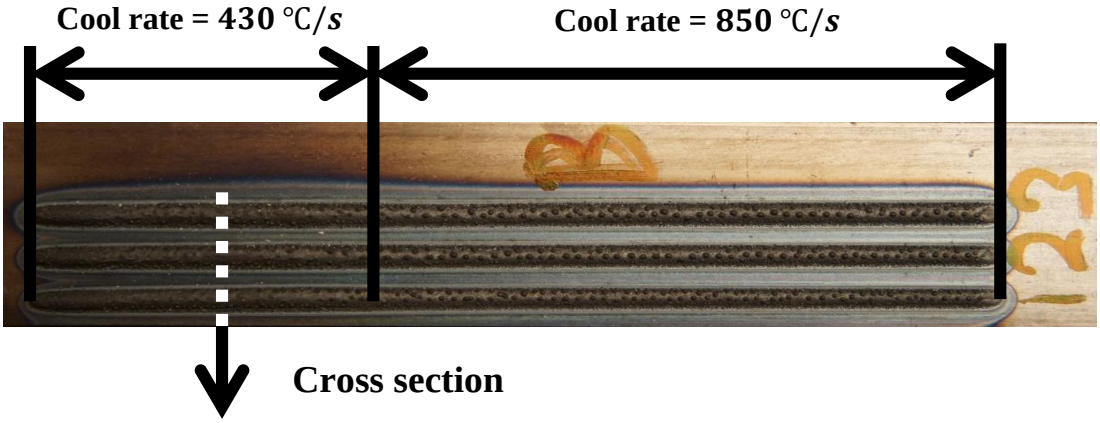

Figure 5-7 Multi-line claddings for evaluation of the microstructure controller.

Two samples F and G, were cladded by the closed-loop process with the same conditions as in Figure 5-7. The PID controller was tuned for the current setup. As observed in Table 5-1, due to the great nonlinearities of the system a new set of PID gains were required for each setpoint. However, it was intended to tune a single set of PID gains for the multi-line step setpoint for samples F and G, which was hard to achieve and required greater attention. The optimum set of PID gains tuned for the multi-line claddings with a step setpoint ($850\,\frac{℃}{s}$ and $430\,\frac{℃}{s}$) are listed in Table 5-2.

Table 5-2 Optimal PID gains for multi-line cladding with step set point.

Step Setpoint Cooling Rate	K_C	T_I	T_D
$F - G$ **(850** $\frac{℃}{s}$ **and 430** $\frac{℃}{s}$**)**	4	0.002	0

The closed-loop response of the cooling rate for samples F and G are illustrated in Figure 5-8 and Figure 5-9, respectively. The number ($n = 1, 2\ and\ 3$) after the sample number (i.e. Fn) indicates the deposition line (shown in Figure 5-7) in each sample. The controller is successful in achieving the desired setpoints; however, there are oscillations around the initial setpoint $430\frac{℃}{s}$. As discussed in Section 5.2.1, since $430\frac{℃}{s}$ is lower than the $850\frac{℃}{s}$, the oscillations are mainly considered to be noise in the program due to low pixel resolution at lower cooling rates. Moreover, since the optimal PID gains are assigned for the step setpoint which contains two cooling rate values, it has been tuned for a combination of both setpoints ($850\frac{℃}{s}$ and $430\frac{℃}{s}$). Thus, the PID gains do not satisfy the most optimum response for each of these setpoints individually, whereas, they are tuned to produce an average good response for both setpoints. Comparing closed-loop cooling rate responses of samples F and G, the general performance of the controller is satisfactory under disturbances.

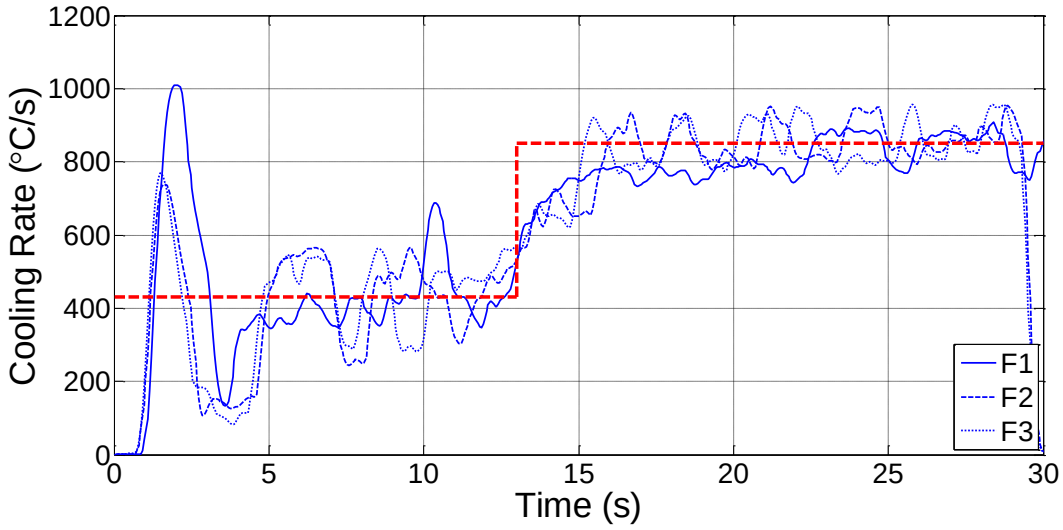

Figure 5-8 Closed-loop response of cooling rate for sample *F* (multi-line cladding with step setpoint).

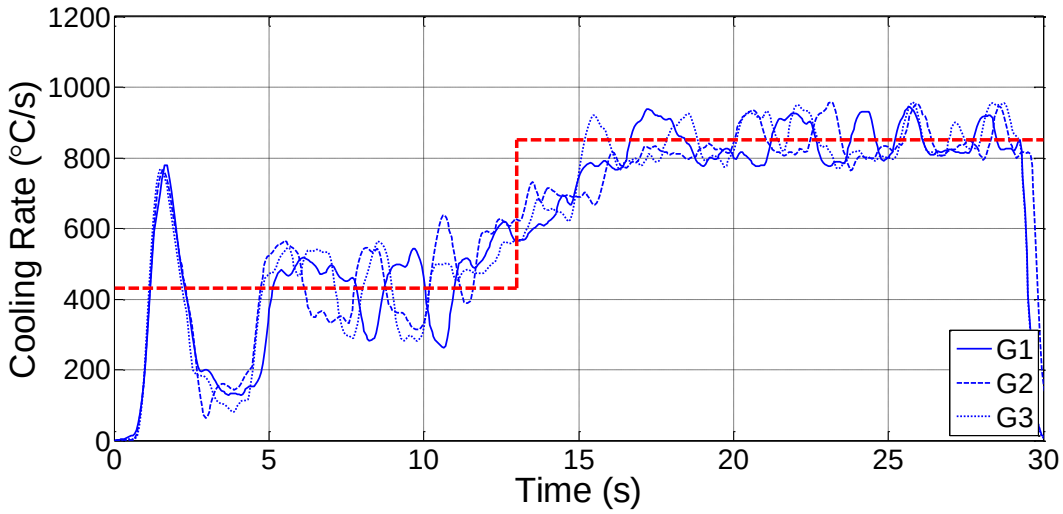

Figure 5-9 Closed-loop response of cooling rate for sample *G* (multi-line cladding with step setpoint).

The closed-loop traveling speeds of the two samples F and G are shown in Figure 5-10 and Figure 5-11, respectively. It is noticeable that $F1$ has a different path of speed compared to the other lines ($F2$ and $F3$). As a result, the closed-loop cooling rate response of $F1$ is also different compared to $F2$ and $F3$, which are the second and third lines of deposition in sample F. The effect of this small

divergence of $F1$ on its microstructure will be discussed in the later sections. On the other hand, all the three deposited lines in the G sample ($G1, G2$ and $G3$), have similar closed-loop traveling speeds and cooling rates. It is apparent that the controller has a small malfunction in $F1$. The major reason to include sample F is to study the effects of a malfunctioning controller on the final microstructure, otherwise, all other closed-loop depositions produced good results similar to sample G.

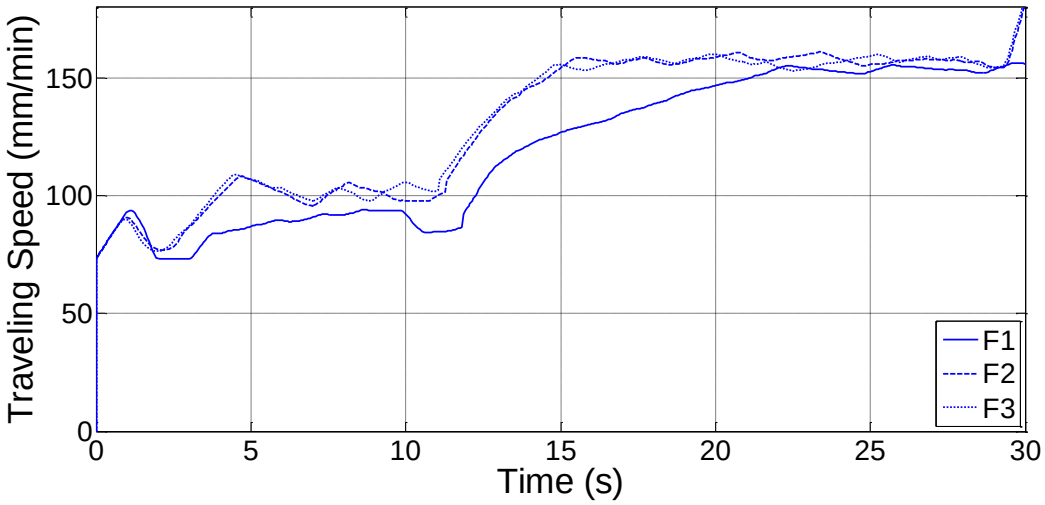

Figure 5-10 Closed-loop traveling speeds of sample F ($430\ \frac{℃}{s} - 850\ \frac{℃}{s}$).

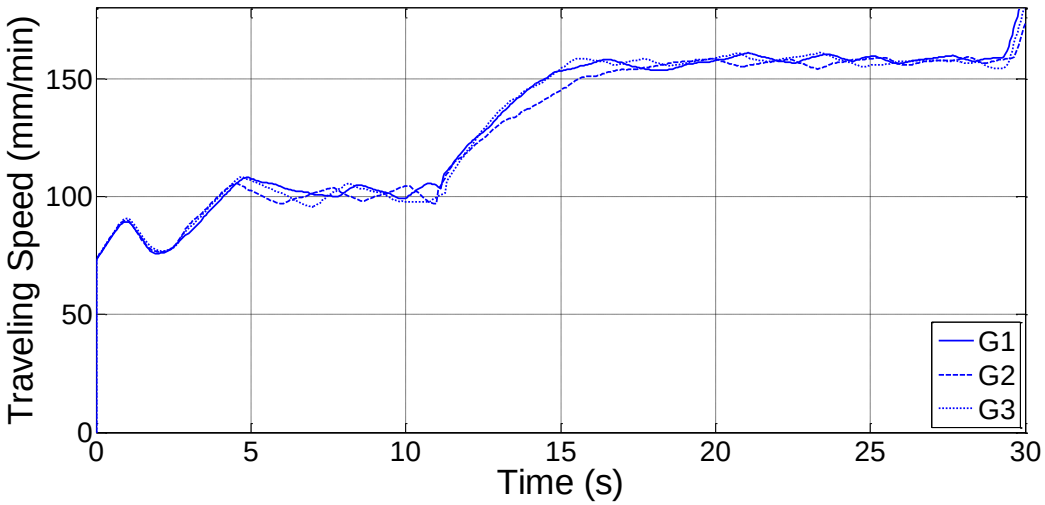

Figure 5-11 Closed-loop traveling speeds of sample G ($430\ \frac{℃}{s} - 850\ \frac{℃}{s}$).

The melt pool temperature of samples F and G are illustrated in Figure 5-12 and Figure 5-13, respectively. As expected, the $F1$ line has a slightly different trend of temperature variation compared to other lines in Figure 5-12. An unanticipated finding is that the melt pool temperature of the $430\ \frac{℃}{s}$ and $850\ \frac{℃}{s}$ sections are not different. The temperature is found to be consistent although the cooling rate and the traveling speed are changing. This finding further supports the idea that small variations in the traveling speed do not affect the melt pool temperature, whereas, they influence the cooling rate and thus the microstructure significantly.

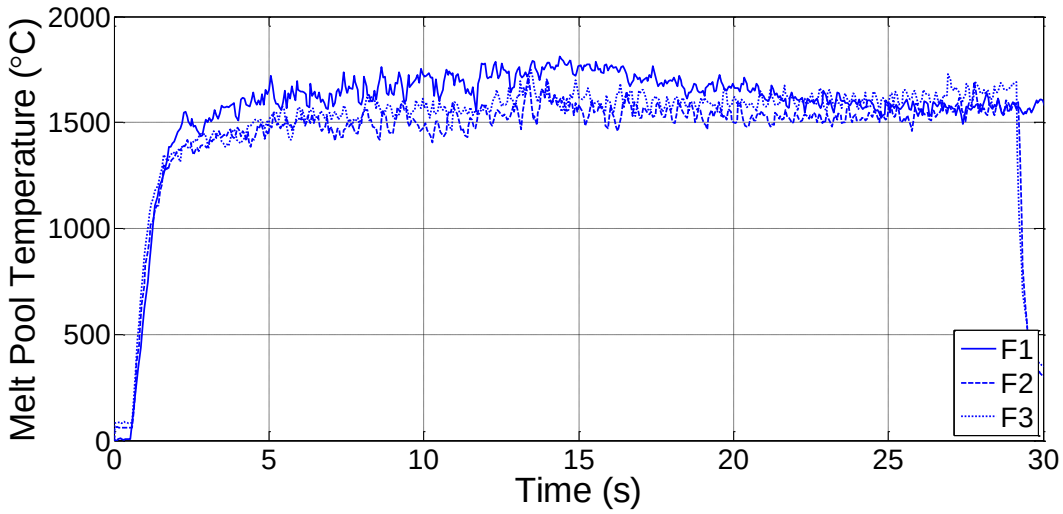

Figure 5-12 Closed-loop response of the melt pool temperature for sample F ($\mathbf{430}\ \frac{℃}{s} - \mathbf{850}\ \frac{℃}{s}$).

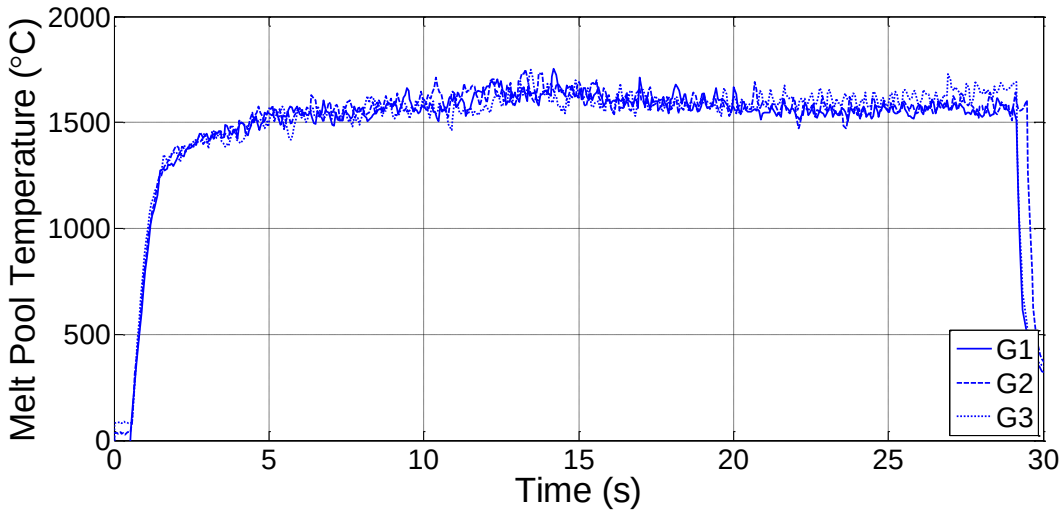

Figure 5-13 Closed-loop response of the melt pool temperature for sample G ($\mathbf{430}\ \frac{℃}{s} - \mathbf{850}\ \frac{℃}{s}$).

These results suggest that the controller is able to conveniently track a desired response for the cooling rate at different setpoints. However, a malfunction in the controller response is intentionally included in the results to study the influence of an uncontrolled process on microstructural evolutions.

5.3.2 Microstructure Control and Results

Microstructure consistency and control were studied for single-line claddings in the closed-loop process. It is now crucial to investigate the microstructure control in the closed-loop process of the multi-line depositions. In order to do so, each sample was sectioned at two locations, one in the $430\ \frac{℃}{s}$ region and the other in the $850\ \frac{℃}{s}$ region, as shown in Figure 5-7. If the microstructural trends of each line in samples F and G are similar, the controller has been successful in controlling the microstructure during the LAM process.

Figure 5-14 and Figure 5-15 illustrate the microstructures in sample F, at the low ($430\ \frac{℃}{s}$) and high ($850\ \frac{℃}{s}$) cooling rate regions, respectively. As expected, samples $F2$ and $F3$ have similar microstructures at both cooling rates, however, the deposited sample $F1$ differs. This variation in microstructure is a result of a different trend of cooling rate and traveling speed for $F1$ compared to the other two lines, as seen in Figure 5-8 and Figure 5-10. However, similar microstructures observed in samples$F2$ and $F3$ support the consistency of performance in the closed-loop control process.

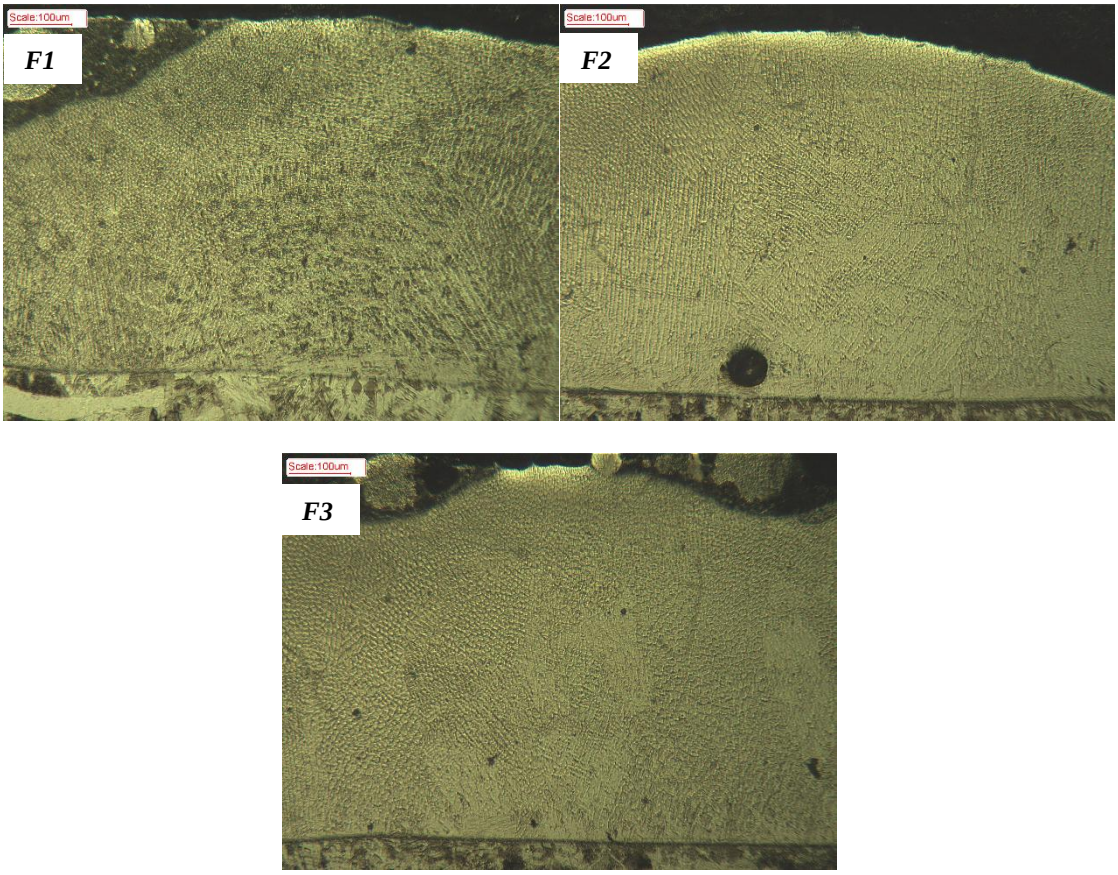

Figure 5-14 Micrographs of lines $F1$, $F2$ and $F3$ at low cooling rate (closed-loop control at $430\ \frac{℃}{s}$).

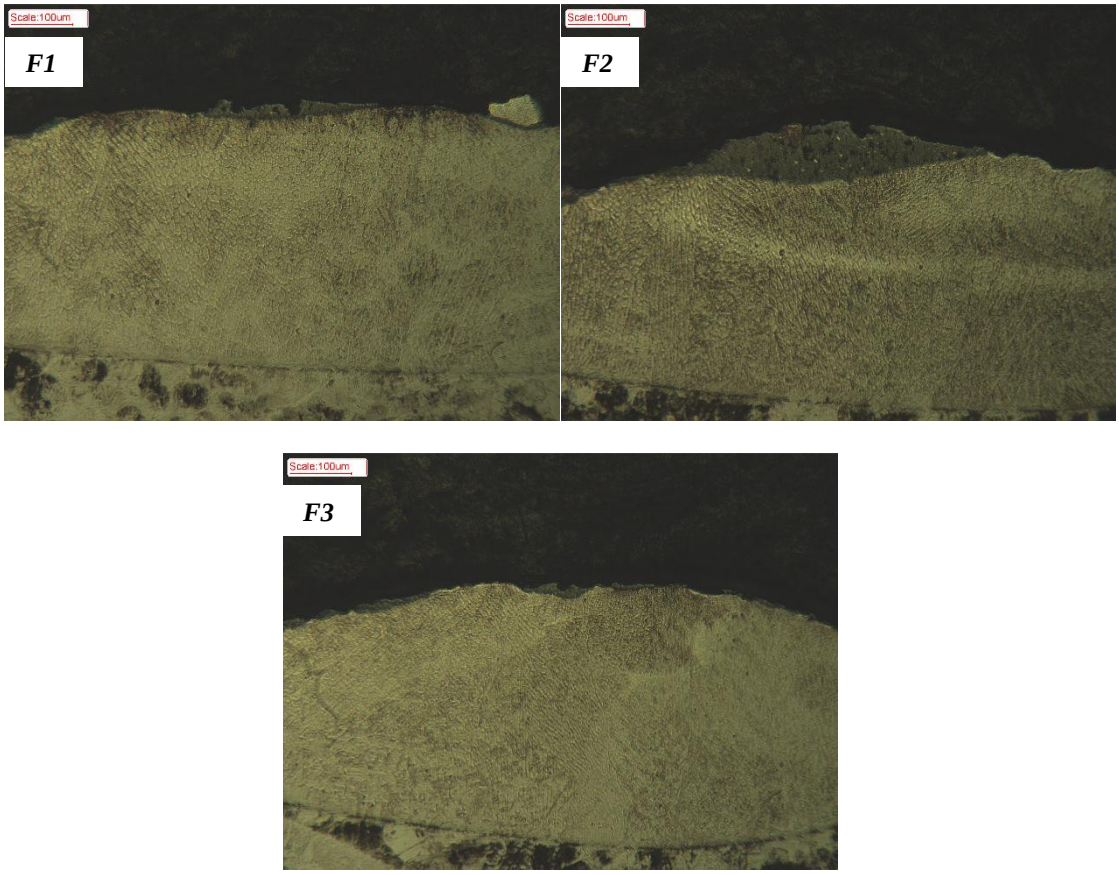

Figure 5-15 Micrographs of lines $F1$, $F2$ and $F3$ at high cooling rate (closed-loop control at $850\ \frac{℃}{s}$).

To better illustrate the microstructure control and consistency in the F samples, higher magnification micrographs of these samples are presented in Figure 5-16 and Figure 5-17. As explained previously, lines $F2$ and $F3$ have very similar microstructures, whereas, line $F1$ is different due to the malfunction of the controller.

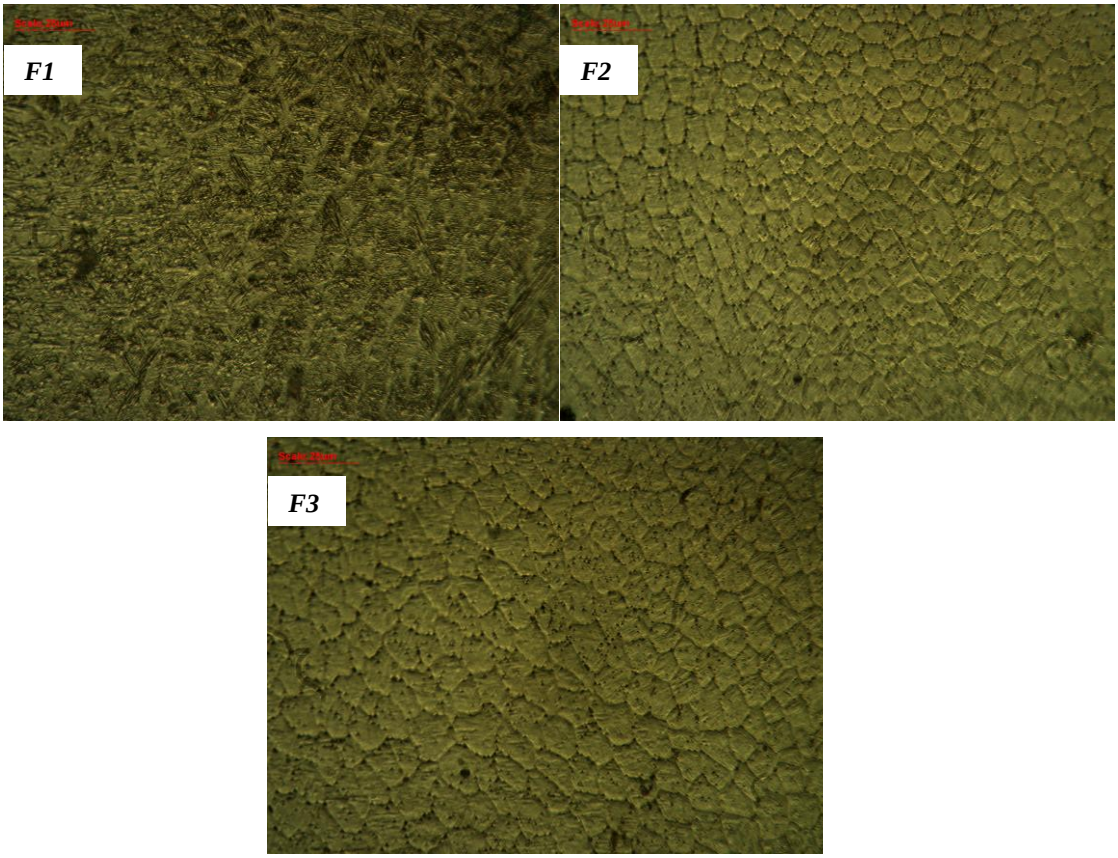

Figure 5-16 High magnification micrographs of lines $F1$, $F2$ and $F3$ at low cooling rate (closed-loop control at $430\ \frac{℃}{s}$).

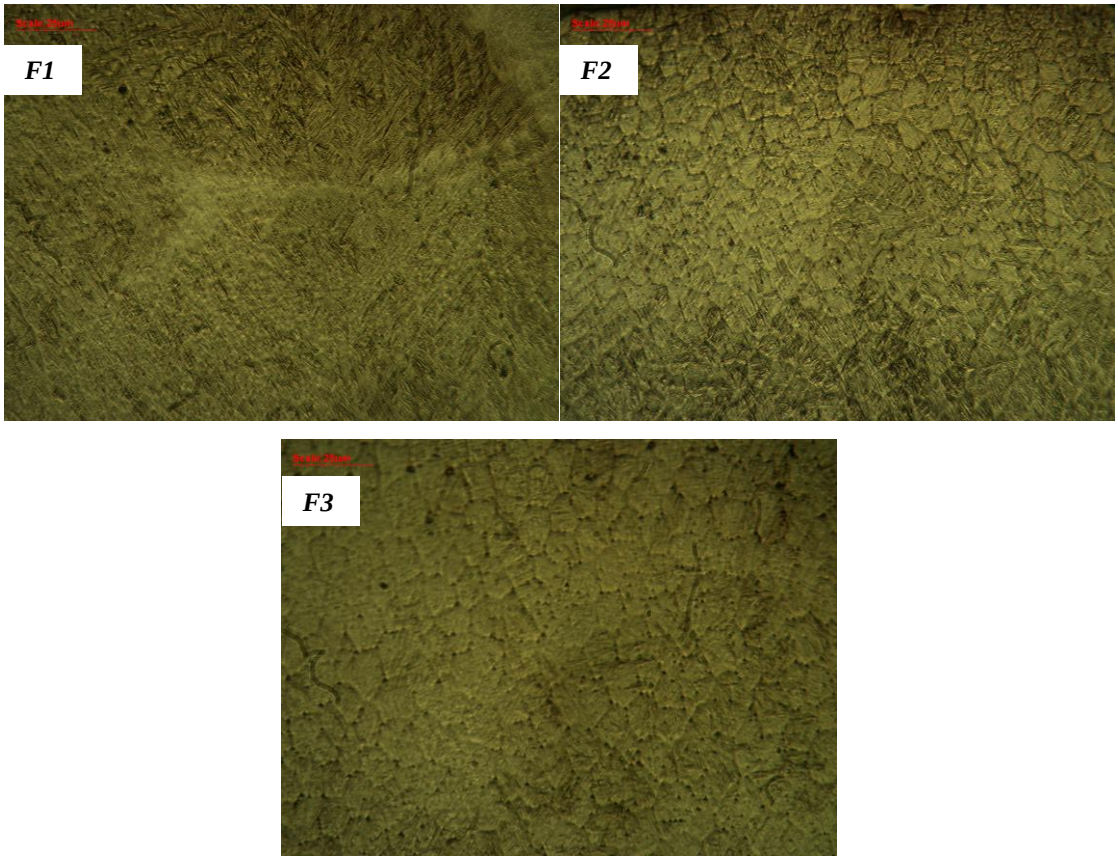

Figure 5-17 High magnification micrographs of lines $F1$, $F2$ and $F3$ at high cooling rate (closed-loop control at $850\ \frac{℃}{s}$).

Turning to further analysis of microstructure control, a set of samples designated G were produced in which the controller performed correctly for all deposited lines. Figure 5-18 and Figure 5-19 present micrographs of sample G, at low ($430\ \frac{℃}{s}$) and high ($850\ \frac{℃}{s}$) cooling rate regions, respectively. In contrast to sample F, it is clear that all deposited lines in G have consistent similar microstructures at both cooling rates. Higher magnification micrographs of the G samples are also illustrated in Figure 5-20 and Figure 5-21.

All three lines in sample G have a similar microstructure in terms of: (1) grain size, (2) cellular and columnar growth, (3) volumetric percentage of the columnar and cellular regions, and (4) volumetric percentage of the γ-austenite and δ-ferrite phases. Thus, by implementing a closed-loop control for the cooling rate of multi-line claddings in samples F and G, their microstructures were controlled consistently throughout the deposition.

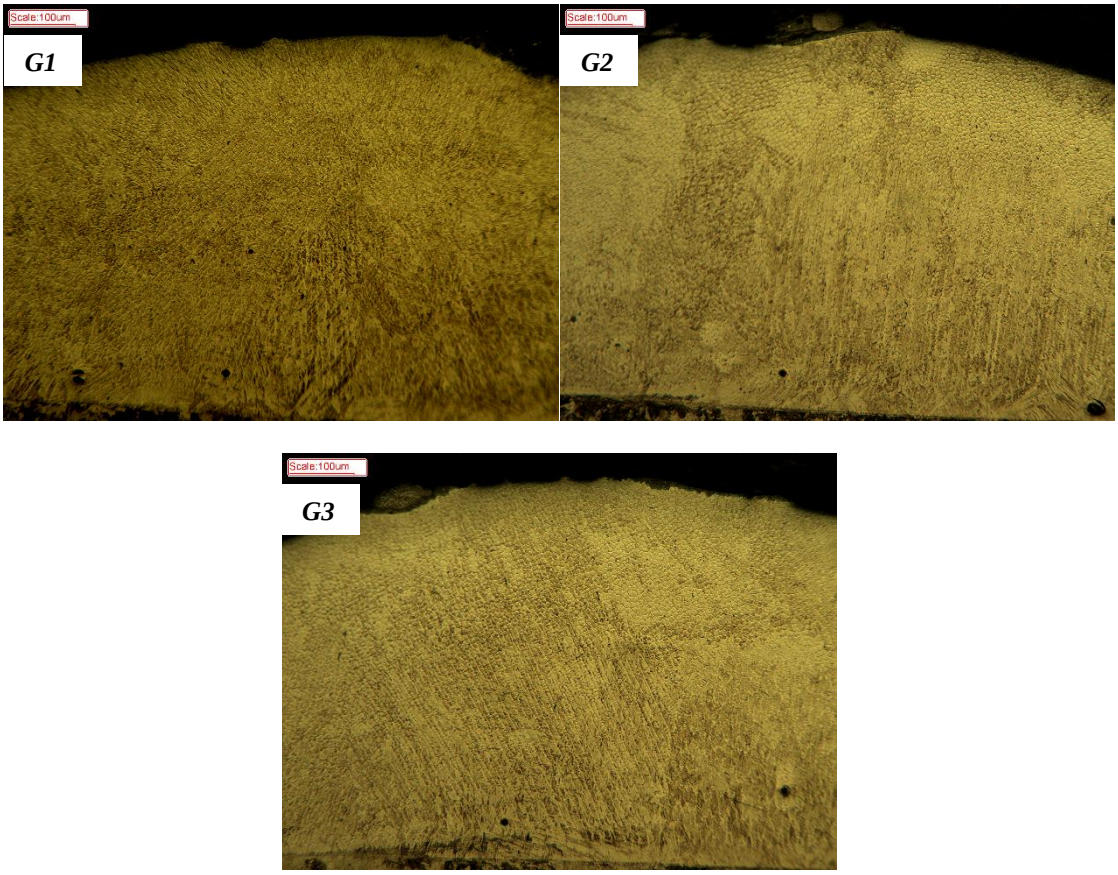

Figure 5-18 Micrographs of lines $G1$, $G2$ and $G3$ at low cooling rate (closed-loop control at $430\ \frac{℃}{s}$).

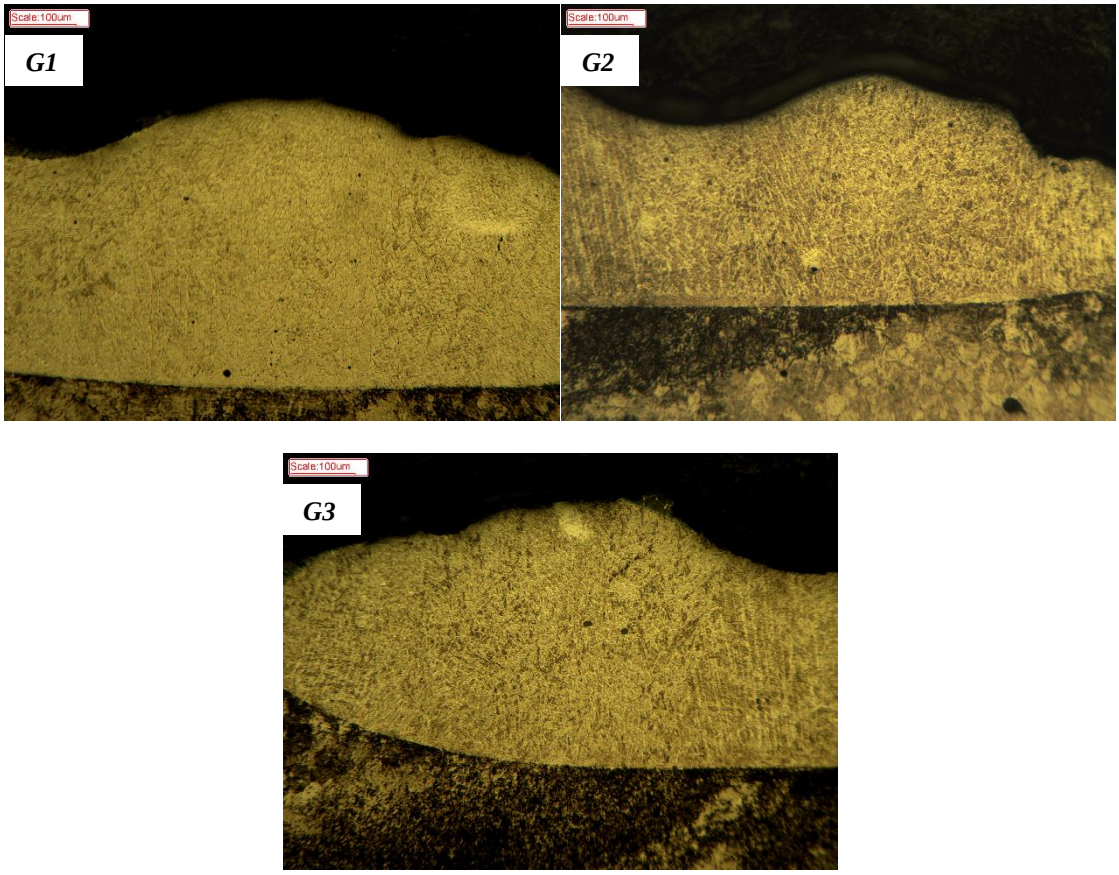

Figure 5-19 Micrographs of lines $G1$, $G2$ and $G3$ at high cooling rate (closed-loop control at $850\ \frac{℃}{s}$).

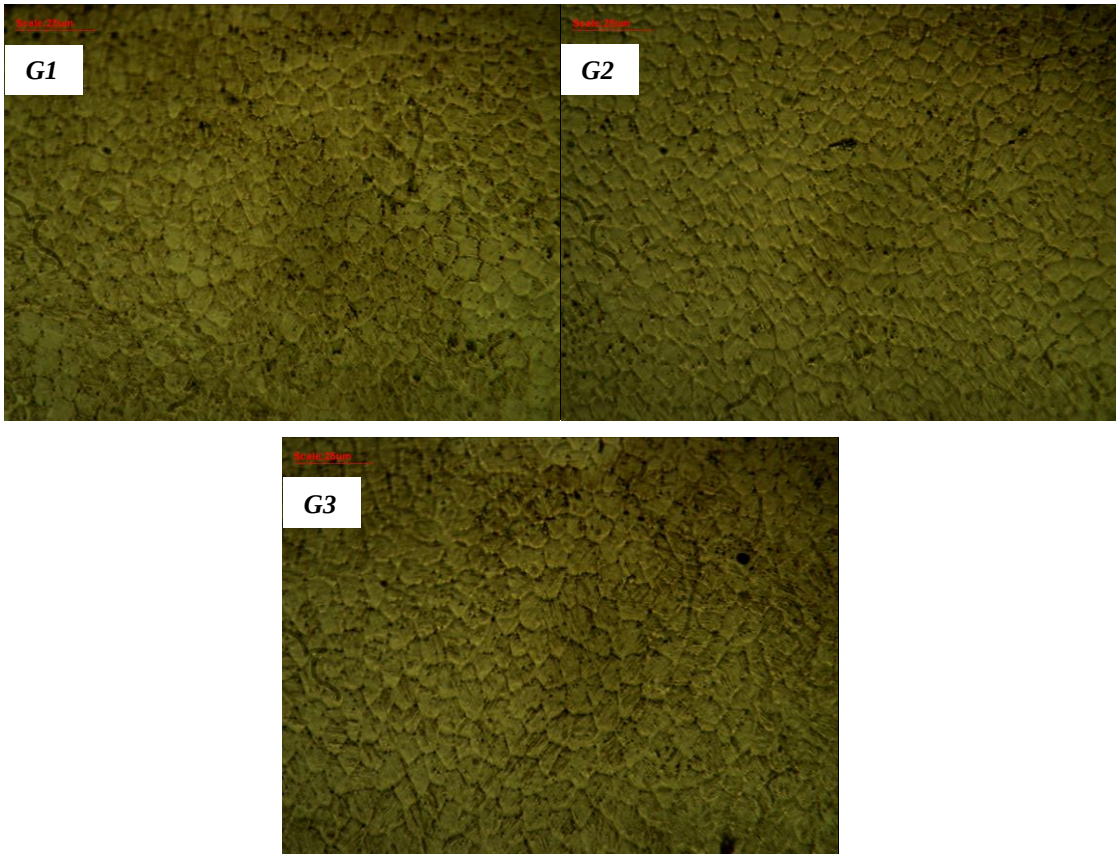

Figure 5-20 High magnification micrographs of lines $G1$, $G2$ and $G3$ at low cooling rate (closed-loop control at $430\ \frac{℃}{s}$).

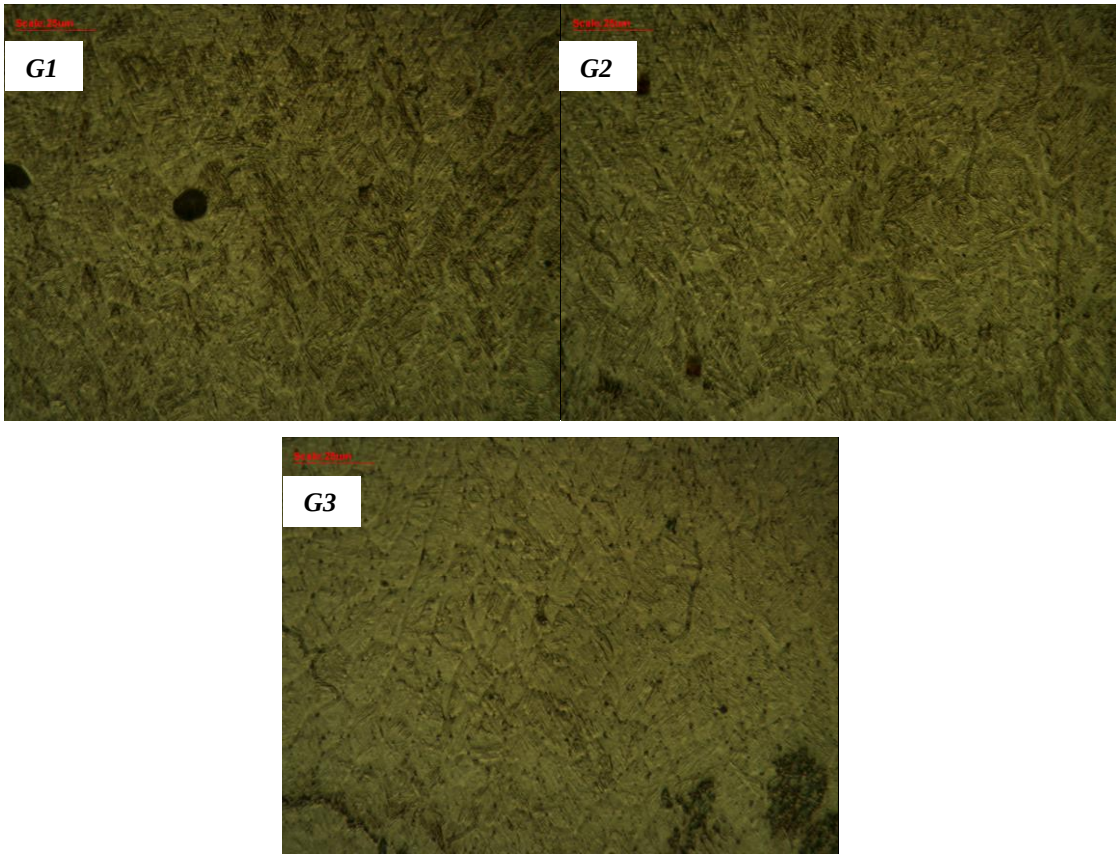

Figure 5-21 High magnification micrographs of lines $G1$, $G2$ and $G3$ at high cooling rate (closed-loop control at $850\ \frac{℃}{s}$).

To better study the grain size control in the F and G samples, their ASTM grain size number were measured for the low cooling rate region, $C = 850\frac{℃}{s}$, (Figure 5-16 and Figure 5-20) by the Heyn lineal intercept procedure presented in Section 4.3.1. According to Table 5-3, all the F and G lines have similar grain size numbers, which indicates consistent grain size dimensions produced by the closed-loop microstructure controller. It has to be noted that since $F1$ did not have a similar cellular structure as $F2$ and $F3$, it's dimensions were note measured. Moreover, since at the high cooling rate, $C = 430\frac{℃}{s}$, (Figure 5-17 and Figure 5-21), the F and G samples had a primary martensite phase with a needle-like microstructure as opposed to a cellular one, grain size measurements were not performed. However, it is obvious that even at high cooling rate the microstructure controller has been successful in achieving a consistent microstructure throughout the process.

Table 5-3 ASTM grain size number were measured for the low cooling rate region, $C = 430\frac{℃}{s}$.

Sample No.	$F1$	$F2$	$F3$	$G1$	$G2$	$G3$
ASTM Grain Size No.	-	10.7	10.6	11.5	11.8	11.3

It is noteworthy to point out that although the melt pool temperature is constant for both cooling rate regions (Figure 5-12 and Figure 5-13), the microstructures of the low cooling rate region (Figure 5-14 and Figure 5-18) is different to that of the higher cooling rate (Figure 5-15 and Figure 5-19) for both samples. Hence, it is concluded that control of the melt pool temperature does not satisfy a controlled microstructure, whereas, a controlled cooling rate results in a controlled microstructure. This is to the contrary of the majority of reports available in literature, which have investigated thermal and material control of the process.

Moreover, in both samples, the low cooling rate region ($430\frac{℃}{s}$) has a larger grain size compared to the higher cooling rate region ($850\frac{℃}{s}$), which is in complete agreement with the results presented in Chapter 4.

5.3.3 Micro Hardness Analysis in Closed-loop Control of the Microstructure

For further analysis of a controlled microstructure by the developed closed-loop microstructure controller, micro hardness tests were performed on the deposited clad lines in sample G as shown in Table 5-4 and Table 5-5. It has to pointed out that all micros hardness tests were performed at similar locations for all samples at the top of the clad cross section. Another sign of a controlled microstructure is a similar micro hardness for all the deposited samples. According to results listed in Table 5-4, all the G samples have very close micro hardness results at low the cooling rate ($430\frac{℃}{s}$), specially $G1$ and $G3$, which are similar. However, line $G2$ has some differences compared to the other two lines, which requires further analysis. One reason for this decrease in hardness may be the slight increase in grain size for $G2$ as shown by Table 5-3.

On the other hand, Table 5-5 indicates a significant approval of microstructure control for the deposited lines at the high cooling rate ($850\frac{℃}{s}$). Interestingly, all the G lines have a similar micro

hardness that is caused by a consistent similar microstructure for all these samples. Overall, micro hardness tests further proved the correct functionality of the developed real time microstructure controller for the LAM process.

Table 5-4 Micro hardness results for lines $G1$, $G2$ and $G3$ at low cooling rate (closed-loop control at $430\ \frac{℃}{s}$).

Sample No.	$G1$	$G2$	$G3$
Micro Hardness (HVN1000)	330	229	336

Table 5-5 Micro hardness results for lines $G1$, $G2$ and $G3$ at high cooling rate (closed-loop control at $850\ \frac{℃}{s}$).

Sample No.	$G1$	$G2$	$G3$
Micro Hardness (HVN1000)	426	439	467

5.3.4 Dilution and Clad Height Analysis in Closed-loop Control of the Microstructure

Although, results indicate that the microstructure has been controlled by the developed closed-loop system, the controller's effect on the physical properties (e.g. clad height and dilution) of the clad have not been studied. The clad height and dilution for the F and G samples are presented in Table 5-6 and Table 5-7, respectively. According to Table 5-6, the first deposition line of the F sample ($F1$) has different dilution and clad height values compared to the other two lines ($F2$ and $F3$). As discussed earlier, this variation is caused by the malfunction of the controller and a different cooling rate path (see Figure 5-8 and Figure 5-10). Hence, apart from having a different microstructure, $F1$ has a different dilution and clad height as well. On the other hand, a consistent dilution and clad height is observed in all deposition lines of the G sample, which is due to the consistent performance of the microstructure

controller. Thus, a closed-loop microstructure process with a constant cooling rate results in a controlled clad height and dilution.

However, the low ($430\ \frac{℃}{s}$) and the high cooling regions ($800\frac{℃}{s}$) have different dilution and clad height values in Table 5-6and Table 5-7. The different clad height and dilution is a concern since in many applications require different desired microstructures with a constant geometry. The changing clad height for different closed-loop microstructure responses requires further attention and analysis.

Table 5-6 Dilution and clad height of the *F* sample for two cooling rate setpoints.

Sample	$\boldsymbol{F1}$ $(\mathbf{430}\frac{℃}{s})$	$\boldsymbol{F1}$ $(850\frac{℃}{s})$	$\boldsymbol{F2}$ $(\mathbf{430}\frac{℃}{s})$	$\boldsymbol{F2}$ $(850\frac{℃}{s})$	$\boldsymbol{F3}$ $(\mathbf{430}\frac{℃}{s})$	$\boldsymbol{F3}$ $(850\frac{℃}{s})$
Clad Height	$123\ \mu m$	$61\ \mu m$	$151\ \mu m$	$87\ \mu m$	$151\ \mu m$	$83\ \mu m$
Dilution	23%	48%	14%	30%	15%	36%

Table 5-7 Dilution and clad height of the *G* sample for two cooling rate setpoints.

Sample	$\boldsymbol{G1}$ $(\mathbf{430}\frac{℃}{s})$	$\boldsymbol{G1}$ $(850\frac{℃}{s})$	$\boldsymbol{G2}$ $(\mathbf{430}\frac{℃}{s})$	$\boldsymbol{G2}$ $(850\frac{℃}{s})$	$\boldsymbol{G3}$ $(\mathbf{430}\frac{℃}{s})$	$\boldsymbol{G3}$ $(850\frac{℃}{s})$
Clad Height	$138\ \mu m$	$75\ \mu m$	$145\ \mu m$	$70\ \mu m$	$140\ \mu m$	$86\ \mu m$
Dilution	18%	38%	16%	41%	18%	39%

Together these results provide significant insight into microstructure control of the LAM process. A controller was designed to control the cooling rate so that the microstructure will be controlled. Results prove that the solidification structures during the LAM process can be controlled by the developed closed-loop control process. The controller is the first of its' kind in the LAM industry, since it can produce microstructures with a desired grain size derived from cellular and columnar growth solidification modes, volumetric percentage of the columnar and cellular regions, and volumetric percentage of different phases in real time. The growth of the cellular and columnar regions in during

metal deposition may also be controlled based on the cooling rate . Moreover, the volumetric percentage of each phase of the deposition can be controlled and set in-situ during deposition. The applications of the developed microstructure controller are quite broad and can be applied to various industries and applications.

Chapter 6
Conclusion and Future Work

6.1 Conclusions

The purpose of the current study was to develop a real-time monitoring system and closed-loop process for real time microstructure control in laser additive manufacturing. As a result, the following achievements and contributions were obtained:

1. **Development of an infrared-based feedback signal for monitoring the cooling rate and melt pool temperature of the process in real time.** An IR camera was used to provide on-line thermographic images of the LAM process. With the help of thermal image analysis techniques, thermal images were processed in real time in Labview to obtain thermal information of the process. These information include: (1) melt pool temperature, (2) cooling rate and (3) thermal maps (1-D, 2-D and 3-D). The development of such a system is first of its' kind in the field since, previous researchers were only able to measure the cooling rate off-line due to the very high cooling rate values and limitation of thermal monitoring apparatus.

2. **Establishment of a closed-loop PID controller for the cooling rate in LAM.** A PID controller was developed to tune the traveling speed. The controller was designed to control the cooling rate around operating points in order to achieve a novel closed-loop microstructure process.

3. **Conduction of several experiments to study the combined effect of melt pool temperature and cooling rate on clad microstructure.** Experiments were designed to analyze the influence of melt pool temperature and cooling rate on detailed microstructure such as grain size, phase transformations and morphology. The powder deposition density (PDD) and effective energy per unit area (E) were depicted to represent combined changes of the laser power, traveling speed and powder feed rate. Initially, samples were deposited having similar E and PDD values but, different laser processing parameters. Different microstructures were observed for the samples. However, the results has shown that although the combined parameters (E and PDD) were the same for all samples, their cooling rates and melt pool temperatures were different. There was a significant correlation between the cooling rate and microstructural evolutions. However, melt pool temperatures

were not as effective on the microstructure as the cooling rates. Thus, the cooling rate was identified as the main influencing parameter on the microstructure, which has to be controlled during the process.

4. **Study of cooling rate effects on clad microstructure, and understanding cooling rate changes with respect to traveling speed variations.** Further analysis was required to study the sole effect of cooling rate on the clad microstructure. A new set of *B* experiments were conducted; increasing the travelling speed, and keeping the laser power and powder feed rate constant during single-line claddings. The cooling rate had direct effect on: (1) the volumetric percentage of each phase inside the microstructure, (2) formation and growth of different γ-austenite and δ-ferrite phases, and (3) grain size and grain boundaries. The increasing speed created an increasing trend for the cooling rate and a decreasing trend for the melt pool temperature. Interestingly, a linear relation was observed between travelling speed and the cooling rate (and melt pool temperature as well).

5. **Design and implementation of a closed-loop PID controller for the cooling rate, and microstructure analysis of the closed-loop process.** Different single-line and multi-line claddings were deposited by the developed closed-loop control process in order to control the cooling rate around the operating setpoints. Two single-line claddings with constant cooling rate setpoints ($C_1 = 750\ \frac{℃}{s}$ and $C_2 = 210\ \frac{℃}{s}$) were deposited and evaluated. The controller was successful in controlling the operating cooling rate setpoints, and microstructure analysis revealed a consistent controlled microstructure throughout the cladding line. The closed-loop process was also evaluated in multi-line LAM depositions with a staircase stepoint. The controller's performance was satisfactory in achieving the desired cooling rates in real time. More importantly, it was observed that the multi-lines with similar cooling rates, which were deposited besides each other had consistent similar microstructures due to the controlled cooling rate.

   The developed controller is a breakthrough in the LAM industry, since it can provide controlled microstructure and morphology in real time.

6. **Evaluation of cooling rate and melt pool temperature effects on clad height and dilution.** Clad height and dilution of samples were also measured during the different closed-loop experiments proposed in the research. Clad height decreased with the

increasing melt pool temperature; however, clad dilution was not related to the melt pool temperature. In fact, dilution increased linearly with the cooling rate. Thus, further analysis showed that dilution was also consistent during the single-line and multi-line closed-loop process because of the controlled cooling rate.

6.2 Future Work

The above-mentioned achievements provide a great step forward in achieving an automated LAM process with desired mechanical and metallurgical properties. Although, a system was developed to control the microstructure in real time, the performance of the closed-loop system has not been evaluated in complex conditions. Nonetheless, a few more steps are required to transform the multidisciplinary technology to a fully functional automated process.

1. **Including the influence of other processing parameters in the closed-loop process as controlling actions to improve controller performance in microstructure control:** While, the current cooling rate controller provides great insight into microstructure control and has proven the feasibility of microstructure control in real time, it has not been evaluated in complex conditions for a variety of materials. Apart from the travelling speed, other processing parameters such as the laser power, laser beam diameter and powder feed rate affect the microstructure. In order to generalize the microstructure control process it is required to include all influencing parameters in the final controller. Hence, a multi input multi output (MIMO) system has to be identified to completely model and control the deposited LAM microstructure.
2. **Development of a feedback control for the melt pool temperature in order to obtain better microstructure control results:** Melt pool temperature was identified as the second most important output parameter that defined the microstructure. Therefore, a complete microstructure controller will definitely involve a closed-loop process for the melt pool temperature as well. For the current controller to be complete in terms of microstructure control it requires to interact the role of melt pool temperature as well.
3. **Integration of a closed-loop clad geometry controller with the developed microstructure control process to achieve a fully automated machine:** The current developed closed-loop process is only able to control the cooling rate and consequently the

microstructure in real time. The mechanical and material properties of the deposition are controlled with this process; however, the geometrical properties of the clad such as clad height and width are still sensitive to disturbances and thus require a separate controlling scheme. It was observed that constant closed-loop cooling rates result in consistent geometry. However, comparing different cooling rates it is apparent that at different cooling rates different geometries are present. In majority of industrial applications, although, material properties of a clad are of most importance, a consistent clad geometry is required for the different microstructures. Hence, a feedback controller is also required to produce desired clad geometries for different controlled microstructures.

4. **Development and implementation of different type of real time controllers and system identification techniques for microstructure modeling and control:** In this research, only one type of controller namely PID was implemented and evaluated for microstructure control. There are several other types of controllers available, which may produce better results; however, the majority of these controllers are model-based. Various microstructure models can be obtained by system identification techniques to gain better insight into the process. With the development of different process models, several controllers can be implemented and experimented to yield better microstructure results in real time.

5. **Development of a numerical model for microstructural evolutions during LAM**: In this thesis the microstructure was controlled indirectly by means of the thermal process. It is complicated to directly observe the evolution of the microstructure by experimental technology due to the rapid solidification of the deposited coatings. An alternative method for studying this problem is by using numerical simulation for the evolution of the microstructure. The majority of the current numerical models are verified by experimental results due to the lack of real time thermal recordings. However, a complete numerical model can be achieved for microstructural evolutions in LAM based on the real time monitored results of the cooling rate and melt pool temperature obtained in the current setup.

6. **Extension of the microstructure controller to commercial materials:** To extend the application of the developed closed-loop process to fabrication of complex tools and parts, it is necessary to examine the performance of the developed system with several

commercial materials such as other Iron alloys, Titanium, Nickel, Cobalt and Tungsten based alloys.

Bibliography

[1] E. Toyserkani, A. Khajepour, and S. Corbin, *Laser Cladding*. Florida: CRC Press, 2005.

[2] D. D. Gu, W. Meiners, K. Wissenbach, and R. Poprawe, "Laser additive manufacturing of metallic components: materials, processes and mechanisms," *Int. Mater. Rev.*, vol. 57, no. 3, pp. 133–164, May 2012.

[3] "Cad Model." [Online]. Available: www.plastnett.org.

[4] "Powder." [Online]. Available: http://en.wikipedia.org/wiki/File:Rhodium_powder_pressed_melted.jpg.

[5] "Control." [Online]. Available: www.laserdesign.com.

[6] "Laser." [Online]. Available: breastcancerinfoblog.com.

[7] T. H. MAIMAN, "Stimulated Optical Radiation in Ruby," *Nature*, vol. 187, no. 4736, pp. 493–494, Aug. 1960.

[8] P. A. Ciraud, "Process and Device for the Manufacture of any Objects Desired from any Meltable Material," *FRG Discl. Publ.*, 1972.

[9] C. O. Brown, E. M. Breinan, and B. H. Kear, "Deposition from wire feedstock into an energy beam," 4323756, 1982.

[10] G. Gnanamuthu, "Surface alloying and trasnformation hardening using an industrial laser," *JOM*, vol. 27, no. 12, p. A61, 1975.

[11] F. Seaman, "Using industrial laser to surface harden and alloy," *Met. Prog.*, vol. 108, no. 3, p. 67, 1975.

[12] V. M. Weerasinghe and W. M. Steen, "Laser cladding with pneumatic powder delivery," in *Lasers in Materials Processing*, 1983, pp. 166–174.

[13] M. L. Griffith, J. T. Keicher, J. A. Romero, J. E. Smugeresky, L. D. Harwell, and D. L. Greene, "Laser engineered net shaping for the fabrication of metallic components," *Am. Soc. Mech. Eng. Mater. Div. Adv. Mater. Dev. Charact. Process. Mech. Behav.*, vol. 74, pp. 175–176, 1996.

[14] J. Mazumder, D. Dutta, N. Kikuchi, and A. Ghosh, "Closed loop direct metal deposition: art to part," *Opt. Lasers Eng.*, vol. 34, no. 4–6, pp. 397–414, Oct. 2000.

[15] L. Fang, L. Rocco, C. Andrew, S. Martin, O. William, and Y. Jian-hua, "Characteristics of Stellite 6 Deposited by Supersonic Laser Deposition Under Optimized Parameters," *J. Iron Steel Res. Int.*, Feb. 2013.

[16] J. Beuth, J. Fox, J. Gockel, C. Montgomery, R. Yang, H. Qiao, P. Reeseewatt, A. Anvari, S. Narra, and N. Klingbeil, "Process Mapping for Qualification Across Multiple Direct Metal Additive Manufacturing Processes," in *Proceedings 2013 Solid Freeform Fabrication Symposium*, 2013, no. August, pp. 655–665.

[17] M. A. McLean, "Laser direct casting of high nickel alloy parts," *Met. Powder Rep.*, vol. 53, no. 9, p. 57, Sep. 1998.

[18] G. K. Lewis and D. A. Cremers, "Overview of laser technology at Los Alamos National Laboratory," *J. Laser Appl.*, vol. 7, no. 4, p. 224, Aug. 1995.

[19] L. Xue and M. U. Islam, "Free-form laser consolidation for producing metallurgically sound and functional components," *J. Laser Appl.*, vol. 12, no. 4, p. 160, Aug. 2000.

[20] J. M. Wilson and Y. C. Shin, "Microstructure and wear properties of laser-deposited functionally graded Inconel 690 reinforced with TiC," *Surf. Coatings Technol.*, vol. 207, pp. 517–522, Aug. 2012.

[21] "TruLaser Cell." [Online]. Available: http://www.trumpf-laser.com/en/products/laser-systems/3d-laser-processing-systems.html.

[22] "Concept Laser." [Online]. Available: http://www.concept-laser.de/en/home.html.

[23] "Optomec." [Online]. Available: http://www.optomec.com.

[24] "DM3D." [Online]. Available: http://www.pomgroup.com/.

[25] "BeAM." [Online]. Available: http://www.beam-machines.fr/uk/en/.

[26] F. Arcella, "Producing titanium aerospace components from powder using laser forming," *JOM*, vol. 52, no. 5, pp. 28 – 30, 2000.

[27] E. Toyserkani, A. Khajepour, and S. Corbin, "3-D finite element modeling of laser cladding by powder injection: effects of laser pulse shaping on the process," *Opt. Lasers Eng.*, vol. 41, no. 6, pp. 849–867, Jun. 2004.

[28] K. Dai and L. Shaw, "Thermal and mechanical finite element modeling of laser forming from metal and ceramic powders," *Acta Mater.*, vol. 52, no. 1, pp. 69–80, Jan. 2004.

[29] X. He and J. Mazumder, "Transport phenomena during direct metal deposition," *J. Appl. Phys.*, vol. 101, no. 5, p. 053113, Mar. 2007.

[30] X. He, G. Yu, and J. Mazumder, "Temperature and composition profile during double-track laser cladding of H13 tool steel," *J. Phys. D. Appl. Phys.*, vol. 43, no. 1, p. 015502, Jan. 2010.

[31] A. Manthiram, D. L. Bourell, and H. L. Marcus, “Nanophase materials in solid freeform fabrication,” *JOM*, vol. 45, no. 11, pp. 66–70, Nov. 1993.

[32] H. Asgharzadeh and A. Simchi, “Effect of sintering atmosphere and carbon content on the densification and microstructure of laser-sintered M2 high-speed steel powder,” *Mater. Sci. Eng. A*, vol. 403, no. 1–2, pp. 290–298, Aug. 2005.

[33] R. Honeycombe and H. Bhadeshia, *Steels: Microstructure and Properties, Second Edition*, 2nd ed. London: Edward Arnold, 1995, p. 336.

[34] A. J. Sedriks, “Corrosion resistance of austenitic Fe-Cr-Ni-Mo alloys in marine environments,” Jul. 2013.

[35] T. M. Devine, C. L. Briant, and B. J. Drummond, “Mechanism of intergranular corrosion of 316L stainless steel in oxidizing acids,” *Scr. Metall.*, vol. 14, no. 11, pp. 1175–1179, Nov. 1980.

[36] M. S. F. de Lima and S. Sankaré, “Microstructure and mechanical behavior of laser additive manufactured AISI 316 stainless steel stringers,” *Mater. Des.*, vol. 55, pp. 526–532, Mar. 2014.

[37] J. F. Ready, *LIA handbook of laser materials processing*, 2nd ed. Florida: Laser Institute of America, 2001, pp. 561–563.

[38] A. J. Pinkerton, “Multiple-layer cladding of stainless steel using a high-powered diode laser: an experimental investigation of the process characteristics and material properties,” *Thin Solid Films*, vol. 453–454, pp. 471 – 476.

[39] S. A. David, J. M. Vitek, R. W. Reed, and T. L. Hebble, “Effect of rapid solidification on stainless steel weld metal microstructures and its implications on the Schaeffler diagram,” Oak Ridge, TN, Sep. 1987.

[40] Y. Zhang, M. Xi, S. Gao, and L. Shi, “Characterization of laser direct deposited metallic parts,” *J. Mater. Process. Technol.*, vol. 142, no. 2, pp. 582–585, Nov. 2003.

[41] J. Mazumder, “The direct metal deposition of H13 tool steel for 3-D components,” *JOM*, vol. 49, no. 5, pp. 55 – 60, 1997.

[42] M. Alimardani, V. Fallah, M. Iravani-Tabrizipour, and A. Khajepour, “Surface finish in laser solid freeform fabrication of an AISI 303L stainless steel thin wall,” *J. Mater. Process. Technol.*, vol. 212, no. 1, pp. 113–119, Jan. 2012.

[43] K. Abd-Elghany and D. L. Bourell, “Property evaluation of 304L stainless steel fabricated by selective laser melting,” *Rapid Prototyp. J.*, vol. 18, no. 5, pp. 420–428, 2012.

[44] J. Delgado, J. Ciurana, and C. a. Rodríguez, “Influence of process parameters on part quality and mechanical properties for DMLS and SLM with iron-based materials,” *Int. J. Adv. Manuf. Technol.*, vol. 60, no. 5–8, pp. 601–610, Sep. 2011.

[45] J. P. Kruth, L. Froyen, J. Van Vaerenbergh, P. Mercelis, M. Rombouts, and B. Lauwers, “Selective laser melting of iron-based powder,” *J. Mater. Process. Technol.*, vol. 149, no. 1–3, pp. 616–622, Jun. 2004.

[46] Y. F. Shen, D. D. Gu, and P. Wu, “Development of porous 316L stainless steel with controllable microcellular features using selective laser melting,” *Mater. Sci. Technol.*, vol. 24, no. 12, pp. 1501–1505, Dec. 2008.

[47] D. Gu and Y. Shen, “Processing conditions and microstructural features of porous 316L stainless steel components by DMLS,” *Appl. Surf. Sci.*, vol. 255, no. 5, pp. 1880–1887, Dec. 2008.

[48] R. Li, J. Liu, Y. Shi, M. Du, and Z. Xie, “316L Stainless Steel with Gradient Porosity Fabricated by Selective Laser Melting,” *J. Mater. Eng. Perform.*, vol. 19, no. 5, pp. 666–671, Sep. 2009.

[49] E. Yasa and J.-P. Kruth, “Microstructural investigation of Selective Laser Melting 316L stainless steel parts exposed to laser re-melting,” *Procedia Eng.*, vol. 19, pp. 389–395, Jan. 2011.

[50] P. . Kobryn and S. . Semiatin, “Microstructure and texture evolution during solidification processing of Ti–6Al–4V,” *J. Mater. Process. Technol.*, vol. 135, no. 2–3, pp. 330–339, Apr. 2003.

[51] E. Brandl, A. Schoberth, and C. Leyens, “Morphology, microstructure, and hardness of titanium (Ti-6Al-4V) blocks deposited by wire-feed additive layer manufacturing (ALM),” *Mater. Sci. Eng. A*, vol. 532, pp. 295–307, Jan. 2012.

[52] A. Emamian, S. F. Corbin, and A. Khajepour, “The influence of combined laser parameters on in-situ formed TiC morphology during laser cladding,” *Surf. Coatings Technol.*, vol. 206, no. 1, pp. 124–131, Oct. 2011.

[53] A. Emamian, S. F. Corbin, and A. Khajepour, “Tribology characteristics of in-situ laser deposition of Fe-TiC,” *Surf. Coatings Technol.*, vol. 206, no. 22, pp. 4495–4501, Jun. 2012.

[54] A. Emamian, S. F. Corbin, and A. Khajepour, “The effect of powder composition on the morphology of in situ TiC composite coating deposited by Laser-Assisted Powder Deposition (LAPD),” *Appl. Surf. Sci.*, vol. 261, pp. 201–208, Nov. 2012.

[55] A. Emamian, S. F. Corbin, and A. Khajepour, “Effect of laser cladding process parameters on clad quality and in-situ formed microstructure of Fe–TiC composite coatings,” *Surf. Coatings Technol.*, vol. 205, no. 7, pp. 2007–2015, Dec. 2010.

[56] N. W. ; Klingbeil, S. . Bontha, C. J. . Brown, D. R. . Gaddam, P. A. . Kobryn, H. L. . Fraser, and J. L. . Sears, "Effects of Process Variables and Size Scale on Solidification Microstructure in Laser-Based Solid Freeform Fabrication of Ti-6Al-4V," in *2004 Solid Freeform Fabrication Symposium*, 2004, pp. 92–103.

[57] J. E. Davis, N. W. Klingbeil, and S. Bontha, "Effect of Free-edges on Melt Pool Geometry and Solididfication Microstructure in Beam-based Fabrication of Bulkky 3-D Structures," in *Proceedings 2009 Solid Freeform Fabrication Symposium*, 2009, pp. 230–241.

[58] N. W. Klingbeil, J. L. Beuth, R. K. Chin, and C. H. Amon, "Measurement and Modeling of Residual Stress-Induced Warping in Direct Metal Deposition Processes," in *Proceedings 1998 Solid Freeform Fabrication Symposium*, 1998, pp. 367–374.

[59] N. W. Klingbeil, J. W. Zinn, and J. L. Beuth, "Measurement of Residual Stresses in Parts Created by Shape Deposition Manufacturing," in *Proceedings 1997 Solid Freeform Fabrication Symposium*, 1997, pp. 125–132.

[60] N. . Klingbeil, J. . Beuth, R. . Chin, and C. . Amon, "Residual stress-induced warping in direct metal solid freeform fabrication," *Int. J. Mech. Sci.*, vol. 44, no. 1, pp. 57–77, Jan. 2002.

[61] R. Ong, J. Beuth, and L. Weiss, "Residual Stress Control Issues for Thermal Deposition of Polymers in SFF Processes," in *Proceedings 2000 Solid Freeform Fabrication Symposium*, pp. 209–218.

[62] S. Bontha and N. W. Klingbeil, "Thermal Process Maps for Controlling Microstructure in Laser-Based Solid Freeform Fabrication," in *Proceedings 2003 Solid Freeform Fabrication Symposium*, 2003, pp. 219–226.

[63] A. Vasinonta, J. L. Beuth, and R. Ong, "Melt Pool Size Control in Thin-Walled and Bulky Parts via Process Maps," in *Proceedings 20031Solid Freeform Fabrication Symposium*, 2001, pp. 432–440.

[64] A. Vasinonta, J. L. Beuth, and M. L. Griffith, "A Process Map for Consistent Build Conditions in the Solid Freeform Fabrication of Thin-Walled Structures," *J. Manuf. Sci. Eng.*, vol. 123, no. 4, p. 615, Nov. 2001.

[65] A. Vasinonta and J. Beuth, "Process Maps for Controlling Residual Stress and Melt Pool Size in Laser-Based SFF Processes," in *Proceedings 2000 Solid Freeform Fabrication Symposium Solid Freeform Fabrication Symposium*, 2000, pp. 200–208.

[66] A. Vasinonta and J. Beuth, "Process Maps for Laser Deposition of Thin-Walled Structures," in *Proceedings 1999 Solid Freeform Fabrication Symposium*, 1999, pp. 383–392.

[67] D. Rosenthal, "The Theory of Moving Sources of Heat and its Application to Metal Treatments," *Trans. ASME*, vol. 68, pp. 849–866, 1946.

[68] Y. Cao and J. Choi, “Multiscale modeling of solidification during laser cladding process,” *J. Laser Appl.*, vol. 18, no. 3, p. 245, 2006.

[69] P. Saunders, *Radiation Thermometry: Fundamentals and Applications in the Petrochemical Industry*. SPIE PRESS BOOK, 2007, p. 26.

[70] “Jenoptik.” [Online]. Available: http://www.jenoptik.com/en_home.

[71] R. D. Hudson, *Infrared System Engineering*. Wiley-Interscience; 1 edition, 2006, p. 642.

[72] L. Li and W. M. Steen, “<title>In-process clad quality monitoring using optical method</title>,” in *Laser-Assisted Processing II*, 1990, pp. 89–100.

[73] F. Meriaudeau and F. Truchetet, “Control and optimization of the laser cladding process using matrix cameras and image processing,” *J. Laser Appl.*, vol. 8, no. 6, p. 317, Aug. 1996.

[74] D. Salehi and M. Brandt, “Melt pool temperature control using LabVIEW in Nd:YAG laser blown powder cladding process,” *Int. J. Adv. Manuf. Technol.*, vol. 29, no. 3–4, pp. 273–278, Dec. 2005.

[75] D. G. McCartney and J. D. Hunt, “Measurements of cell and primary dendrite arm spacings in directionally solidified aluminium alloys,” *Acta Metall.*, vol. 29, no. 11, pp. 1851–1863, Nov. 1981.

[76] K. Somboonsuk, J. T. Mason, and R. Trivedi, “Interdendritic Spacing: Part I. Experimental Studies,” *Metall. Trans. A*, vol. 15, no. 6, pp. 967–975, Jun. 1984.

[77] D. Bouchard and J. S. Kirkaldy, “Prediction of dendrite arm spacings in unsteady-and steady-state heat flow of unidirectionally solidified binary alloys,” *Metall. Mater. Trans. B*, vol. 28, no. 4, pp. 651–663, Aug. 1997.

[78] R. W. Cahn and P. Haasen, *Physical Metallurgy*, Fourth (4t. Elsevier, 1996.

[79] M. Doubenskaia, P. Bertrand, and I. Smurov, “Pyrometry in laser surface treatment,” *Surf. Coatings Technol.*, vol. 201, no. 5, pp. 1955–1961, Oct. 2006.

[80] C. Doumanidis and Y.-M. Kwak, “Geometry Modeling and Control by Infrared and Laser Sensing in Thermal Manufacturing with Material Deposition,” *J. Manuf. Sci. Eng.*, vol. 123, no. 1, p. 45, 2001.

[81] Y. P. Kathuria and A. Tsuboi, “The effect of beam interaction time on laser cladding process,” pp. 351–352.

[82] I. Smurov, “Pyrometry applications in laser machining,” vol. 4157, pp. 55–66, 2001.

[83] I. Smurov and M. Ignatiev, “Real Time Pyrometry in Laser Surface Treatment,” *Laser Process. Surf. Treat. Film Depos.*, vol. 307, pp. 529–564, 1996.

[84] W. M. Steen and J. Mazumder, *Laser Material Processing*, 4th ed. London: Springer-Verlag, 2010, p. 558.

[85] M. . Griffith, M. . Schlienger, L. . Harwell, M. . Oliver, M. . Baldwin, M. . Ensz, M. Essien, J. Brooks, C. . Robino, J. . Smugeresky, W. . Hofmeister, M. . Wert, and D. . Nelson, “Understanding thermal behavior in the LENS process,” *Mater. Des.*, vol. 20, no. 2–3, pp. 107–113, Jun. 1999.

[86] G. Bi, A. Gasser, K. Wissenbach, A. Drenker, and R. Poprawe, “Investigation on the direct laser metallic powder deposition process via temperature measurement,” *Appl. Surf. Sci.*, vol. 253, no. 3, pp. 1411–1416, Nov. 2006.

[87] M. Doubenskaia, P. Bertrand, and I. Y. Smurov, “Temperature Monitoring of Nd:YAG Laser Cladding (CW and PP) by Advanced Pyrometry and CCD-Camera based Diagnostic Tool,” *Laser-Assisted Micro- and Nanotechnologies*, vol. 5399, pp. 212–219, Apr. 2004.

[88] M. Pavlov, D. Novichenko, and M. Doubenskaia, “Optical Diagnostics of Deposition of Metal Matrix Composites by Laser Cladding,” *Phys. Procedia*, vol. 12, pp. 674–682, Jan. 2011.

[89] Y. P. Hu, C. W. Chen, and K. Mukherjee, “Measurement of temperature distributions during laser cladding process,” *J. Laser Appl.*, vol. 12, no. 3, p. 126, 2000.

[90] T. Hua, C. Jing, L. Xin, Z. Fengying, and H. Weidong, “Research on molten pool temperature in the process of laser rapid forming,” *J. Mater. Process. Technol.*, vol. 198, no. 1–3, pp. 454–462, Mar. 2008.

[91] S. Lhospitalier, P. Bourges, A. Bert, J. Quesada, and M. Lambertin, “Temperature measurement inside and near the weld pool during laser welding,” *J. Laser Appl.*, vol. 11, no. 1, p. 32, 1999.

[92] P. Peyre, P. Aubry, R. Fabbro, R. Neveu, and A. Longuet, “Analytical and numerical modelling of the direct metal deposition laser process,” *J. Phys. D. Appl. Phys.*, vol. 41, no. 2, p. 025403, Jan. 2008.

[93] L. Wang and S. Felicelli, “Analysis of thermal phenomena in LENS™ deposition,” *Mater. Sci. Eng. A*, vol. 435–436, pp. 625–631, Nov. 2006.

[94] Y. Zhang, G. Yu, X. He, W. Ning, and C. Zheng, “Numerical and experimental investigation of multilayer SS410 thin wall built by laser direct metal deposition,” *J. Mater. Process. Technol.*, vol. 212, no. 1, pp. 106–112, Jan. 2012.

[95] M. Vasudevan, N. Chandrasekhar, V. Maduraimuthu, a. K. Bhaduri, and B. Raj, "Real-Time Monitoring of Weld Pool during GTAW using Infra-Red Thermography and analysis of Infra-Red thermal images," *Weld. World*, vol. 55, no. 7–8, pp. 83–89, Mar. 2013.

[96] L. Song and J. Mazumder, "Feedback Control of Melt Pool Temperature During Laser Cladding Process," *IEEE Trans. Control Syst. Technol.*, vol. 19, no. 6, pp. 1349–1356, Nov. 2011.

[97] W. Hofmeister and M. Griffith, "Solidification in direct metal deposition by LENS processing," *JOM*, vol. 53, no. 9, pp. 30–34, Sep. 2001.

[98] L. Wang, S. D. Felicelli, and J. E. Craig, "Thermal Modeling and Experimental Validation in the LENS TM Process," in *Proceedings 2007 Solid Freeform Fabrication Symposium*, 2007, pp. 100–111.

[99] S. Yamashita, A. Fujinaga, M. Yamamoto, K. Shinozaki, and K. Kadoi, "In-situ Temperature Measurement using Monochrome High-speed Sensors during Laser Welding," pp. 0–3, 2012.

[100] J. Yu, X. Lin, J. Wang, J. Chen, and W. Huang, "Mechanics and energy analysis on molten pool spreading during laser solid forming," *Appl. Surf. Sci.*, vol. 256, no. 14, pp. 4612–4620, May 2010.

[101] *ASM Metals Handbook*, 8th ed. p. 424.

[102] J. C. Lippold and K. Damian J., *Welding Metallurgy and Weldability of Stainless Steels*. Wiley-Interscience, 2005, p. 357.

[103] K.-P. M. Michael Vollmer, *Infrared Thermal Imaging: Fundamentals, Research and Applications*. Wiley-VCH, 2010.

[104] H. Sadiq, M. B. Wong, X.-L. Zhao, and R. Al-Mahaidi, "Effect of high temperature oxidation on the emissivity of steel," 2011.

[105] R. Felice, "Pyrometry for Liquid Metals," *Adv. Mater. Process.*, vol. July, pp. 31–33, 2008.

[106] "NI Labview PID." [Online]. Available: http://www.ni.com/white-paper/3782/en/.

[107] G. J. Davies, *Solidification And Casting*. Essex: Applied Science Publishers LTD., 1973, p. 206.

[108] M. C. Flemings, *Solidification processing*, vol. 8. McGraw-Hill, 1974, p. 364.

[109] B. Chalmers, "The structure of ingots," *J. Aust. Inst. Met.*, 1963.

[110] E. Heyn, "Short Reports from the Metallurgical Laboratory of the Royal Mechanical and Testing Institute of Charlottenburg," *Metallographist*, vol. 5, pp. 37–64, 1903.